KU LEUVEN

ULB

ARENBERG DOCTORAL SCHOOL
Faculty of Science

Gravitational wave signatures of dark matter environments

Ludovico Machet

Dissertation presented in partial fulfillment
of the requirements for the degree of
Doctor of Science (PhD): Physics

Supervisors:
Prof. dr. Thomas Hertog
Prof. dr. Geoffrey Compère

October 2025

GRAVITATIONAL WAVE SIGNATURES OF DARK MATTER ENVIRONMENTS

Ludovico MACHET

Supervisors:
Prof. dr. Thomas Hertog
Prof. dr. Geoffrey Compère

Members of the
Examination Committee:
Prof. dr. Laura Lopez Honorez, chair
Prof. dr. Tjonnie Li
Dr. Henri Inchauspé
Prof. dr. Tanja Hinderer
(Utrecht University)
Prof. dr. Sumanta Chakraborty
(School of Physical Sciences, IACS)

Dissertation presented in partial fulfillment of the requirements for the degree of Doctor of Science (PhD): Physics

October 2025

Uitgegeven in eigen beheer, Ludovico Machet, Brussels (Belgium)

Acknowledgments

The doctoral journey that resulted in this manuscript has been a long and challenging path, one that would not have been successful without the support, mentorship, and encouragement of many individuals and institutions. With these words, I wish to express my deepest gratitude to each of them. Their constant presence has been fundamental to this work and to my contribution to the scientific endeavour.

First and foremost, I would like to express my heartfelt gratitude to my advisors, Geoffrey and Thomas. Your support, patience, and dedication have been crucial to my academic growth and to the pursuit of the ideas discussed in this thesis. Your vision to strengthen the gravitational wave community in Belgium is already bearing fruit and has been incredibly helpful for my research.

I am also thankful to the Research Foundation - Flanders (FWO) for entrusting me with a PhD fellowship in fundamental research and for providing the financial support that made this work possible. At the same time, I am grateful to the European Space Agency (ESA) for funding the initial part of my stay at KU Leuven.

Next, I would like to acknowledge my collaborators, who generously shared their ideas, insights, and knowledge with me. A special thanks goes to you, Sumanta, for breathing new life into our main project. I am also deeply grateful to Pablo Cano for introducing me to the problem of compact objects from new fundamental fields, which added an important connection to high-energy physics in my work. More generally, thank you for being an inexhaustible source of expertise and insight. A heartfelt thanks also goes to Llibert Aresté Saló, who shared his deep experience in numerical relativity with me and made the final chapter of this work possible.

To my colleagues - students and seniors alike - at KU Leuven, ULB, and beyond, including Simon, Marina, Daniel, Bogdan, Caroline, Annelien, Milan, Arthur, Francesco, Tom, Joel, Gaston, Lorenzo, and Guillaume: I extend my deepest

appreciation. Your professional collaboration and friendship made these years all the more enjoyable.

Equally important, I want to thank the incredible people I encountered outside of my academic life during these years. Dennis, Feng, Ellen, Markus, Leila, Lucrezia, Iro, I am so happy to call you my friends. You have been my keys to Brussels. Rossana, the best housemate I could have asked for. Going through our PhD struggles together and always supporting each other made life lighter.

And I cannot forget to thank you, François. Your love, presence, and belief in me were absolutely fundamental to completing this journey. Thank you for seeing value in my work, for your curiosity, and for asking precise questions from the very first moment our lives intersected. Thank you for the light your eyes give back when I tell you about my "silly" science.

Finally, a last but crucial word for my family. To my sister, Martina, your brilliant journey in and outside of physics inspires me every day. And to my parents, Piera and Riccardo, you are the source of these pages as much as I am. Thank you for supporting me every step of the way.

Popularized Abstract

Gravitational wave observations opened an exciting new window to study the gravitational Universe. Direct detections of black holes and neutron stars are revealing the dynamics of compact objects and are likely to improve our understanding of gravity in the strong-field regime. To properly interpret these signals, the potential influence of matter surrounding their source has to be evaluated. This work explores how matter effects modify the properties of gravitational wave sources, focusing on an environment composed by dark matter.

First, we model a Schwarzschild black hole immersed in a dark matter spike, deriving a fully relativistic matter density profile. We compute the system's quasi-normal oscillation frequencies, and its response to a tidal perturbation. The relativistic dark matter profile leads to distinct scaling laws for the quasi-normal modes frequency shifts compared to non-relativistic models, while the Love numbers provide a potential signature of the dark matter presence. We then introduce a different model for the dark matter component, a scalar field resulting from nonlinear sigma models, motivated by string theory compactification. We first study boson stars solutions to these models, self-gravitating condensates of massive bosonic fields. We show that these theories allow for spherically symmetric solutions, that have properties dependent on the sigma mode curvature. Next, we study the dynamics of such scalar fields on black hole spacetimes, simulating their accretion onto isolated black holes and their impact on binary black hole mergers. Using numerical relativity, we show that the curvature of the sigma model dictates whether the scalar field behaves as an attractive or repulsive self-interaction, altering the accretion physics and the gravitational wave emission.

By incorporating nonlinear field theories, relativistic dark matter profiles, and advanced numerical techniques, we contribute to the effort of detecting subtle imprints of exotic physics in gravitational wave signals, as well as improving high-precision tests of general relativity with future gravitational waves detectors.

Gepopulariseerde Samenvatting

Zwaartekrachtgolven waarnemingen hebben een opwindend nieuw venster geopend voor het bestuderen van het gravitationele heelal. Directe detecties van zwarte gaten en neutronensterren onthullen de dynamica van compacte objecten en zullen waarschijnlijk ons begrip van zwaartekracht in het sterke-veldregime verbeteren. Om deze signalen correct te interpreteren, moet de potentiële invloed van materie rondom hun bron worden geëvalueerd. Dit werk onderzoekt hoe materie-effecten de eigenschappen van zwaartekrachtgolfbronnen wijzigen, met een focus op een omgeving samengesteld uit donkere materie.

Eerst modelleren we een Schwarzschild-zwart gat dat is omgeven door een donkere-materie-"spike"(piek), waarbij we een volledig relativistisch materiedichtheidsprofiel afleiden. We berekenen de quasi-normale oscillatiefrequenties van het systeem en de respons op een getijverstoring. Het relativistische donkere-materieprofiel leidt tot verschillende schalingswetten voor de frequentieverschoven quasi-normale modi in vergelijking met niet-relativistische modellen, terwijl de Love-getallen een potentieel signatuur van de aanwezigheid van donkere materie bieden. Vervolgens introduceren we een ander model voor de donkere-materiecomponent, een scalair veld afkomstig van niet-lineaire sigma-modellen, geïnspireerd door stringtheorie-compactificatie. Eerst bestuderen we bosonster-oplossingen voor deze modellen, zelf-graviterende condensaten van massieve bosonische velden. We tonen aan dat deze theorieën toestaan dat bolsymmetrische oplossingen bestaan, waarvan de eigenschappen afhangen van de kromming van de sigma-modus. Daarna bestuderen we de dynamica van dergelijke scalaire velden in zwarte-gat-ruimtetijden, waarbij we hun accretie op geïsoleerde zwarte gaten en hun impact op samensmeltende dubbel-zwart-gat-systemen simuleren. Met behulp van numerieke relativiteit tonen we aan dat de kromming van het sigma-model bepaalt of het scalair veld zich gedraagt als een aantrekkelijke of afstotende zelf-interactie, waardoor de

accretiefysica en de emissie van zwaartekrachtgolven worden gewijzigd.

Door niet-lineaire veldtheorieën, relativistische donkere-materieprofielen en geavanceerde numerieke technieken te integreren, dragen we bij aan de inspanningen om subtiele afdrukken van exotische fysica in zwaartekrachtgolfsignalen te detecteren, evenals het verbeteren van hoog-precisiemetingen van algemene relativiteitstheorie met zwaartekrachtgolven-detectoren van de volgende generatie.

Abstract

Next-generation gravitational wave detectors will require higher accuracy waveform models to faithfully recover the parameters of the detected signals' sources. In this thesis, motivated by this consideration and by the opportunities to uncover new physics in these high-precision measurements, we investigate the impacts of a dark matter distribution on potential gravitational waves sources for this class of detectors. We focus on two kinds of candidates: a fluid-like cold dark matter and a minimally coupled scalar field sector derived from a nonlinear sigma model. This work discussed how these matter distributions could imprint signatures on a gravitational wave source.

First, we model a Schwarzschild black hole immersed in a dark matter spike, deriving a fully relativistic density profile for the fluid-like dark matter through adiabatic contraction of an initial Hernquist profile. Via black hole perturbation theory on this spacetime, we compute the system's quasi-normal modes (QNMs), and its response to a tidal perturbation via the tidal Love numbers (TLNs). We observe that the QNMs receive corrections with respect to their values in a vacuum Schwarzschild spacetime, and that the TLNs are non-vanishing. We find that the relativistic dark matter profile leads to distinct scaling laws for the quasi-normal modes frequency shifts compared to non-relativistic models, and that the shifts are suppressed for massive and diluted halos. The Love numbers, while small, provide a new channel for energy loss during the inspiral phase, which could alter a binary black hole dynamics over several orbits.

In the second part of the thesis, we introduce a scalar field resulting from nonlinear sigma models, motivated by string theory compactification arguments. We introduce the maximally symmetric $\mathrm{SL}(2,\mathbb{R})$ and $\mathrm{O}(3)$ sigma models. We identify spherically symmetric boson stars solutions to these models, self-gravitating condensates of massive bosonic fields. The curvature of the sigma models is shown to affect significantly the properties of such solutions. The $\mathrm{SL}(2,\mathbb{R})$ model yields light and diluted boson stars, while the $\mathrm{O}(3)$ theory allows for solutions with mass and compactness of the order of those of neutron stars.

Finally, we study the dynamics of such scalar fields on black hole spacetimes, simulating their accretion onto isolated black holes and their impact on binary black hole mergers. Using numerical relativity simulations with the `GRChombo` code, we show that the curvature of the sigma model dictates whether the scalar field behaves as an attractive or repulsive self-interaction, altering the accretion physics and the gravitational wave emission. The $\mathrm{SL}(2,\mathbb{R})$ field behaves with an attractive self-interaction, while the $\mathrm{O}(3)$ one shows a repulsive dynamics. This emerges clearly in the accretion process when the scalar field mass is low with respect to the black hole scale. In the binary black hole case, the scalar field forms a circumbinary cloud that induces a dephasing in the GW waveform, with the direction and magnitude of the dephasing depending on the model's curvature. We observe indications that these models suppress *bosenova* phenomena, i.e. a rapid instability which results in the ejection of the boson cloud from the binary system.

The results of this work contribute to ongoing efforts to characterise the main contributions from an environment that will have to be included in the waveform generation pipelines for future gravitational waves observatories. We argue that this line of research will be key to unlock the maximal amount of information from future observations, allowing for precise tests of general relativity and for the detection of new fundamental physics in the gravity sector.

Beknopte samenvatting

Zwaartekrachtgolven-detectoren van de volgende generatie zullen nauwkeurigere golfvormmodellen vereisen om de parameters van de bronnen van gedetecteerde signalen betrouwbaar te kunnen reconstrueren. In dit proefschrift, gemotiveerd door deze overweging en door de mogelijkheden om nieuwe fysica te ontdekken in deze hoog-precisiemetingen, onderzoeken we de impact van een donkere-materieverdeling op potentiële zwaartekrachtgolfbronnen voor deze klasse van detectoren. We richten ons op twee soorten kandidaten: een vloeistofachtige koude donkere materie en een minimaal gekoppelde scalair-veldsector afgeleid van een niet-lineair sigma-model. Dit werk bespreekt hoe deze materieverdelingen kenmerken kunnen achterlaten op een zwaartekrachtgolfbron.

Eerst modelleren we een Schwarzschild-zwart gat dat is omgeven door een donkere-materie-"spike"(piek), waarbij we een volledig relativistisch dichtheidsprofiel afleiden voor de vloeistofachtige donkere materie door adiabatische contractie van een initieel Hernquist-profiel. Via de zwarte-gat-verstoringstheorie op deze ruimtetijd berekenen we de quasi-normale modi (QNM's) van het systeem en de respons op een getijverstoring via de getij-Love-getallen (TLN's). We observeren dat de QNM's correcties ondergaan ten opzichte van hun waarden in een vacuüm Schwarzschild-ruimtetijd, en dat de TLN's niet verdwijnen. We vinden dat het relativistische donkere-materieprofiel leidt tot verschillende schalingswetten voor de frequentieverschoven quasi-normale modi in vergelijking met niet-relativistische modellen, en dat de verschuivingen worden onderdrukt voor massieve en verdunde halo's. De Love-getallen, hoewel klein, bieden een nieuw kanaal voor energieverlies tijdens de inspiraalfase, wat de dynamica van een dubbel-zwart-gatsysteem over meerdere banen kan veranderen.

In het tweede deel van het proefschrift introduceren we een scalair veld afkomstig van niet-lineaire sigma-modellen, gemotiveerd door argumenten uit de stringtheorie-compactificatie. We introduceren de maximaal symmetrische $\mathrm{SL}(2,\mathbb{R})$ en $\mathrm{O}(3)$ sigma-modellen. We identificeren bolsymmetrische bosonster-

oplossingen voor deze modellen, zelf-graviterende condensaten van massieve bosonische velden. De kromming van de sigma-modellen blijkt de eigenschappen van dergelijke oplossingen aanzienlijk te beïnvloeden. Het $\mathrm{SL}(2,\mathbb{R})$ model levert lichte en verdunde bosonsterren op, terwijl de $\mathrm{O}(3)$ theorie oplossingen toestaat met massa en compactheid van de orde van die van neutronensterren.

Ten slotte bestuderen we de dynamica van dergelijke scalaire velden in zwarte-gat-ruimtetijden, waarbij we hun accretie op geïsoleerde zwarte gaten en hun impact op samensmeltende dubbel-zwart-gat-systemen simuleren. Met behulp van numerieke relativiteitssimulaties met de `GRChombo`-code tonen we aan dat de kromming van het sigma-model bepaalt of het scalair veld zich gedraagt als een aantrekkelijke of afstotende zelf-interactie, waardoor de accretiefysica en de emissie van zwaartekrachtgolven worden gewijzigd. Het $\mathrm{SL}(2,\mathbb{R})$ veld vertoont een aantrekkelijke zelf-interactie, terwijl het $\mathrm{O}(3)$ veld een afstotende dynamica laat zien. Dit komt duidelijk naar voren in het accretieproces wanneer de massa van het scalair veld laag is ten opzichte van de schaal van het zwarte gat. In het geval van dubbel-zwart-gat-systemen vormt het scalair veld een circumbinaire wolk die een faseverschil in de zwaartekrachtgolfvorm induceert, waarbij de richting en grootte van het faseverschil afhangen van de kromming van het model. We observeren aanwijzingen dat deze modellen *bosenova*-fenomenen onderdrukken, dat wil zeggen een snelle instabiliteit die resulteert in de uitstoting van de bosonwolk uit het binaire systeem.

De resultaten van dit werk dragen bij aan de lopende inspanningen om de belangrijkste bijdragen van een omgeving te karakteriseren die moeten worden opgenomen in de golfvormgeneratiepijplijnen voor toekomstige zwaartekrachtgolven-observatoria. We betogen dat deze onderzoeklijn essentieel zal zijn om de maximale hoeveelheid informatie uit toekomstige waarnemingen te halen, waardoor precieze tests van de algemene relativiteitstheorie en de detectie van nieuwe fundamentele fysica in de zwaartekrachtsector mogelijk worden.

List of Abbreviations

ADM Arnowitt, Deser and Misner. 77

BBH binary black hole. 85

BSSN Baumgarte, Shapiro, Shibata, Nakamura form of the ADM equations. 78

CCT Conformal Transverse-Traceless formulation of the constraint equations. 80

CCZ4 Conformal-covariant Z4 formulation of the ADM equations. 78

DF dynamical friction. 9

DM dark matter. 7

EMRI extreme mass-ratio inspiral. 6

EOB effective one-body. 4

ET Einstein Telescope. 4

GR General Relativity. 1

GSF gravitational self-force. 4, 5

GW gravitational waves. 2

IMRI intermediate mass-ratio inspiral. 6

LISA Laser Interferometer Space Antenna. 4

LVK LIGO-Virgo-KAGRA. 2, 4

NR numerical relativity. 4

PM post-Minkowskian. 4

PN post-Newtonian. 4

SNR signal-to-noise ratio. 3

Contents

List of Figures

List of Tables

Chapter 1

General introduction

In the context of Einstein's General Relativity (GR), the spacetime geometry is dynamical and it is related to the matter and energy content of the Universe via the well-known Einstein field equations

$$R_{\mu\nu} - \frac{1}{2}\, g_{\mu\nu} R = 8\pi\, T_{\mu\nu}, \tag{1.1}$$

with $R_{\mu\nu}$, R the Ricci tensor and scalar, $g_{\mu\nu}$ the metric tensor, $T_{\mu\nu}$ the stress-energy tensor [1] and we are setting the constants $G = c = 1$. In the weak-field regime, one can linearize equation (1.1) for perturbations of the metric tensor around a flat Minkowski background $g_{\mu\nu} = \eta_{\mu\nu} + h_{\mu\nu}$, with $|h_{\mu\nu}| \ll 1$. The trace-reversed perturbation

$$\bar{h}_{\mu\nu} := h_{\mu\nu} - \frac{1}{2}\eta_{\mu\nu} h^{\alpha}_{\alpha}, \tag{1.2}$$

satisfies a wave equation sourced by the stress-energy tensor

$$\Box \bar{h}_{\mu\nu} = -16\pi T_{\mu\nu}. \tag{1.3}$$

The operator $\Box = -\partial_t^2 + \nabla^2$ is the flat space d'Alembertian and equation (1.3) follows from the field equations after imposing the *Lorentz* (or *de Donder*) gauge condition $\partial^{\nu} \bar{h}_{\mu\nu} = 0$. These spacetime oscillations, propagating at the speed of

[1] In general, the field equations admit an additional term in the left hand side of the form $\Lambda g_{\mu\nu}$, with Λ the cosmological constant. For the purpose of this thesis, we will globally assume the spacetime to be asymptotically flat, so that equation (1.1) holds.

light according to a wave-light equation of motion, are known as gravitational waves (GW). Outside of the source, i.e. for $T_{\mu\nu} = 0$, gauge transformations can be used to reduce $h_{\mu\nu}$ to a traceless form with two degrees of freedom, which are transverse with respect to the propagation direction. The *transverse-traceless (TT)* gauge is defined by

$$h^{TT}_{\mu 0} = 0, \qquad h^{TT\,\mu}{}_{\mu} = 0 \tag{1.4}$$

In this gauge, a plane wave travelling along the $\hat{z}$ axis can be written as

$$h^{TT}_{\mu\nu} = \begin{pmatrix} 0 & 0 & 0 & 0 \\ 0 & h_+ & h_\times & 0 \\ 0 & h_\times & -h_+ & 0 \\ 0 & 0 & 0 & 0 \end{pmatrix}_{\mu\nu} \cos[\omega(t-z)], \tag{1.5}$$

with $h_+, h_\times$ the amplitudes of two propagating degrees of freedom, also referred to as the plus and cross polarisations, and ω the frequency. In the source region, the solution to equation (1.3) is found integrating the Green's function associated to the d'Alembertian operator over the stress-energy tensor. At lowest order of a multipole expansion, the amplitude is related to the second time derivative of the quadrupolar component of the source's energy density Q_{ij}, i.e.

$$h^{TT}_{ij} \sim \frac{2}{r}\ddot{Q}_{ij}(t-r). \tag{1.6}$$

GWs carry energy and angular momentum, and impact the proper distance in between two free-falling observers. When such observers are mirrors suspended at the extremities of a laser interferometer, the difference in arm-length induced by a passing GW alters the frequency of the laser beams travelling in the system. Once recombined, the dephased laser transmits an optical signal proportional to the amplitude (generally called strain) of the wave, which can be detected. This idea is the key working mechanism of the GW detectors currently operated by the LIGO-Virgo-KAGRA (LVK) Collaboration. Such experiments reported the first direct detection of a GW in 2016 [5], observing the merger of two black holes of order 30 solar masses. To this date, the LVK Collaboration has observed up to 218 events [2], opening a rich new window on the gravitational Universe. These events are summarized in the well-known *stellar graveyard* plot of Figure 1.1.

Each circle on Figure 1.1 represents a compact object detected either via standard electromagnetic signals, red and yellow circles at the bottom, or via GWs, orange and blue ones. The discovery of such a rich population of objects has allowed fundamental progress in the understanding of high-energy

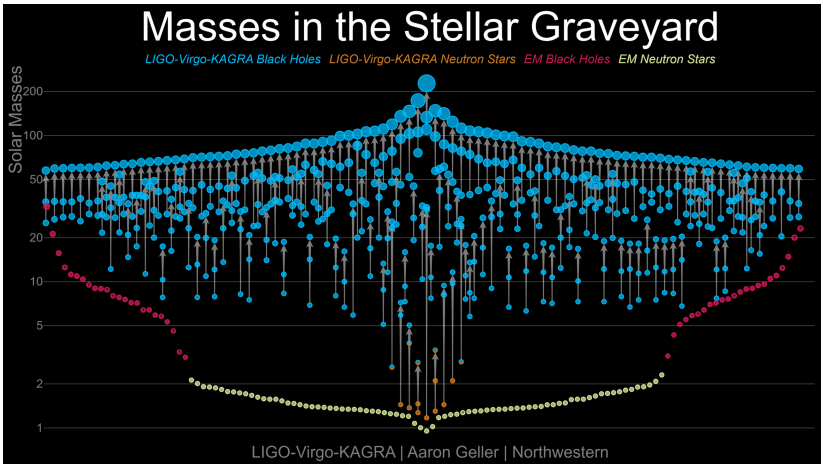

Figure 1.1: Known compact objects likely produced from stellar evolution. The light yellow and red dots at the bottom are neutron stars and black holes, respectively, detected via electromagnetic signals. The orange and light blue circles are neutron stars and black holes detected in GW mergers [LVK/A. Geller/Northwestern].

astrophysical systems. Finding black holes with masses around 3 solar masses and above 60 solar masses is drawing new light to the testing of stellar evolution models, as stellar dynamics should prevent their formation [3, 1]. Moreover, combined with electromagnetic data, GW have made possible the breakthrough multimessenger detection of a binary neutron star merger, of the subsequent kilonova emission and the related heavy elements nucleosynthesis [4, 141].

The typical GW strain detectable by the LVK interferometers is of order $\delta L/L \sim |h_{\mu\nu}| \sim 10^{-21}$. Theoretical models of the expected signals, called *waveforms*, are thus fundamental to extract the signals from the instrumental noise. Matched-filtering techniques compare theoretical waveforms templates to the data output of the detectors, maximizing the signal-to-noise ratio (SNR) over the physical parameters space [11]. This step is crucial to uncover the faint physical signal from the loud instrumental noise.

Obtaining waveform models requires solving the relativistic two-body problem for binaries of compact objects which orbits shrink because of the emission of GWs. This first stage of a binary's evolution is called the *inspiral* and it constitute the longest part of a GW signal. Eventually, the compact objects reach the last stable orbit and plunge into each other in a strongly nonlinear phase referred to as *merger*. Finally, the spacetime's excitations around the

remnant body decay in a quasi-normal oscillatory phase known as *ringdown*. This problem notoriously does not admit a closed form solution and approximate methods are required in different regimes of the evolution. Four main techniques are used: for widely separated binaries, the weak-field approximation holds and the relativistic effects can be obtained via a post-Newtonian (PN) or post-Minkowskian (PM) expansion, if the velocities are taken to be small with respect to the speed of light or not, respectively. When the objects are in the strong-field regime and move at high velocities, or when non-linear effects become relevant, a numerical approach can be taken, with tools from numerical relativity (NR). The equations of motion can also be expanded in the ratio of the two bodies masses when this is small, so that the lighter object effectively traces a forced geodesic motion in an effective background metric. This latest approach is known as gravitational self-force (GSF) theory and it is adapted to asymmetric binaries in the strong-field regime. Finally, the post-merger phase of the dynamics is modelled with isolated black hole perturbation theory. The regions of validity of these different schemes are plotted on Figure 1.2. Phenomenological and effective models, like the effective one-body formalism (EOB) combine inputs from these techniques to produce fast and accurate waveforms over all the phases of a binary coalescence [63, 125].

The state-of-the art waveform models implemented into data-analysis pipelines are accurate enough to faithfully recover the parameters of the sources expected to fall into the LVK band, i.e. binary black holes of stellar mass scale and neutron star - black hole or neutron star - neutron star binaries. The next generation of GW observatories, however, is expected to require more accurate waveforms in order to perform unbiased parameter reconstruction and to fully reach its science goals. Ground-based detectors like the Einstein Telescope (ET) and Cosmic Explorer will observe in a frequency band largely overlapping with the one accessible to LVK, but at higher sensitivity [165, 197]. The increased sensitivity will allow the detection of louder signals, i.e. of signals with an SNR of order $\mathcal{O}(SNR) \sim 10^3$. This will decrease the uncertainties in the posterior space of parameters. When these become comparable to the intrinsic uncertainty of the waveform model, biases can emerge in the parameter inference. Figure 1.3 shows how high-SNR signals will require the development of waveform models one to three order of magnitude more accurate than the ones currently available [195].

High-accuracy waveforms will be also essential for space-based interferometers like the recently adopted Laser Interferometer Space Antenna (LISA) [90]. Spanning an arm length of 2.5 million kilometres, LISA will access GWs in the mHz regime, emitted by a wide variety of sources. Differently than present detectors, for which the physical signals are distributed sparsely in the data stream, LISA will be signal-dominated, with a large number of overlapping

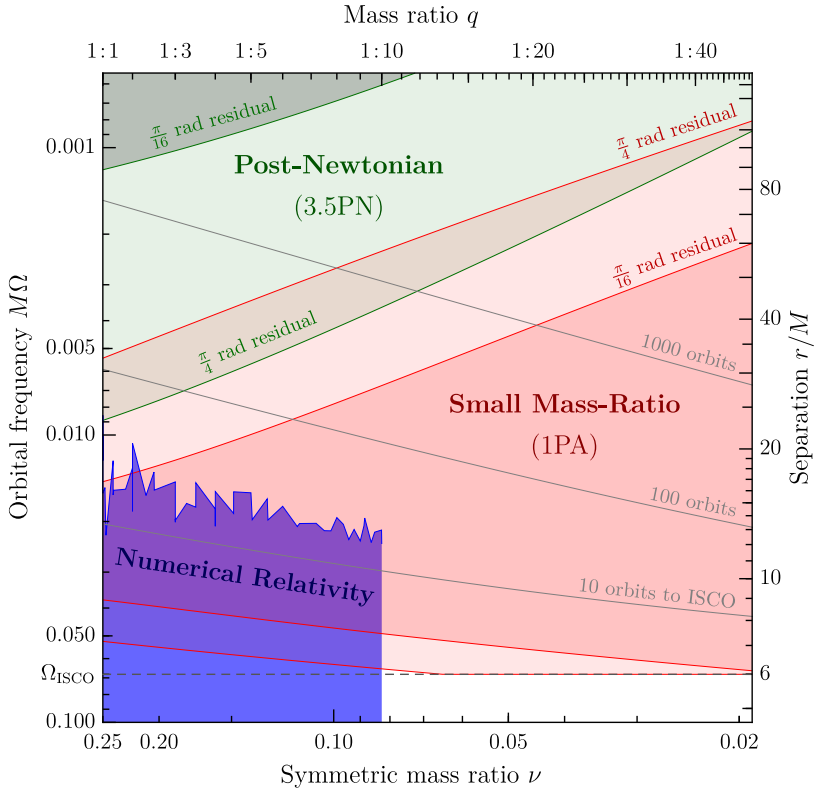

Figure 1.2: Domains of validity of different approximation schemes to the relativistic two-body problem, for a non-spinning quasi-circular binary. The $1PA$ tag refers to the first post-adiabatic order in he GSF expansion. The grey lines indicate the number of orbits away from ISCO for binaries with the given parameters. This plot appears in [172, 6].

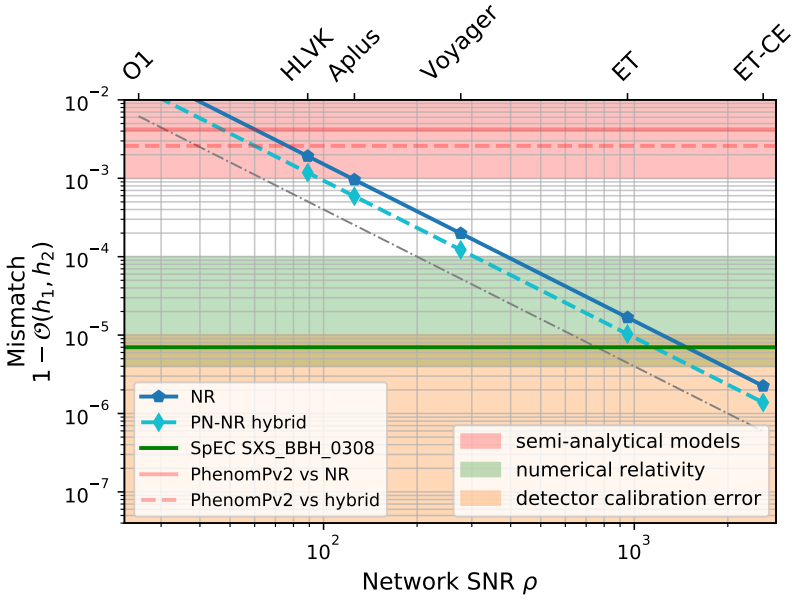

Figure 1.3: Mismatch between a reference non-spinning quasi-circular NR waveform SXS_BBH_0308 and injected signals from Phenom and NR models as a function of the SNR. When the mismatch is below the thick blue line, the waveforms are indistinguishable. Current Phenom models are not sufficient for unbiased parameter estimation with third generation detectors as ET and CE. This plot is taken from [195].

signals in band at all time, together with some long-lived and high-SNR events from massive black holes binaries. Such data structure will require waveform models to be accurate over a large number of orbits [6], in order to correctly detect persistent signals and to minimize residuals in subdominant sources.

Furthermore, accurate templates will be needed to achieve the science goal of performing precision tests of GR and to put stringent constraints on beyond-GR theories. These are key objectives for the next-generation GW observatories. ET aims to improve significantly the bounds on deviations from GR in the inspiral phase of compact object binaries, test for the presence of extra polarizations in the signals [213], and test discrepancies with the black-hole paradigm at percent-level accuracy from the post-merger phase [40, 46]. LISA will be sensitive to stellar-mass black holes inspiraling into quiet massive black holes at the center of galaxies or stellar cluster, giving rise to intermediate or extreme mass-ratio inspirals, known as IMRIs or EMRIs depending on the asymmetry between

the components' masses. Such systems can emit GW in the LISA band over a timescale of years, tracing over 10^5 orbits [114], providing exquisite probes of the spacetime geometry up to some Schwarzschild radii away from the primary black hole.

On top of allowing probes of GR in the strong-field regime at high-precision, the future GW detectors may be sensitive to new fundamental physics, like extensions to GR itself or to the Standard Model of particle physics. New physics impacts a binary coalescence in all its phases: in the inspiral regime, where the GR weak-field expansions can receive corrections or be affected by non-zero tidal effects [41, 71], in the highly-dynamical merger phase, where nonlinear terms can become relevant, and in the ringdown phase, which frequency content would differ from the GR one [65, 191]. Furthermore, GW signals from a binary of compact objects could be affected by the presence of a non-vacuum environment interacting with the source [29]. The environments can be composed by baryonic matter, like gaseous accretion disks [77], or dark matter (DM) haloes [187]. Generically, the exchange of energy and angular momentum between the compact objects and the environment induces a dephasing of the inspiral. It is therefore crucial to carefully characterise the effect that different kinds of environments likely to encompass next-generation GW sources might have onto the expected signals. The goal of such investigation is twofold: on one hand, including environmental effects into data analysis and parameter estimation pipelines will ensure to avoid biases in the reconstruction of the sources' properties [93, 154, 227]. On the other hand, the imprints of a matter environment onto the different stages of a coalescence could help constrain the environment properties and composition, possibly shining some light on long-lasting questions like the nature of DM or the possible existence of beyond-Standard Model fields [84].

In the next sections, we will outline the current results concerning the presence of matter around a GW source, with a particular focus on DM distributions, which will be the subject of the work presented in the rest of this thesis.

1.1 Dark matter environments of GW sources

The presence of dark matter in the energy budget of the universe is strongly supported by a large amount of data and observations on several scales. It is a key component of our current cosmological model [43]. The first hints suggesting the existence of a matter sector not contributing to the total luminosity of galaxies came from pioneering works studying the velocity dispersions of galaxy clusters as well as of stars in a single galaxy [228, 203]. Since then, additional data coming from the large-scale structure of the universe, the

cosmic microwave background anisotropies, light elements abundances from Big Bag Nucleosynthesis, gravitational lensing, baryonic acoustic oscillations, have contributed to the development of the cosmological ΛCDM model. To match such abundance of data on a large scale, DM is described as a massive perfect fluid, composed by collisionless particles moving at non-relativistic speeds, i.e. *cold*, at the structure formation era.

Despite an outstanding agreement with these observations at galactic and cosmological scale, the behaviour of DM at small scales is still object of investigation and questioning, with tensions with the ΛCDM model as the cusp-core and the missing satellite problems [222, 189]. At the same time, the nature of the DM component (or components), remains unknown and largely unconstrained. Figure **??** shows a sketch of various candidates that could make up for the totality or some fraction of the DM observed in the universe and the mass ranges they globally span. The lower bound comes from cosmological observations constraining the coherent wave-light behaviour of DM at very large scales, while macroscopic candidates are allowed to constitute at least part of the DM up to stellar mass objects.

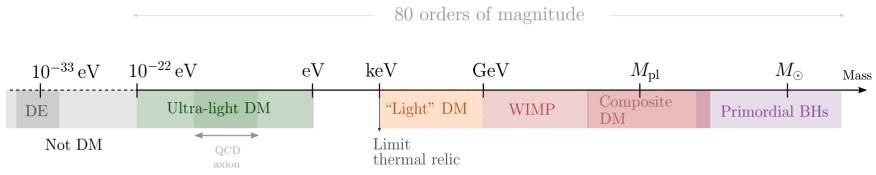

Figure 1.4: Schematic diagram representing the possible mass range spanned by DM candidates. The allowed region covers several orders of magnitude in mass and it is relatively unconstrained. A variety of physical objects, like new fundamental fields or primordial black holes, can be invoked as DM candidates. The sketch is taken from [107].

Despite intense efforts to directly detect the microscopic components of DM, in the case they would arise from an unknown fundamental field [167], the nature of the dark sector remains an open question. DM to Standard Model particles interactions have failed to yield any information about this puzzle, and DM evidence has mainly accumulated from gravitational observations. Thus, it is well-motivated to investigate if GWs can help characterize DM, as they probe gravity in the strong-field regime. If a significant DM density was to be present in the surroundings of a GW source, the emitted signal could bring signatures of such environment, that might lead to the detection of such distribution and the distinction between different DM candidates [42, 84].

Considerable efforts have been made to quantify the impact of DM environmental effects on candidate sources, as well as for baryonic environments like accretion disks. A summary of early results was compiled in the seminal analysis of Barausse, Cardoso and Pani [29]. Several works have used Newtonian and non-relativistic modelling of the sources' environments to obtain order-of-magnitude estimates and first-order corrections to the GW waveforms. More recently, efforts have been focused in developing fully relativistic techniques to precisely account for the environments' impacts and to develop self-consistent waveforms at the level of accuracy required by the next-generation detectors. DM rich environments have been shown to display different physical signatures depending on the underlying dark sector properties. We will make a global distinction between cold DM composed by particles generally heavier than the eV scale, which can be modelled by a fluid-like stress-energy tensor, and the set of light DM particles with masses orders of magnitude smaller than the eV scale, which require a field-theoretical treatment. These categories will be subject of the contributions in the main chapters of this thesis.

1.1.1 Fluid DM candidate

Cold DM modelled as a fluid solution to GR reproduce experimental evidence on large scales. On smaller scales, like galactic cores or compact stellar clusters, the DM dynamics is poorly understood, with tensions with respect to the ΛCDM model that could explained by baryonic physics or modifications to the DM paradigm. Sticking to the cold DM formalism, it has been argued that significant overdensities can grow around supermassive and intermediate mass black holes. The argument goes back to the work of Gondolo and Silk [120], showing that an isolated black hole growing slowly via accretion over a long timescale would redistribute the bound orbits of DM particles to form a steep density profile called *spike*. This process was invoked to propose the existence of spike profiles around galactic centres [216], but also around lighter intermediate mass black holes [226]. A compact object binary inspiraling into a DM spike interacts gravitationally with the dark fluid and experiences an effective dynamical friction (DF) force, which induces a phase shift of the emitted GWs with respect to an inspiral in a vacuum.

First estimates of this effect have been based on a Newtonian description of the spike profile and of the DF, while assuming a static DM profile during the binary evolution, and concluded that a large dephasing, detectable by instruments like LISA, is likely. [103]. More recent developments have refined the computation, including a detailed prescription for the matter evolution in phase space [144, 140] and relativistic effects via the development of BH perturbation theory over a non-vacuum background [67, 210, 68, 109, 185]. DF

effects have been implemented into modular state-of-the-art waveform generators such as `FastEMRIWaveform` [142, 210, 219]. When quantifying the DM impact in terms of change in the number of orbits in the inspiral compared to the vacuum case, including feedback into the halo dynamics and relativistic effects generally tends to reduce the effect with respect to the static Newtonian halo case, up to a two-orders of magnitude factor, while still yielding a measurable effect [86].

Other possible impacts of a fluid DM halo on a binary have been proposed, like the emergence of non-zero tidal effects because of the halo's response [69], non-trivial eccentricity evolution [37, 183, 225] and corrections to the remnant black hole ringing frequencies [67, 147, 190].

In chapter 2 we will discuss a specific model belonging to this class of DM candidates: an anisotropic fluid. We will discuss the adiabatic contraction argument and derive the DM spike associated to an initial galactic-like profile around a slowly growing Schwarzschild black hole. We will then compute the quasi-normal frequency modes of such spacetime in the odd sector of gravitational perturbations. We will discuss the tidal deformability of this spacetime and compute its tidal Love numbers. We obtain the Love numbers associated to all perturbation sectors. Chapter 2 is based on [78]. The work discussed in the chapter has been carried out in collaboration with Geoffrey Compère and Sumanta Chakraborty, with equally distributed contributions.

1.1.2 Light DM candidate

DM could be composed by bosonic particles with mass below the eV scale, with occupation numbers high enough to allow them to be described by classical field theory. Popular candidates in this category are light and ultra-light axions, axion-like particles and higher-spin fields like the dark photon [107]. This class of models has sparked interest in the literature because of their peculiar behaviour around highly spinning black holes driven only by the gravitational interaction. A light field can extract energy and angular momentum when scattering onto a Kerr black hole, growing a long-lived bosonic cloud around it via the *superradiance* mechanism [56]. The existence of such DM clouds can source several different signatures accessible to GW instruments.

As a result of the superradiant process, a particle cloud with a Hydrogen atom-like structure forms in the surroundings of the black hole, with a total mass that as high as 10% of the black hole one [34]. Because of cloud's growth, the host black hole would lose angular momentum, generating gaps in a mass-spin distribution of a black hole population, also known as Regge plane [96, 55, 101, 19], which could be investigated with a sufficient number of precise spin

measurements. Observing spinning black holes in a wide range of masses would allow probe an equally wide range of DM candidates' masses, as the superradiant process is sensitive to a specific combination of the black hole and particle mass. Another signatures are sourced by the cloud's dynamics, as transitions in the field's energy level and particle annihilations into gravitons can emit continuous GWs [57]. Finally, if the cloud is part of an asymmetric black hole binary system, energy exchanges in between the field and the secondary binary component can source sharp features in the inspiral evolution, as resonant or fast shrinking orbits, with a sizeable impact on the emitted waveform [38, 31, 32, 214, 58].

In the case of a more symmetrical black hole binary, numerical investigations have been carried out to study the behaviour of light fields on a dynamical spacetime. Numerical simulations typically cannot reproduce the emergence of a superradiant cloud, as its growth timescale is several order of magnitudes longer than what is achievable with reasonable computational resources. However, it was shown that massive fields can grow into a dense cloud from accretion onto an isolated black hole as well as onto a black hole binary [83, 28]. A binary evolving in this cloud will emit a signal dephased with respect to a vacuum one, because of DF and radial forces exerted by the cloud [27]. It has been shown that the dephasing is sensitive to the field mass for simple massive scalar field, with a maximal impact on the binary evolution for field's whose Compton wavelength are comparable to the binary separations in the latest stages of the inspiral [22].

In chapter 3 we introduce a class of light scalar fields with a non-trivial kinetic term coming from a nonlinear sigma model geometry of the field space. The theory admits a free parameter that quantifies the curvature of the scalar manifold and can be thought of a self-interaction term. We study the spherically symmetric solutions to the theory starting from an appropriate ansatz to the Einstein Field Equations solution. We discuss the properties of these solutions and interpret them as boson stars with compactness dependent on the field space curvature. We show that a positive curvature of the scalar manifold can generate compact objects of astrophysical scale. Chapter 3 is based on [66]. The work discussed in this chapter has been carried out in collaboration with Pablo Cano and Charlotte Mijn. I developed the numerical algorithm to identify the solutions to the theory's equations of motion.

In chapter 4 we use NR tools to study the aforementioned theories on a black hole spacetime. We simulate the accretion process onto an isolated Schwarzschild black hole and discuss its dependence of the field mass and field space curvature. We then simulate the last few orbits of an equal mass black hole binary inspiral with an initially uniform scalar field density. We characterize qualitatively the impact of the theories' parameters onto the scalar field cloud behaviour and onto the inspiral time and accumulated dephasing. Chapter 4 is based on [164]. This

work is mainly my own and was done in collaboration with Llibert Aresté Saló, who contributed with precious help in the setup of the numerical simulations with `GRChombo` and `GRTresna`.

Chapter 2

Quasi-normal modes and tidal Love numbers of the Schwarzschild-Hernquist black hole

2.1 Introduction

This chapter will focus on the case of fluid dark matter halos. It has been argued that fluid DM can grow to large densities in the neighbourhood of a seed BH, generating a characteristic spike profile. This model was derived in the pioneering work of Gondolo and Silk [120] and was generalised to a relativistic formalism in [205, 108]. The impact of such dark matter distribution on the inspiral phase of a BH binary evolution has been extensively studied, from first estimates in [103] to further work refined the computation, pointing out the importance of taking into account the dynamical evolution of the matter distribution [144, 86, 185]. Efforts are underway to build a self-consistent relativistic model of such system based on BH perturbation theory and efficient for waveform generation [67, 210, 211].

In this chapter, building upon this program, we will construct a fully relativistic model for an Hernquist matter distribution that surrounds a supermassive black hole, which complete the existing literature [205, 210]. We will develop the theory of perturbations around a spherically symmetric background sourced

by anisotropic matter and compare our equations with the literature [68, 159, 100]. We will then study two typical signatures of gravitational perturbations in the presence of matter: quasi-normal modes and tidal Love numbers. We will compare these quantities computed for a relativistic matter distribution to the values obtained in the literature when considering analytical models inspired by Newtonian physics.

The quasi-normal spectrum of a dressed BH is altered by the impact of the matter on the gravitational perturbations potential, which yields shifts in the resonant frequencies with respect to vacuum GR [67]. Black hole spectroscopy has received considerable attention as a key tool to investigate BH properties like the Kerr hypothesis as well as to uncover signatures of beyond-GR physics [39, 76, 65, 206, 178]. The detectability prospects of such shifts are currently uncertain [212]. A precise determination of the relativistic effects impact on these quantities is therefore necessary to discuss detectability and possible degeneracies with different theories. Likewise, the static tidal Love numbers of a BH identically vanish in vacuum GR for asymptotically flat spacetimes [50, 150, 48, 184, 47]. They are non-zero in the case the compact object is not a BH, for alternative theories to GR or for non-vacuum spacetimes [74, 69, 79]. In this work, we compute the electric-type (odd) and magnetic-type (even) Love numbers for a BH dressed by a relativistic spike. Non-zero tidal Love numbers will contribute to the dephasing of a compact object's inspiral into a BH-spike system, and could be constrained by LISA with high precision [188].

Through this work we will use geometrized units with $c = G = 1$, with the exception of 2.2, where we will write G explicitly.

2.2 Relativistic dark matter spike profiles

The first relativistic derivation of a spherically symmetric dark matter (DM) halo around a BH was performed in [205], considering a Schwarzschild background. The effects of relativistic rotation were included in [108] upon upgrading the background to the Kerr metric. In this work, we assume that the DM halo is composed of cold and collisionless particles modelled by an anisotropic gas. Thus, the DM particles interact only gravitationally and we do not include self-interactions or gravitational heating, which could deplete the density profile in its inner region [217, 208, 216, 174, 119, 44]. We will furthermore assume that a BH grows adiabatically at the centre of such halo, i.e. on a timescale much larger than the orbital timescale of the DM particles in the BH spacetime. Assuming the BH hole to sit at the centre of mass of the halo avoids complications due to its eventual motion around the system's barycentre and related accretion of DM

along this path. In the following sections we will start from a non-relativistic spherically symmetric distribution and perform the relaxation to a relativistic profile. We will focus on the Hernquist model as starting point of this process.

2.2.1 Spherically symmetric distribution functions

A collisionless gas of massive particles follows geodesic orbits. Assuming a small backreaction of the DM, the geometry is dictated by the central BH. Assuming spherical symmetry and Einstein gravity, the geometry is the Schwarzschild geometry. Let $u^\mu = \frac{dx^\mu}{d\tau}$ be the four-velocity and $p_\mu = \mu g_{\mu\nu} u^\nu$ the four-momentum of identical particles of mass μ and proper time τ, $g_{\mu\nu}u^\mu u^\nu = -1$. The free particle Hamiltonian is given by $H(x^\mu, p_\nu) = \frac{1}{2} g^{\mu\nu}(x) p_\mu p_\nu$. One can describe the gas by the phase space distribution function $f = f(x^\mu, p_\nu)$ normalized as $\int f\sqrt{-g} d^4p d^4x = \mu^4$. Liouville theorem states that for a collisionless gas f should be invariant along a geodesic, i.e.

$$\frac{\mathrm{d}}{\mathrm{d}\tau} f(x^\mu(\lambda), p_\nu(\lambda)) = \frac{\mathrm{d}x^\mu}{\mathrm{d}\lambda}\frac{\partial f}{\partial x^\mu} + \frac{\mathrm{d}p_\nu}{\mathrm{d}\lambda}\frac{\partial f}{\partial p_\nu} = \{H, f\} = 0. \tag{2.1}$$

This equation is known as the collisionless Boltzmann equation (CBE). For a given solution, the particle current density can be constructed as

$$J_\mu = \int f(x,p) p_\mu \sqrt{-g}\, \mathrm{d}^4 p, \tag{2.2}$$

and the mass density can be inferred as $\rho = \sqrt{-J_\mu J^\mu}$. A solution to the CBE can be obtained by finding an adapted phase space coordinate system that makes the equation trivial, so that the solution follows by a choice of boundary conditions. Adapted phase space coordinates are the relativistic angle-action variables (q^α, J_α) [132]. This method has been applied to a Schwarzschild spacetime for the study of accretion phenomena [198, 163]. In the case of spherically symmetric DM halos with a single component mass μ, we assume $f = \mu^{-4} f(E, L)\delta(\mu' - \mu)$ with $f(E, L)$ dimensionless where E, L are the energy per unit mass and the total angular momentum per unit mass. The angular momentum along the z-direction per unit mass L_z does not appear in the distribution function by SO(3) symmetry. The CBE is then automatically obeyed since $E = -u_t, L = \sqrt{u_\theta^2 + u_\phi^2 \sin^{-2}\theta}, L_z = u_\phi$ are constants of geodesic motion. Note that $E, L \geq 0$, $L_z \in \mathbb{R}$. After performing the coordinate change, integrating over μ and multiplying by a factor of 4 to take into account both signs of p_r, p_θ for given constants of motion, the particle current density becomes

$$J_\mu = 4 \int f(E, L) p_\mu \frac{L}{\sin\theta\sqrt{UR}} dE dL dL_z, \tag{2.3}$$

where $U = L^2 - L_z^2 \sin^{-2}\theta$, $R = E^2 r^4 - \Delta(r^2 + L^2)$, $\Delta = r^2 - 2M_{\rm BH} r$. The components J_r, J_θ are vanishing since bound orbits have a symmetric motion between positive and negative radial or polar velocities. The component J_ϕ also vanishes because the integrand is odd under sign reversal of L_z. The mass density is given by $\rho = -(1-2M_{\rm BH}/r)^{-1/2} J_t \mu^{-1} M_{DM}$ where we now normalize the mass with respect to the complete DM mass M_{DM} instead of the individual particle mass. Performing the integral over L_z one obtains

$$\rho(r) = 4\pi M_{DM} \left(1 - \frac{2M_{\rm BH}}{r}\right)^{-1/2} \int \frac{f(E,L)}{\sqrt{R}} E L dE dL, \tag{2.4}$$

which agrees with Eq. (3.15) of [205]. The range of integration of E, L is dictated by the region of existence of bounded orbits that reach r, which is known analytically. Such orbits only exist for $r \geq 4GM$ and therefore $\rho(r) = 0$ for $r \leq 4GM$. The energy is integrated in the range $E_{\rm min}(r) \leq E < 1$ with $E_{\rm min}(r) = (1 + 2GM_{\rm BH}/r)/\sqrt{1 + 6GM_{\rm BH}/r}$ for $r \geq 6GM_{\rm BH}$ and $E_{\rm min}(r) = (1 - 2GM_{\rm BH}/r)/\sqrt{1 - 3GM_{\rm BH}/r}$ for $4GM_{\rm BH} \leq r \leq 6GM_{\rm BH}$. The angular momentum lies in the range $L_{\rm min}(E) \leq L \leq L_{\rm max}(E, r)$ with $L^2_{\rm min}(E) = 32(GM_{\rm BH})^2/(36E^2 - 27E^4 - 8 + E(9E^2 - 8)^{3/2})$ and $L_{\rm max}(E, r) = r\sqrt{E^2/(1 - 2GM_{\rm BH}/r) - 1}$.

The relativistic profile $f(E, L)$ of a DM cloud around a Schwarzschild BH can be fixed by matching via the Eddington inversion method a non-relativistic profile $f' = f'(E'_N, L')$ obtained from N-body simulations without central BH to the relativistic profile with the central Schwarzschild BH [108]. Here E'_N is the non-relativistic energy related to the relativistic energy as $E' = 1 + E'_N$. Starting from a non-relativistic distribution $f'(E'_N, L')$ that generates a central Newtonian potential $\Phi(r)$, one can show that the adiabatic growth of a BH conserves the distribution function, i.e. $f(E, L) = f'(E'_N, L')$, together with the invariants I_r, I_ϕ and I_θ, given by

$$I_{r,N} = \frac{1}{2\pi\mu} \oint p_r {\rm d}r = \frac{1}{2\pi} \oint \sqrt{2E'_N - 2\Phi - \frac{L'^2}{r^2}}\, {\rm d}r, \tag{2.5}$$

$$I_{\theta,N} = \frac{1}{2\pi\mu} \oint p_\theta {\rm d}\theta = \frac{1}{2\pi} \oint \sqrt{L'^2 - \frac{L'^2_z}{\sin^2\theta}}\, {\rm d}\theta = L' - |L'_z|, \tag{2.6}$$

$$I_{\phi,N} = \frac{1}{2\pi\mu} \oint p_\phi {\rm d}\phi = \frac{1}{2\pi} \oint L'_z {\rm d}\phi = L'_z, \tag{2.7}$$

for a Newtonian system (where the radial integral is defined in between the two roots of the integrand) and by

$$I_{r,{\rm Schw}} = \frac{1}{2\pi\mu} \oint p_r {\rm d}r = \frac{1}{2\pi} \oint \frac{\sqrt{R(r)}}{\Delta(r)}\, {\rm d}r\ , \tag{2.8}$$

$$I_{\theta,\mathrm{Schw}} = \frac{1}{2\pi\mu}\oint p_\theta \mathrm{d}\theta = L - |L_z| \ , \tag{2.9}$$

$$I_{\phi,\mathrm{Schw}} = \frac{1}{2\pi\mu}\oint p_\phi \mathrm{d}\phi = L_z \ , \tag{2.10}$$

for general relativistic system described by the Schwarzschild metric with $R(r) = E^2 r^4 - \Delta(r^2 + L^2)$, $\Delta = r^2 - 2M_{\mathrm{BH}} r$ (Carter's constant is $Q = L^2 - L_z^2$)[1]. The angular momenta L', L'_z are automatically matched $L' = L$, $L'_z = L_z$ which is consistent for a spherically symmetric system, while the relativistic energy $E' = E'(E, L)$ is obtained from the matching equation $I_{r,N}(E'_N, L) = I_{r,\mathrm{Schw}}(E, L)$ once the Newtonian profile $\Phi(r)$ is given.

2.2.2 The Schwarzschild-Hernquist model

For definiteness, we take as a starting point in this work the Hernquist profile

$$\rho_{\mathrm{H}}(r_{\mathrm{s}}, \rho_0) = \frac{\rho_0}{(r/r_{\mathrm{s}})(1 + r/r_{\mathrm{s}})^3} \ , \tag{2.11}$$

which generates the Newtonian gravitational potential $\Phi_{\mathrm{H}}(r) = -(GM_{\mathrm{DM}}/r + r_{\mathrm{s}})$. Here, $M_{\mathrm{DM}} = 2\pi\rho_0 r_{\mathrm{s}}^3$ is the total DM mass in the halo. We can numerically evaluate the relativistic energy $E' = E'(E, L)$ to machine precision. Using Eddington's formula, the dimensionless ergodic distribution function for this model is given by (see e.g. Eq. (4.51) of [49]),

$$f_{\mathrm{H}}(\epsilon') = \frac{1}{\sqrt{2}(2\pi)^3 (GM_{\mathrm{DM}} r_{\mathrm{s}})^{3/2}} \frac{\sqrt{\epsilon'}}{(1-\epsilon')^2} \times \left[(1-2\epsilon')(8\epsilon'^2 - 8\epsilon' - 3) + \frac{3\sin^{-1}\sqrt{\epsilon'}}{\sqrt{\epsilon'(1-\epsilon')}}\right] , \tag{2.12}$$

where $\epsilon' \equiv -(E'-1) r_{\mathrm{s}}/GM_{\mathrm{DM}}$ is expressed in terms of the relativistic energy $E'(E, L)$.

Following [205], we can define the dimensionless quantities $\tilde{L} = L/\sqrt{r_{\mathrm{s}} GM_{\mathrm{DM}}}$, $\tilde{\epsilon} = (r_{\mathrm{s}}/GM_{\mathrm{DM}})(1-E)$ and re-express $\epsilon' = \epsilon'(\tilde{\epsilon}, \tilde{L})$. In terms of these quantities,

[1] We note that the invariant I_r^{BH} defined in Eq.(4) of [210] is incorrect since it misses a redshift factor. The error dates to the paper [205] where Eq. (3.19) for the Schwarzschild case is incorrect, while the formula Eq. (3.8) for the Kerr case is correct. This leads to a difference between the derivation of our results and the ones of [210] by a relative factor of $1 - 2M/6M = 2/3$ around the innermost stable circular orbit.

the mass density in Eq. (2.4) can be rewritten as

$$\rho = \frac{G^{3/2} M_{\rm DM}^{5/2}}{r_{\rm s}^{1/2}} \frac{2\pi}{r - 2GM_{\rm BH}} \int_0^{\tilde{\epsilon}_{\rm max}} {\rm d}\tilde{\epsilon} \left(1 - \frac{GM_{\rm DM}}{r_{\rm s}} \tilde{\epsilon}\right) \int_{\tilde{L}^2_{\rm min}}^{\tilde{L}^2_{\rm max}} {\rm d}\tilde{L}^2 \frac{f_{\rm H}(\epsilon'(\tilde{\epsilon}, \tilde{L})}{\sqrt{\tilde{L}^2_{\rm max} - \tilde{L}^2}} \,. \tag{2.13}$$

We compute numerically the density, given the above expression, for a reference system with parameters

$$M_{\rm DM} = 10^{12}\, M_\odot,\, M_{\rm BH} = 10^6\, M_\odot,\, r_{\rm s} = 20\,{\rm kpc}\,, \tag{2.14}$$

which correspond to a scale density of $\rho_0 = 0.76\,{\rm GeV/cm}^3$ and corresponds to plausible astrophysical values [224]. The result is shown on 2.1. The profile obtained from adiabatic contraction admits a sharp spike with cutoff at radius equal to twice the Schwarzschild radius $R_{\rm S} = 2GM_{\rm BH}$ (the location of the marginally bound circular orbit). We also note that the slope of the relativistic profile decreases at a much larger radius $r'_{\rm s}$ than the original $r_{\rm s}$. For the purpose of the subsequent discussion, we have defined the dimensionless variable $x \equiv r/(GM_{\rm BH})$. Numerical investigations show that the parameter $x'_{\rm s}$ can be expressed as a combination of other parameters of the problem

$$x'_{\rm s} = \frac{2r_{\rm s} M_{\rm DM}}{GM^2_{\rm BH}}\,, \tag{2.15}$$

which approximates the fitted values of $x'_{\rm s}$ up to 10 % error. This has been also recently obtained in [211]. In the following, we will keep the notation $x'_{\rm s}$ for compactness of the relativistic Schwarzschild-Hernquist profile.

We fit the data via the `NonLinearModelFit` method of `Mathematica` to the following model,

$$\rho = \bar{\rho}(x)\lambda := \bar{\rho}(x) \left(\frac{M_{DM}}{10^{12}\, M_\odot}\right)^{\alpha} \left(\frac{M_{\rm BH}}{10^6\, M_\odot}\right)^{\beta} \left(\frac{r_s}{20\, kpc}\right)^{\gamma}, \tag{2.16}$$

with the radial dependence of the density profile being,

$$\bar{\rho}(x) = A \left(1 - \frac{4}{x}\right)^{w} x^{-q} \left(1 + \frac{x}{x'_s}\right)^{q-4}. \tag{2.17}$$

The $(\alpha,\, \beta,\, \gamma)$ coefficients are obtained by varying one parameter at a time while keeping the two other fixed. The best-fit values of the $(A,\, w,\, q, \alpha,\, \beta,\, \gamma)$ coefficients are given in 2.1.

It follows that our model approximates the numerical result up to a maximum of 10 % error between the fitted model and the numerically obtained data, on

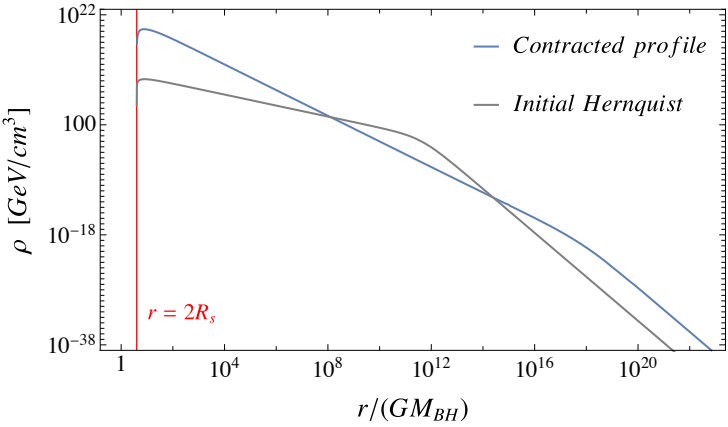

Figure 2.1: DM spike generated by adiabatic contraction from the non-relativistic Hernquist profile. The original profile is shown in gray. The spike has a sharp cutoff at the marginally bound circular orbit, located at radius $2R_{\rm S} = 4M_{\rm BH}$.

	Best fit
A [GeV/cm^3]	1.85×10^{22}
w	2.45
q	2.33
α	0.33
β	-1.66
γ	-0.67

Table 2.1: Best fit parameters, namely $(A, w, q, \alpha, \beta, \gamma)$, for the Schwarzschild-Hernquist BH model, presented in Eq. (2.16).

nearly the whole range of radii. The polynomial ansatz, presented in Eq. (2.16) is motivated by the simple model proposed in [210] but contains one important modification. The last term in Eq. (2.17) is inserted to correctly account for the behaviour of the DM at large radius. Indeed, the profile ought to asymptote to the initial Hernquist power-law profile far away from the region controlled by the adiabatic contraction of the spike, i.e., $\rho \sim r^{-4}$ for $r \gg r_{\rm s}$. This is due to the fact that orbits living at such large distances from the core of the halo will be not perturbed significantly by the adiabatic growth of the central BH.

The three-parameter model, as advocated in Eq. (2.16) with coefficients given in 2.1 is our proposal for the complete relativistic DM profile obtained from the

adiabatic contraction of the Hernquist profile, which we call the Schwarzschild-Hernquist model. It depends upon the total DM mass $M_{\rm DM}$, the BH mass $M_{\rm BH}$ and the Hernquist shape parameter $r_{\rm s}$.

We point out that the spike slope we obtain is slightly but significantly steeper than what was concluded in [210]. They obtained $q = 1.90$ while we obtain $q = 2.33$. We also point out that the γ coefficient $\gamma = 0.31$ obtained in [210] is very different than the one that we obtain namely $\gamma = -0.67$. A negative value of γ is in fact physically motivated: for higher values of r_s and fixed halo mass M_{DM} the DM density gets effectively diluted, with smaller densities for short radii. Thus, an increase in the Hernquist scale radius should yield a smaller density after adiabatic contraction. The discrepancies with the parameters given in [210] come from the fact that the fit performed in that reference is valid only for radii of order $r < \mathcal{O}(10R_S)$, while it deviates significantly from the contracted profile for larger radii. The analysis carried out in this work requires to consistently model the DM distribution over the whole spacetime. For example, if one was to assume the model given in [210] to be valid up to infinity, the total mass of the spike $M_{DM} = \int_{2R_S}^{\infty} {\rm d}r\, 4\pi r^2 \rho(r)$ would be infinite. Our model compares well with the recent one proposed in [211] while this part of our work was finished. The main difference is the fitted value of γ which slightly differs.

Proceeding further, given the density profile for the DM distribution, the total mass enclosed in a radius r is given by,

$$m(r) = \frac{\pi}{2} R_S^3 \lambda \int^r {\rm d}x\, x^2 \bar{\rho}(x)\,, \tag{2.18}$$

where we have collected into the λ factor all the scaling terms in equation (2.16). We checked that the total mass of the halo differs from the mass of the initial Hernquist profile by only 10% using the fitted parameters given in 2.1. Inserting Eq. (2.17) into Eq. (2.18) and using the fact that $x'_s \gg 4$, we obtain the analytic mass density of the Schwarzschild-Hernquist BH model as

$$m_{\rm SH}(r) = M_{\rm BH} + \lambda R_S^3 \tilde{A}\, {}_2F_1\left(w+1, q+w-2; w+2; -\frac{(x-4)x'_s}{4(x+x'_s)}\right)\Theta(x-4)\,, \tag{2.19}$$

with, $x = 2r/R_S$, $\Theta(x)$ being the Heaviside step function and the factor $\tilde{A}$ being,

$$\tilde{A} = \frac{A\,\pi\, x'^4_{\rm s}\, 4^{-q-w+2}}{2(w+1)} \frac{(x-4)^{w+1}}{(x'_{\rm s}+4)^4} \left(\frac{x+x'_{\rm s}}{x'_{\rm s}}\right)^q \left(\frac{x'_{\rm s}+4}{x+x'_{\rm s}}\right)^{q+w+1}\,. \tag{2.20}$$

The above mass profile is plotted in Figure 2.2. Let us remark that the density distribution in Eq. (2.17) vanishes at $x = 4$, the radius of the marginally bound

circular orbit. For $2 < x < 4$, the mass of the spacetime is that of the central BH, and for $x \gg x'_{\rm s}$, it is given by the total mass $(M_{\rm DM} + M_{\rm BH})$.

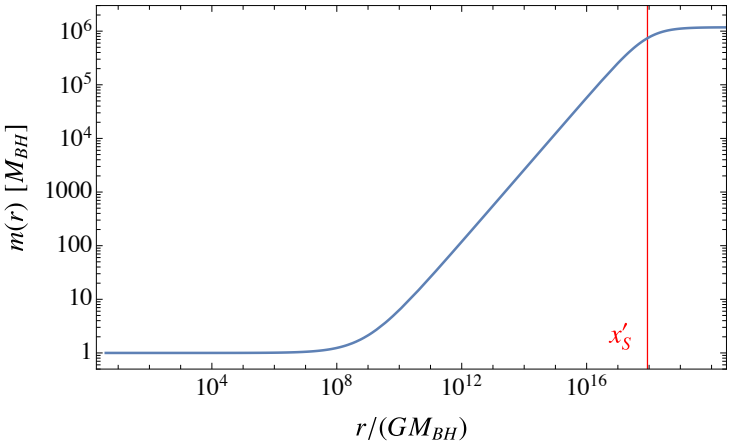

Figure 2.2: We have plotted the mass distribution in the relativistic DM spike profile in units of the central BH mass for the Schwarzschild-Hernquist model considered above. As evident, for lower radius, the mass profile asymptotes to the mass of the central BH, while at larger radius, it asymptotes to the total mass of the system $(M_{\rm DM} + M_{\rm BH})$.

2.2.3 Effective spherically symmetric metric and light-rings

We now convert the information about the matter distribution into an effective metric describing the DM surrounding the BH. This can be constructed via an effective averaging of the stress-energy tensor of an ensemble of particles following geodesics on the BH spacetime, given by a matter density $\bar{\rho}$ [104, 117, 67]. Under the simplifying assumption that the eccentricity of such geodesics can be neglected, this can be shown to be equivalent to requiring an anisotropic stress-energy tensor with no radial pressure,

$$T^{\nu}_{\mu} = \text{diag}(-\bar{\rho}, 0, \bar{p}_t, \bar{p}_t)\,, \tag{2.21}$$

which can be coupled to a spherically symmetric metric ansatz via the Einstein equations. Writing,

$$\overline{\mathrm{d}s}^2 = -f(r)\mathrm{d}t^2 + \frac{1}{g(r)}\mathrm{d}r^2 + r^2\mathrm{d}\Omega^2\,, \qquad g(r) := 1 - \frac{2m(r)}{r}\,, \tag{2.22}$$

with $m(r)$ being the mass enclosed in a radius r, one gets the following equation relating the metric components

$$\frac{rf'(r)}{f(r)} = \frac{2m(r)}{r-2m(r)}, \tag{2.23}$$

whereas the tangential pressure and the density are related by the following relation

$$2\bar{p}_t = \frac{m(r)\bar{\rho}(r)}{r-2m(r)}, \qquad \bar{\rho}(r) = \frac{m'(r)}{4\pi r^2}\,. \tag{2.24}$$

These equations are consistent with [68].

A direct consequence of Eq. (2.23) is the equality

$$r - 3m(r) = -\frac{\{r-2m(r)\}\,r^3}{2f}\frac{d}{dr}\left(\frac{f}{r^2}\right)\,. \tag{2.25}$$

Therefore the existence of a light-ring (or anti-light-ring [91]) in such a geometry, *i.e.*, a locus r such that $\partial_r(f/r^2) = 0$, is equivalently a locus where

$$r = 3m(r)\,. \tag{2.26}$$

Since the matter density vanishes for radii below the standard light-ring $r = 3M_{\rm BH}$, the standard light-ring is present in the geometry. Motivated by recent studies [123], let us study whether a second light-ring might be present. The null, weak and strong energy conditions [126] are obeyed given that $\bar{\rho}$ and $\bar{p}_t$ are non-negative in the exterior region $r > 2m$. The dominant energy condition reduces to the condition $\bar{\rho} \geq \bar{p}_t$. The constraint only applies when matter is present, for $r \geq 4M_{\rm BH}$ and it reduces to

$$r \geq \frac{5}{2}m(r)\,. \tag{2.27}$$

Comparing the existence of a (anti-)light-ring, as in Eq. (2.26), and the dominant energy condition constraint (2.27), we see that there is a very small window where a light-ring located within matter could exist. However, the dominant energy condition would be only marginally obeyed. This is therefore a very extreme situation which is not physically realistic. We performed a numerical check assuming the Schwarzschild-Hernquist density (2.16). We obtained that one would need to scale down r_s in the baseline model (2.14) as $r_s \mapsto 2.5 \times 10^{-10} r_s$ to achieve such a scenario, which would imply unrealistic DM densities. In that scenario, the pressure $\bar{p}_t$ is enhanced and its value gets closer to the density $\bar{\rho}$, see 2.3. We therefore conclude that for realistic parameters, there will be one and only one lightring at $r = 3M_{\rm BH}$. More general matter models are described

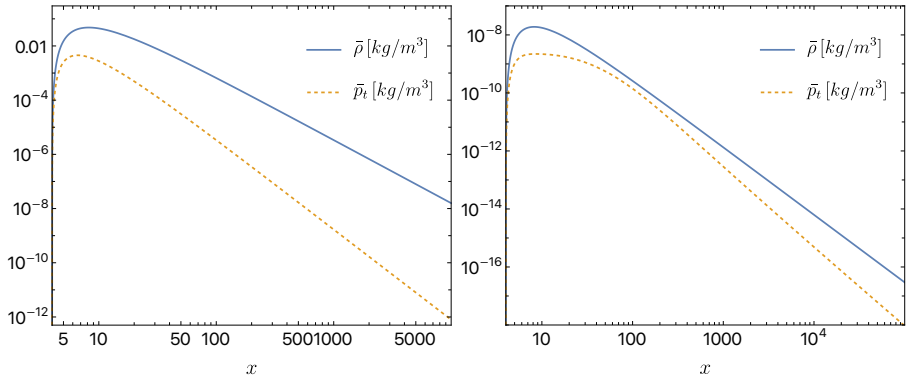

Figure 2.3: Left: Density (solid line) and pressure (dashed line) for the Schwarzschild-Hernquist BH with realistic values (2.14). Right: Density (solid line) and pressure (dashed line) for the Schwarzschild-Hernquist BH with rescaled factor $r_s \mapsto 2.5 \times 10^{-10} r_s$ and other factors unchanged. The latter matter distribution does not violate the dominant energy condition while the metric admits two light rings and one anti-light ring.

by an anisotropic fluid with radial pressure,

$$T_{\mu\nu} = \bar{\rho}\bar{u}_\mu\bar{u}_\nu + \bar{p}_{\rm r}\bar{v}_\mu\bar{v}_\nu + \bar{p}_{\rm t}\bar{\Pi}_{\mu\nu} \ , \tag{2.28}$$

where, $\bar{u}_\mu\bar{u}^\mu = -1$, $\bar{v}_\mu\bar{v}^\mu = +1$, and $\bar{v}_\mu\bar{u}^\mu = 0$, with $\Pi_{\mu\nu} = \bar{g}_{\mu\nu} + \bar{u}_\mu\bar{u}_\nu - \bar{v}_\mu\bar{v}_\nu$. We take $\bar{u}_\mu = -\sqrt{f(r)}\delta^t_\mu$ and $\bar{v}^\mu = \sqrt{g(r)}\delta^\mu_r$. Implying, $\bar{u}^\mu = \{1/\sqrt{f(r)}\}\delta^\mu_t$ and $\bar{v}_\mu = \{1\sqrt{g(r)}\}\delta^r_\mu$. In this case, the Einstein's equations and the conservation of the stress-energy tensor are equivalent to the following three equations

$$\bar{\rho}(r) = \frac{m'(r)}{4\pi r^2} \ , \qquad \frac{f'(r)}{f(r)} = -\frac{2(m(r) + 4\pi\bar{p}_{\rm r}(r)r^3)}{r(2m(r) - r)} \ , \tag{2.29}$$

$$\begin{aligned}\bar{p}_{\rm t}(r) = &-\frac{2r\bar{p}_{\rm r}(r)(1 + 2\pi r^2(\bar{p}_{\rm r}(r) + \bar{\rho}(r)))}{4m(r) - 2r} \\ &- \frac{r^2\bar{p}'_{\rm r}(r) + m(r)(3\bar{p}_{\rm r}(r) - \bar{\rho}(r) + 2r\bar{p}'_{\rm r}(r))}{4m(r) - 2r}.\end{aligned} \tag{2.30}$$

The generic solution is given in terms of the (arbitrary) radial mass aspect $m(r)$ and the radial pressure $\bar{p}_{\rm r}(r)$. These equations disagree with Ref. [100] (see equation (9.6) of this paper). In the case $\bar{p}_{\rm r} = 0$, we recover Eqs. (2.23)-(2.24).

2.3 Perturbed Einstein's equations in the presence of matter

Having discussed the background geometry as well as the matter content, describing a BH immersed in a non-relativistic/relativistic DM distribution, in this section we discuss the perturbation of the same. This involves perturbations of the geometry, described by $\delta g_{\mu\nu}$, as well as perturbation of the matter, captured by $\delta T_{\mu\nu}$. The corresponding equations relating the perturbed metric to the perturbed matter sector, are the linearized Einstein's equations:

$$\delta G_{\mu\nu} = 8\pi G \delta T_{\mu\nu} \ , \tag{2.31}$$

and the perturbed conservation equation for the matter stress-energy tensor, i.e.,

$$\delta \left(\nabla_\mu T^{\mu\nu} \right) = 0 \ . \tag{2.32}$$

In what follows we will present the perturbed matter stress-energy tensor, as well as the perturbed Einstein tensor, in terms of certain fundamental observables associated with the matter and the metric. We start with the perturbed matter stress-energy tensor and shall decompose it into axial and polar parts.

2.3.1 Perturbation of the matter stress-energy tensor

Given the fact that the background matter distribution was anisotropic ($p_r = 0 \neq p_t$), it only makes sense to write down the perturbed stress-energy tensor of an anisotropic fluid, which takes the following form

$$T_{\mu\nu} = \rho u_\mu u_\nu + p_{\rm r} v_\mu v_\nu + p_{\rm t} \Pi_{\mu\nu} \ , \tag{2.33}$$

where $u_\mu u^\mu = -1$, $v_\mu v^\mu = +1$, $v_\mu u^\mu = 0$ and $\Pi_{\mu\nu} = g_{\mu\nu} + u_\mu u_\nu - v_\mu v_\nu$. Here, the metric is perturbed as $g_{\mu\nu} = \bar{g}_{\mu\nu} + h_{\mu\nu}$ and the scalars as $\rho = \bar{\rho} + \delta\rho$, $p_{\rm t} = \bar{p}_{\rm t} + \delta p_{\rm t}$, $p_{\rm r} = \bar{p}_{\rm r} + \delta p_{\rm r}$. Note that, the above anisotropic stress-energy tensor can describe the DM halo, provided we set $\bar{p}_r = 0$. The perturbations of the fluid four-velocity u^μ and the auxiliary four-vector v^μ are defined as variations of the contravariant components of the respective fluid vectors,

$$u^\mu = \bar{u}^\mu + \delta u^\mu, \qquad v^\mu = \bar{v}^\mu + \delta v^\mu \, . \tag{2.34}$$

The perturbations of the covariant components of the fluid vectors are instead given by

$$\delta(u_\mu) = h_{\mu\nu} u^\nu + \bar{g}_{\mu\nu} \delta u^\nu, \qquad \delta(v_\mu) = h_{\mu\nu} v^\nu + \bar{g}_{\mu\nu} \delta v^\nu \, . \tag{2.35}$$

Due to the metric perturbation, it is in general not equivalent to impose either $\delta u^\mu = 0$ or $\delta(u_\mu) = 0$. We will refer to the first choice as the 'up' choice and refer to the second choice as the 'down' choice for cancelling the variation of the fluid vector. It corresponds to physically different dynamics for the fluid.

2.3.2 Perturbation equations: odd sector

The odd metric perturbations in Regge-Wheeler gauge are defined in the standard fashion as

$$h_{t\theta} = h_{\theta t} = -\frac{h_0(t,r)}{\sin\theta}\partial_\phi Y_{\ell m}, \qquad h_{t\phi} = h_{\phi t} = h_0(t,r)\sin\theta\partial_\theta Y_{\ell m}, \tag{2.36}$$

$$h_{r\theta} = h_{\theta r} = -\frac{h_1(t,r)}{\sin\theta}\partial_\phi Y_{\ell m}, \qquad h_{r\phi} = h_{\phi r} = h_1(t,r)\sin\theta\partial_\theta Y_{\ell m}. \tag{2.37}$$

Besides the metric perturbations, as presented above, there will also be perturbations associated with the fluid elements, in particular the fluid four-velocity u^μ and orthogonal vector field v^μ. In the axial sector, perturbations of each of them will introduce one extra degree of freedom. However, it turns out that these perturbation variables have different values for $\delta v^\mu = 0$, compared to $\delta v_\mu = 0$. As a consequence, the master equations describing the QNMs as well as the static TLNs are different, depending on whether the perturbation of the covariant or, the contravariant components of v^μ have been set to zero. Following which we discuss these two cases separately and describe them as the 'down' and the 'up' definitions, respectively.

The 'up' master equations

The only odd perturbations in the matter sector are the odd perturbations of δu^μ and δv^μ, which are given by

$$\delta u^\theta = -\frac{\sqrt{f(r)}}{4\pi(\bar{p}_t+\bar{\rho})r^2}\frac{U^{\rm up}(r)e^{-i\omega t}}{\sin\theta}\partial_\phi Y_{\ell m}\,,$$

$$\delta u^\phi = \frac{\sqrt{f(r)}}{4\pi(\bar{p}_t+\bar{\rho})r^2\sin^2\theta}U^{\rm up}(r)e^{-i\omega t}\sin\theta\,\partial_\theta Y_{\ell m}\,, \tag{2.38}$$

$$\delta v^\theta = -\frac{\sqrt{g(r)}}{4\pi(\bar{p}_t+\bar{\rho})r^2}\frac{V^{\rm up}(r)e^{-i\omega t}}{\sin\theta}\partial_\phi Y_{\ell m}\,,$$

$$\delta v^\phi = \frac{\sqrt{g(r)}}{4\pi(\bar{p}_t+\bar{\rho})r^2\sin^2\theta}V^{\rm up}(r)e^{-i\omega t}\sin\theta\,\partial_\theta Y_{\ell m}\,. \tag{2.39}$$

Therefore, the perturbed non-zero components of the matter stress-energy tensor associated with the axial perturbation become,

$$\delta T^{\rm axial}_{t\phi} = e^{-i\omega t}\left[-\frac{fU^{\rm up}}{4\pi} - \bar{\rho}h_0(r)\right]\sin\theta\partial_\theta Y_{\ell m}\ , \tag{2.40}$$

$$\delta T^{\rm axial}_{t\theta} = -e^{-i\omega t}\left[-\frac{fU^{\rm up}}{4\pi} - \bar{\rho}h_0(r)\right]\frac{\partial_\phi Y_{\ell m}}{\sin\theta}\ , \tag{2.41}$$

$$\delta T^{\rm axial}_{r\phi} = e^{-i\omega t}\left[\bar{p}_r h_1(r) + \frac{(\bar{p}_r - \bar{p}_t)V^{\rm up}}{4\pi(\bar{\rho}+\bar{p}_t)}\right]\sin\theta\partial_\theta Y_{\ell m}\ , \tag{2.42}$$

$$\delta T^{\rm axial}_{r\theta} = -e^{-i\omega t}\left[\bar{p}_r h_1(r) + \frac{(\bar{p}_r - \bar{p}_t)V^{\rm up}}{4\pi(\bar{\rho}+\bar{p}_t)}\right]\frac{\partial_\phi Y_{\ell m}}{\sin\theta}\ . \tag{2.43}$$

One can verify that the above components of the perturbed matter stress-energy tensor identically satisfies Eq. (2.32).

Substituting these components to the right hand side of Eq. (2.31), and using the perturbed Einstein tensor from the metric perturbation described above, we obtain three independent differential equations, these correspond to the (θ,ϕ), (r,ϕ) and (t,ϕ) components of Eq. (2.31), respectively. The (θ,ϕ) component of the perturbed Einstein's equations is homogeneous and relates h_0 with h_1,

$$-i\omega h_0 - \sqrt{fg}\frac{d}{dr}\left(\sqrt{fg}h_1\right) = 0\ . \tag{2.44}$$

After using the above equation and the tortoise coordinate $dr_* \equiv dr/\sqrt{fg}$, the (r,ϕ) component of the perturbed Einstein's equation can be written as the Regge-Wheeler equation with source for the function $\Psi_{\rm RW}(r_*) = (\sqrt{fg}/r)h_1$,

$$\frac{d^2\Psi_{\rm RW}}{dr_*^2} + \left[\omega^2 - V^{\rm up}_{\rm RW}\right]\Psi_{\rm RW} = \frac{4f\sqrt{fg}}{r}\left(\frac{\bar{p}_{\rm t} - \bar{p}_{\rm r}}{\bar{\rho}+\bar{p}_{\rm t}}\right)V^{\rm up}\ , \tag{2.45}$$

where,

$$\begin{aligned} V^{\rm up}_{\rm RW}(r) &= f\left[\frac{\ell(\ell+1)}{r^2} - \frac{6m}{r^3} + 4\pi(\bar{\rho} + 4\bar{p}_{\rm t} - 5\bar{p}_{\rm r})\right] \\ &= f\left[\frac{\ell(\ell+1)}{r^2} - \frac{3}{2r}\left(g' + g\frac{f'}{f}\right) + 8\pi\left(-\bar{\rho} - \bar{p}_{\rm r} + 2\bar{p}_{\rm t}\right)\right]\ . \end{aligned} \tag{2.46}$$

The third and the final perturbed Einstein's equation comes from the (t,ϕ) component of Eq. (2.31), which can be written as,

$$g\left[h_0'' + i\omega\left(h_1' + \frac{2}{r}h_1\right)\right] - 4\pi r\left(\bar{p}_{\rm r} + \bar{\rho}\right)\left(h_0' + i\omega h_1\right)$$

$$-\left[\frac{(\ell+2)(\ell-1)}{r^2}+\frac{2g}{r^2}+8\pi\left(\bar{\rho}-\bar{p}_{\rm r}+2\bar{p}_{\rm t}\right)\right]h_0=4fU^{\rm up}\,. \tag{2.47}$$

In summary, the three non-trivial field equations in the context of axial perturbations are given by the Eqs. (2.44), (2.45) and (2.47). Even though, we have three equations, there are four unknowns to solve for, namely $\Psi_{\rm RW}$, h_0, $U^{\rm up}$ and $V^{\rm up}$. Thus, to close the system of equations, additional conditions are necessary and we simply set $\delta v^\mu=0$. Since v^μ is an auxiliary vector, the above can always be achieved. This sets to zero the source terms in Eq. (2.45). Thus, one can obtain the homogeneous solution for $\Psi_{\rm RW}$ from the master equation and reconstruct h_0 from Eq. (2.44), while Eq. (2.47) would provide an expression for $U^{\rm up}$. Therefore, the system of equations governing axial perturbations of gravity plus fluid system becomes closed and hence exactly solvable.

The 'down' master equations

In the previous section, in order to close the system of equations, we had set $\delta v^\mu=0$. However, it is also possible to close the system of equations by simply setting $\delta v_\mu=0$. In this case, the off-diagonal terms in the metric perturbations give

$$V^{\rm up}=-4\pi(\bar{\rho}+\bar{p}_{\rm t})h_1\ . \tag{2.48}$$

Thus, it is natural to rewrite Eqs. (2.45) as

$$\frac{d^2\Psi_{\rm RW}}{dr_*^2}+\left[\omega^2-V_{\rm RW}^{\rm down}\right]\Psi_{\rm RW}=0\ , \tag{2.49}$$

where, we have the modified potential,

$$V_{\rm RW}^{\rm down}(r)=f\left[\frac{\ell(\ell+1)}{r^2}-\frac{6m}{r^3}+4\pi(\bar{\rho}-\bar{p}_{\rm r})\right]\ . \tag{2.50}$$

Thus solving the homogeneous equation in Eq. (2.50), leads to the Regge-Wheeler function, then Eq. (2.44) yields h_0, while Eq. (2.47) still gives $U^{\rm up}$ in terms of h_0.

We note that for a background isotropic fluid distribution, with $\bar{p}_{\rm r}=\bar{p}_{\rm t}$, we have $V_{\rm RW}^{\rm up}(r)=V_{\rm RW}^{\rm down}(r)$. Thus, only for a background anisotropic fluid, the potentials of the Regge-Wheeler equation will differ between the 'up' and the 'down' definitions. This implies that the QNM spectrum will also differ, depending on whether one fixes $\delta v^\mu=0$ or $\delta v_\mu=0$. We now move on to determining the perturbation equations in the even sector.

2.3.3 Perturbation equations: even sector

The even metric perturbations in the Regge-Wheeler gauge are defined in the standard fashion as

$$h_{tt} = e^{-i\omega t} f(r) H_0(r) Y_{\ell m} \ , \qquad h_{tr} = h_{rt} = e^{-i\omega t} H_1(r) Y_{\ell m} \ ,$$

$$h_{rr} = e^{-i\omega t} \frac{H_2(r)}{g(r)} Y_{\ell m} \ , \qquad h_{\theta\theta} = e^{-i\omega t} r^2 K(r) Y_{\ell m} \ ,$$

$$h_{\phi\phi} = e^{-i\omega t} r^2 \sin^2\theta K(r) Y_{\ell m} \ . \tag{2.51}$$

The perturbed stress-energy tensor associated with the matter distribution has already been defined in Eq. (2.33). In the even sector, all the scalar perturbations will contribute, which are described with the following variables:

$$\delta\rho(t,r,\theta,\phi) = e^{-i\omega t} \delta\rho(r) Y_{\ell m} \ , \tag{2.52}$$

$$\delta p_{\rm t}(t,r,\theta,\phi) = e^{-i\omega t} \delta p_{\rm t}(r) Y_{\ell m} \ , \tag{2.53}$$

$$\delta p_{\rm r}(t,r,\theta,\phi) = e^{-i\omega t} \delta p_{\rm r}(r) Y_{\ell m} \ . \tag{2.54}$$

In order to close our system of equations, and to avoid unnecessary complications, we shall not consider arbitrary variations of the vectors u^μ, v^μ. Further, as we will demonstrate, unlike the case of axial perturbations, here there is no difference between the 'up' and the 'down' components for the polar sector.

We start by considering perturbations of the contravariant components of the fluid four-vector u^μ and the auxiliary four-vector v^μ, such that, the non-zero components of δu^μ and δv^μ are,

$$\delta u^t = \frac{H_0(r)}{2\sqrt{f}} Y_{\ell m} e^{-i\omega t} \ , \qquad \delta u^r = \frac{g}{\sqrt{f} r^2} \frac{D^{\rm up}(r) Y_{\ell m}}{16\pi(\bar\rho + \bar p_r)} e^{-i\omega t} \ ,$$

$$\delta u^\theta = \frac{\sqrt{f} C^{\rm up}(r) \partial_\theta Y_{\ell m}}{4\pi r^2 (\bar\rho + \bar p_t)} e^{-i\omega t} \ , \qquad \delta u^\phi = \frac{\sqrt{f} C^{\rm up}(r) \partial_\phi Y_{\ell m}}{4\pi r^2 \sin^2\theta (\bar\rho + \bar p_t)} e^{-i\omega t} \ ,$$

$$\delta v^t = \frac{\sqrt{g}}{f} \left[\frac{D^{\rm up}}{16\pi r^2 (\bar\rho + \bar p_r)} + H_1 \right] Y_{\ell m} e^{-i\omega t} \ , \quad \delta v^r = -\frac{\sqrt{g} H_2}{2} Y_{\ell m} e^{-i\omega t} \ ,$$

$$\delta v^\theta = \delta v^\phi = 0 \ . \tag{2.55}$$

Note that, given the spherical symmetry of the background geometry, it follows that the perturbed vectors δu^μ and δv^μ are each characterized by three independent even harmonics. Among these six variables, three are fixed

in terms of metric perturbations, thanks to the following three constraints: $\delta(u^\mu u_\mu) = 0$, $\delta(u^\mu v_\mu) = 0$, and $\delta(v_\mu v^\mu) = 0$. Among the other three variables, we have $D^{\rm up}$ and $C^{\rm up}$, while the sixth one, associated with the δv^θ and δv^ϕ components, has been set to zero for simplicity. Note that unlike the axial sector, here the components of δu^μ and δv^μ are related to metric perturbations and hence cannot be set to zero.

The 'down' components, i.e., the components of δu_μ and δv_μ, on the other hand, reads,

$$\delta u_t = \frac{\sqrt{f} H_0(r)}{2} Y_{\ell m} \ , \qquad \delta u_r = \frac{H_1}{\sqrt{f}} + \frac{D^{\rm up}(r) Y_{\ell m}}{16\pi r^2 \sqrt{f}(\bar\rho + \bar p_r)} \ ,$$

$$\delta u_\theta = e^{-i\omega t} \frac{\sqrt{f} C^{\rm up}}{4\pi(\bar\rho + \bar p_t)} \partial_\theta Y_{\ell m} \ , \qquad \delta u_\phi = e^{-i\omega t} \frac{\sqrt{f} C^{\rm up}}{4\pi(\bar\rho + \bar p_t)} \partial_\phi Y_{\ell m} \ ,$$

$$\delta v_t = -\frac{\sqrt{g} D^{\rm up}}{16\pi r^2(\bar\rho + \bar p_r)} Y_{\ell m} \ , \qquad \delta v_r = \frac{H_2}{2\sqrt{g}} Y_{\ell m} \ ,$$

$$\delta v_\theta = \delta v_\phi = 0 \ . \tag{2.56}$$

In the Regge-Wheeler gauge, the polar sector perturbations do not contain cross terms between the (t, r) and (θ, ϕ) metric perturbations, thus, if we set $\delta v^\mu = 0$, it follows that $\delta v_\mu = 0$. Hence there is no distinction between 'up' and the 'down' master equations for the polar sector.

Given the metric perturbations, as well as fluid perturbations, the non-zero components of the perturbed matter stress-energy tensor in the polar sector become,

$$\delta T^{\rm polar}_{tt} = e^{-i\omega t} \left[f\delta\rho - f H_0 \bar\rho \right] Y_{\ell m} \ , \tag{2.57}$$

$$\delta T^{\rm polar}_{tr} = -e^{-i\omega t} \left[\frac{D^{\rm up}}{16\pi r^2} + \bar\rho H_1 \right] Y_{\ell m} \ , \tag{2.58}$$

$$\delta T^{\rm polar}_{rr} = e^{-i\omega t} \left[\frac{\delta p_r}{g} + \frac{\bar p_r H_2}{g} \right] Y_{\ell m} \ , \tag{2.59}$$

$$\delta T^{\rm polar}_{t\theta} = e^{-i\omega t} \left[-\frac{f C^{\rm up}(r)}{4\pi} \right] \partial_\theta Y_{\ell m} \ , \tag{2.60}$$

$$\delta T^{\rm polar}_{t\phi} = e^{-i\omega t} \left[-\frac{f C^{\rm up}(r)}{4\pi} \right] \partial_\phi Y_{\ell m} \ , \tag{2.61}$$

$$\delta T^{\rm polar}_{\theta\theta} = e^{-i\omega t} \left[r^2 \delta p_t + r^2 \bar p_t K(r) \right] Y_{\ell m} = {\rm cosec}^2\theta \, \delta T^{\rm polar}_{\phi\phi} \ . \tag{2.62}$$

One can verify that the above expressions exactly match with those reported in [68].

Having presented the non-zero perturbed components of the matter stress-energy tensor, we now report the perturbed Einstein's equations associated with the polar perturbation. We summarize these equations below.

- We start with the (θ, ϕ) component of the perturbed Einstein's equations which directly yields

$$H_0(r) = H_2(r) \equiv H(r) \ , \tag{2.63}$$

  after factoring out the overall factors depending on $e^{-i\omega t}$ and spherical harmonics. The subtraction of the (θ, θ) and $\csc^2\theta$ times the (ϕ, ϕ) components of the perturbed Einstein's equations yields the same equation.

  We will assume that Eq. (2.63) is obeyed in order to simplify the remaining perturbed Einstein's equations in what follows.

- The (t, t) component of the perturbed Einstein's equations read (with H_2 replaced by H),

$$K'' + \left(\frac{3}{r} + \frac{g'}{2g}\right) K' - \frac{(\ell-1)(\ell+2)}{2r^2 g} K - \frac{H'}{r} - \left(\frac{\ell(\ell+1) + 2 - 16\pi r^2 \bar{\rho}}{2r^2 g}\right) H = -\frac{8\pi\delta\rho}{g} \ . \tag{2.64}$$

- The (t, r) component of the perturbed Einstein's equations become (with H_2 replaced by H),

$$i\omega K' - \frac{i\omega}{r} H + \frac{\ell(\ell+1)}{2r^2} H_1 + \frac{i\omega}{2rg}\left(-8\pi r^2 \bar{p}_r + 3g - 1\right) K = -\frac{1}{2r^2} D^{\rm up} \ . \tag{2.65}$$

- The (r, r) component of the perturbed Einstein's equations yield (with $H_2 = H_0 = H$),

$$gH' + \frac{2i\omega g}{f} H_1 - \frac{\omega^2 r}{f} K + \frac{(\ell-1)(\ell+2)}{2r}(K - H) + 8\pi r \bar{p}_r H - \frac{8\pi r^2 \bar{p}_r + 1 + g}{2} K' = -8\pi r \delta p_r \ . \tag{2.66}$$

- The $(\theta,\theta)+(\phi,\phi)$ component of the perturbed Einstein's equations yield (with $H_2 = H_0 = H$),

$$g\left(H'' - K''\right) + \frac{2i\omega g}{f}H_1' + \frac{H'}{r}\left\{-4\pi r^2\left(\bar{\rho} - 3\bar{p}_r\right) + 2\right\}$$
$$+ \frac{K'}{r}\left\{4\pi r^2\left(\bar{\rho} - \bar{p}_r\right) - (1+g)\right\} - \frac{\omega^2}{f}\left(K + H\right)$$
$$+ \frac{i\omega}{rf}\left\{-8\pi r^2\bar{\rho} + 1 + g\right\}H_1 + 16\pi\bar{p}_t H = -16\pi\delta p_t \ . \tag{2.67}$$

- The (t,θ) component yields,

$$gH_1' + i\omega\left(K + H\right) + \left\{1 - g - 4\pi r^2\left(\bar{\rho} - \bar{p}_r\right)\right\}\frac{H_1}{r} = -4fC^{\rm up} \ . \tag{2.68}$$

- The (r,θ) component yields,

$$H' - K' + \frac{i\omega}{f}H_1 + \frac{1 - g + 8\pi r^2\bar{p}_r}{rg}H = 0 \ . \tag{2.69}$$

- The (t,ϕ) and (r,ϕ) components will yield identical equations. Hence no new equations can be obtained.

Besides the perturbed Einstein's equations, we also require equations for the matter sector, which are obtained by considering the components of Eq. (2.32), yielding:

- The t component of the perturbed conservation equation reads

$$\delta\rho = \left(\frac{g}{16\pi i\omega r^2}\right)D^{\rm up'} + \left(\frac{gf' + fg'}{32\pi i\omega r^2 f}\right)D^{\rm up} - \left(\frac{\ell(\ell+1)f}{4\pi i\omega r^2}\right)C^{\rm up}$$
$$- \frac{\bar{\rho} + \bar{p}_r}{2}H - \left\{\frac{(\bar{\rho} + \bar{p}_r)(1 + 3g + 8\pi r^2\bar{p}_r)}{4g} + \frac{r\bar{p}_r'}{2}\right\}K \ . \tag{2.70}$$

- The r component of the perturbed conservation equation reads

$$\delta p_r' = \left(\frac{i\omega}{16\pi r^2 f}\right)D^{\rm up} - \left(\frac{4f + rf'}{2rf}\right)\delta p_r + \left(\frac{2}{r}\right)\delta p_t - \left(\frac{f'}{2f}\right)\delta\rho$$
$$+ \left(\frac{i\omega(\bar{p}_r + \bar{\rho})}{f}\right)H_1 + \left(\frac{\bar{p}_r + \bar{\rho}}{2}\right)H' + \left[\frac{r\bar{p}_r'}{2} + \frac{(\bar{\rho} + \bar{p}_r)rf'}{4f}\right]K \ . \tag{2.71}$$

- The θ and the ϕ component of the perturbed conservation equation yields identical results, which read

$$\delta p_t - \frac{i\omega}{4\pi} C^{\rm up} - \frac{\bar{\rho} + \bar{p}_r}{2} H = 0 \ . \tag{2.72}$$

Thus in total we have *nine* equations, *six* from the gravitational sector and *three* from the matter sector. We also have *eight* unknowns to fix — (a) the gravitational perturbation yields *three* unknowns: K, H_1 and H, (b) the perturbation of the matter sector has *five* unknowns: $\delta\rho$, δp_r, δp_t, $D^{\rm up}$ and $C^{\rm up}$. Thus it might appear that the system if equations over determine the system of unknowns, however, as we will demonstrate that is not the case.

Master system of equations for polar perturbations

Let us now determine the master system of equations in the context of polar gravitational perturbation. First of all, in the present situation, we already have $H_0 = H_2 \equiv H(r)$, and the following four first order differential equations

$$K' - \frac{H}{r} + \frac{\ell(\ell+1)}{2i\omega r^2} H_1 + \left(\frac{-8\pi r^2 \bar{p}_r + 3g - 1}{2rg} \right) K = -\frac{1}{2i\omega r^2} D^{\rm up} \ , \tag{2.73}$$

$$H' + \frac{2i\omega}{f} H_1 - \frac{\omega^2 r}{fg} K + \frac{(\ell-1)(\ell+2)}{2rg} (K - H) + \frac{8\pi r \bar{p}_r}{g} H - \frac{8\pi r^2 \bar{p}_r + 1 + g}{2g} K' = -\frac{8\pi r \delta p_r}{g} \ , \tag{2.74}$$

$$H_1' + \frac{i\omega}{g} (K + H) + \left\{ 1 - g - 4\pi r^2 (\bar{\rho} - \bar{p}_r) \right\} \frac{H_1}{rg} = -\frac{4f}{g} C^{\rm up} \ , \tag{2.75}$$

$$H' - K' + \frac{i\omega}{f} H_1 + \frac{1 - g + 8\pi r^2 \bar{p}_r}{rg} H = 0 \ . \tag{2.76}$$

In addition, there are two second order differential equations, that we will analyse later on. Substitution of K' from Eq. (2.73) to Eq. (2.76) yields the following equation,

$$H' + \left(\frac{-8\pi r^2 \bar{p}_r + 3g - 1}{2rg} \right) K + \left[\frac{\ell(\ell+1)}{2i\omega r^2} + \frac{i\omega}{f} \right] H_1 + \left(\frac{1 - 2g + 8\pi r^2 \bar{p}_r}{rg} \right) H = -\frac{D^{\rm up}}{2i\omega r^2} \ . \tag{2.77}$$

Substitution of the above expression for H' in Eq. (2.74), yields the following algebraic relation between these three gravitational perturbation quantities,

$$\left[\ell(\ell+1)+16\pi r^2\bar{p}_r-\frac{2\omega^2r^2}{f}-\frac{3g}{2}-\frac{\left(1+8\pi r^2\bar{p}_r\right)^2}{2g}\right]K$$
$$+\left[\frac{2i\omega rg}{f}+\frac{\ell(\ell+1)(8\pi r^2\bar{p}_r+1-g)}{2i\omega r}\right]H_1$$
$$-\left[(\ell+2)(\ell-1)+8\pi r^2\bar{p}_r+3(1-g)\right]H=-16\pi r^2\delta p_r+\frac{D^{\rm up}}{2i\omega r}\left(g-1-8\pi r^2\bar{p}_r\right)\ . \tag{2.78}$$

This implies that the perturbation variable H can be expressed in terms of $(K, H_1, \delta p_r, D^{\rm up})$ and hence we are left with three independent first order equations. However, we can now substitute the algebraic solution $H = H(K, H_1, \delta p_r, D^{\rm up})$ into Eq. (2.74), which can be shown to be equivalent with the equation obtained after using the other two first order equations as well as the matter equations, namely Eqs. (2.70) and (2.71). Thus, one of the first order equation, in particular Eq. (2.74), is therefore redundant.

The remaining two second order perturbation equations in the gravitational sector, as presented in Eq.(2.64) and Eq.(2.67) can be shown to be compatible with the first order equations, provided two additional constraints are satisfied. After analysis, these two additional constraints are found to be nothing else than the matter equations, Eqs. (2.70) and (2.72), respectively. The second order equations are therefore also redundant and hence can be discarded.

In summary, we are left with two algebraic equations: one from the matter sector, Eq. (2.72), and one from the Einstein sector, Eq. (2.78), as well as four first order equations: two from the matter sector, Eqs. (2.70) and (2.71), and two from the Einstein sector, let us say Eqs. (2.73) and (2.75). We choose to solve these equations for the variables K, H_1, $\delta\rho$ and $D^{\rm up}$ and to algebraically solve the two constraints for H and $C^{\rm up}$ (which is valid for non-vanishing frequency modes). Hence we have *six* equations in total, but *eight* variables. This issue of having more variables than equations is resolved by providing the equations of state

$$\delta p_r = c_s^{(r)}\delta\rho\ , \qquad \delta p_t = c_s^{(t)}\delta\rho\,. \tag{2.79}$$

which determines δp_t and δp_r as a function of $\delta\rho$. Choices for the sound speeds $c_s^{(r)}$ and $c_s^{(t)}$ close the system of equations.

We would like to point out that a similar set of equations have also been derived in [181], albeit in the connection with the f-mode oscillation of anisotropic

neutron stars. The parametrization of the metric and matter perturbations, considered in [181], are different from those presented in this work, and hence the perturbation equations are not directly related with each other.

To investigate the possibility of deriving a second-order master differential equation for polar perturbation with matter, alike the axial case, we first determine a system of two differential equations of first order that depends solely on the gravitational perturbations K and H_1, describing the even perturbations, along with source terms. For that purpose, we have solved for $H(r)$ from Eq. (2.78) and then have substituted the same in the differential equations for K, in Eq. (2.73), yielding,

$$K' = \left[\alpha_0(r) + \alpha_2(r)\omega^2\right] K + \left[\beta_0(r) + \beta_2(r)\omega^2\right] \left(\frac{H_1}{\omega}\right) + S_{\rm K} \tag{2.80}$$

with the following definitions for the functions $\alpha_0(r)$, $\alpha_2(r)$, $\beta_0(r)$, $\beta_2(r)$, and $S_{\rm K}$ respectively, as (defining, $\gamma_\ell \equiv (\ell-1)(\ell+2)$ in subsequent expressions),

$$\alpha_0 \equiv \frac{\gamma_\ell \left(1 - g + 8\pi r^2 \bar{p}_r\right)}{2rg\left[\gamma_\ell + 8\pi r^2 \bar{p}_r + 3(1-g)\right]} - \frac{(1-g)\left(3g - 1 - 8\pi r^2 \bar{p}_r\right)}{rg\left[\gamma_\ell + 8\pi r^2 \bar{p}_r + 3(1-g)\right]} \,, \tag{2.81}$$

$$\alpha_2 \equiv -\frac{2r}{f\left[\gamma_\ell + 8\pi r^2 \bar{p}_r + 3(1-g)\right]} \,, \tag{2.82}$$

$$\beta_0 \equiv -\frac{(\gamma_\ell + 2)\left\{\gamma_\ell + 2(1-g)\right\}}{2ir^2\left[\gamma_\ell + 8\pi r^2 \bar{p}_r + 3(1-g)\right]} \,, \tag{2.83}$$

$$\beta_2 \equiv \frac{2ig}{f\left[\gamma_\ell + 8\pi r^2 \bar{p}_r + 3(1-g)\right]} \,, \tag{2.84}$$

$$S_{\rm K} = \frac{16\pi r \delta p_r}{\gamma_\ell + 8\pi r^2 \bar{p}_r + 3(1-g)} - \frac{D^{\rm up}\left[\gamma_\ell + 2(1-g)\right]}{2i\omega r^2\left[\gamma_\ell + 8\pi r^2 \bar{p}_r + 3(1-g)\right]} \,. \tag{2.85}$$

On the other hand, substitution of H from Eq. (2.78) in the differential equation for H_1, as in Eq. (2.75), yields the following first order differential equation for H_1,

$$\frac{H_1'}{\omega} = \left[\kappa_0(r) + \kappa_2(r)\omega^2\right] K + \left[\delta_0(r) + \delta_2(r)\omega^2\right] \left(\frac{H_1}{\omega}\right) + S_{H1}, \tag{2.86}$$

where, the coefficients κ_0, κ_2, δ_0, δ_2 and the source term S_{H1} becomes,

$$\kappa_0 \equiv -\frac{i\left[4\gamma_\ell g + 16\pi r^2 g\bar{p}_r + 6g(1-g) - \left(3g - 1 - 8\pi r^2 \bar{p}_r\right)\left(g - 1 - 8\pi r^2 \bar{p}_r\right)\right]}{2g^2\left[\gamma_\ell + 8\pi r^2 \bar{p}_r + 3(1-g)\right]} \,, \tag{2.87}$$

$$\kappa_2 \equiv \frac{2ir^2}{fg\left[\gamma_\ell + 8\pi r^2 \bar{p}_r + 3(1-g)\right]} \ , \tag{2.88}$$

$$\delta_0 \equiv -\frac{1-g-4\pi r^2\left(\bar{\rho}-\bar{p}_r\right)}{rg} - \frac{\left(\gamma_\ell+2\right)\left(8\pi r^2\bar{p}_r+1-g\right)}{2rg\left[\gamma_\ell + 8\pi r^2 \bar{p}_r + 3(1-g)\right]} \ , \tag{2.89}$$

$$\delta_2 \equiv \frac{2r}{f\left[\gamma_\ell + 8\pi r^2 \bar{p}_r + 3(1-g)\right]} \ , \tag{2.90}$$

$$S_{H1} \equiv -\frac{4fC^{\rm up}}{g\omega} - \frac{16\pi i r^2 \delta p_r}{g\left[\gamma_\ell + 8\pi r^2 \bar{p}_r + 3(1-g)\right]} + \frac{D^{\rm up}(g-1-8\pi r^2\bar{p}_r)}{2gr\omega\left[\gamma_\ell + 8\pi r^2 \bar{p}_r + 3(1-g)\right]} \ . \tag{2.91}$$

It is interesting to point out that we have the following useful relations:

$$\delta_2 = -\alpha_2, \qquad \kappa_2 = -\frac{\alpha_2^2}{\beta_2} \ . \tag{2.92}$$

Therefore, instead of the three equations, namely Eq.(2.73), Eq.(2.75) and Eq.(2.78) one can simply use the system of two first order equations presented in Eqs. (2.80) and (2.86). This corresponds to the master system of equations for the even perturbations of a spherically symmetric metric.

On the other hand, if we demand the existence of a single master function $\Psi_{\rm Z}$, such that,

$$K = \alpha(r)\Psi_{\rm Z} + \beta(r)\frac{d\Psi_{\rm Z}}{dr_*} \ , \tag{2.93}$$

$$\frac{H_1}{\omega} = \kappa(r)\Psi_{\rm Z} + \delta(r)\frac{d\Psi_{\rm Z}}{dr_*} \ , \tag{2.94}$$

where, the tortoise coordinate r_* is defined as $(dr/dr_*) \equiv \sqrt{fg}$, and, if we further demand that $\Psi_{\rm Z}$ must satisfy an equation of the form

$$\frac{d^2\Psi_{\rm Z}}{dr_*^2} = \left[V_{\rm Z} - \omega^2\right]\Psi_{\rm Z} + S_Z \ , \tag{2.95}$$

we obtain an obstruction as long as $f\partial_r g - g\partial_r f \neq 0$. This obstruction disappears in the Schwarzschild case, where $f = g$ and hence one can define the Zerilli function and its associated potential. We refer the reader to appendix A.1, where the Schwarzschild case is reviewed. Unfortunately, in the presence of matter, there is no generalization of the Zerilli master function for generic even perturbations. We have also investigated whether a third order master equation of the form

$$\frac{d^2\Psi_{\rm Z}}{dr_*^2} + \left[A_Z + B_Z\omega^2\right]\frac{d\Psi_{\rm Z}}{dr_*} = \left[V_{\rm Z} - \omega^2\right]\Psi_{\rm Z} + S_Z \ , \tag{2.96}$$

would exist and found a negative result, which contradicts the claims of [159]. For clarity, the third order term is $\omega^2(d\Psi_{\rm Z}/dr_*)$, which reads in time domain as $(\partial^3\Psi_{\rm Z}/\partial t^2\partial r_*)$. Our proof amounts to show that Eqs. (2.93) - (2.94) and (2.96) lead to a contradiction as long as $f\partial_r g - g\partial_r f \neq 0$, or equivalently, as long as f is not proportional to g. The proof is given in a Mathematica sheet in this Github repository. Our result implies that the third order master equations described in [159] are gauge dependent.

Zero frequency modes

Let us study the static modes, which are defined as the modes with $\omega = 0$ in the frequency domain, and are important for the study of TLNs. We will concentrate on the $\ell \geq 2$ modes, as our interest is in the gravitational perturbations. First of all, the 'θ' component of the matter equations give

$$\delta p_t = \frac{\bar{\rho} + \bar{p}_r}{2} H \,. \tag{2.97}$$

The (t, r) components of the perturbed Einstein equations imply that

$$H_1 = -\frac{1}{\ell(\ell+1)} D^{\rm up} \,. \tag{2.98}$$

The (t, θ) components of the perturbed Einstein equations or, equivalently, the t component of the perturbed matter equations then relates two matter perturbations as

$$\ell(\ell+1) C^{\rm up} = \frac{g}{4f} D^{\rm up\prime} + \frac{1 - g + 4\pi r^2(\bar{p}_r - \bar{\rho})}{4rf} D^{\rm up}. \tag{2.99}$$

We solve these three algebraic equations for $\delta p_{\rm t}$, H_1 and $C^{\rm up}$. Note that the 't' component of the perturbed matter conservation equation, i.e., Eq. (2.70), in the static limit, does not provide any new equation, rather is identical to Eq. (2.99). Finally, the 'r' component of the perturbed matter conservation equation, presented in Eq. (2.71), in the static limit, allows us to solve for $\delta\rho = \delta\rho[K', H, H', \delta p_r, \delta p_r']$. Explicitly, the corresponding expression reads,

$$\left(\frac{f'}{2f}\right)\delta\rho = -\left(\frac{1 + 3g + 8\pi r^2 \bar{p}_r}{2rg}\right)\delta p_r + \left(\frac{\bar{p}_r + \bar{\rho}}{r}\right) H - \delta p_r' + \left(\frac{\bar{p}_r + \bar{\rho}}{2}\right) H' + \left[\frac{r\bar{p}_r'}{2} + \frac{(\bar{\rho} + \bar{p}_r)(1 - g + 8\pi r^2 \bar{p}_r)}{4g}\right] K' \,. \tag{2.100}$$

Thus we have exhausted all the equations arising from the matter sector.

Turning now, to the perturbations equations from the gravitational sector, we first express the static limit of the (r,θ) and the (r,r) components, yielding two first order differential equations for H and K,

$$K' - H' + \frac{g - 1 - 8\pi r^2 \bar{p}_r}{rg} H = 0\,, \tag{2.101}$$

$$H' - \frac{1 + g + 8\pi r^2 \bar{p}_r}{2g} K' - \frac{(\ell-1)(\ell+2) - 16\pi r^2 \bar{p}_r}{2rg} H + \frac{(\ell+2)(\ell-1)}{2rg} K = -\frac{8\pi r}{g} \delta p_r\,. \tag{2.102}$$

One can first algebraically solve Eq. (2.101) for K', substitute in Eq. (2.102) and solve for K. This yields,

$$K = \left[\frac{1 - g + 8\pi r^2 \bar{p}_r}{(\ell-1)(\ell+2)}\right](rH') + \left[\frac{(\ell-1)(\ell+2)g - 16\pi g r^2 \bar{p}_r + (1 + 8\pi r^2 \bar{p}_r)^2 - g^2}{(\ell-1)(\ell+2)g}\right] H - \frac{16\pi r^2}{(\ell-1)(\ell+2)} \delta p_r\,. \tag{2.103}$$

The compatibility of the solutions for K' and K, along with the 'r' component of the perturbed matter conservation equation, then leads to a second order differential equation for the metric perturbation $H(r)$, yielding,

$$H'' + \frac{1 + g + 4\pi r^2(\bar{p}_r - \bar{\rho})}{rg} H' + H\left[\frac{d}{dr}\left(\frac{1 - g + 8\pi r^2 \bar{p}_r}{rg}\right) + \frac{(1 - g + 8\pi r^2 \bar{p}_r)\{2g - 4\pi r^2(\bar{\rho} + \bar{p}_r)\}}{r^2 g^2} - \frac{\ell(\ell+1) - 8\pi r^2(\bar{\rho} + \bar{p}_r)}{r^2 g}\right] + \frac{8\pi(\delta\rho + \delta p_r)}{g} = 0\,. \tag{2.104}$$

The above differential equation for $H(r)$ can also be obtained via the following two routes — (a) $g \times (t,t)$ component $+(\theta,\theta + \phi,\phi)$ component $+ (g/r) \times (r,r)$ component, as well as (b) (t,t) component $+ (1/rg) \times (r,r)$ component. Note that both of these uses the second order differential equations for H and for K. Of course, Eq. (2.101) can be used to eliminate any K' in the above equations.

It turns out that both of these methods yield the above equation, where Eq. (2.97) needs to be used.

Note that we still need a relation between $\delta\rho$ and δp_r, in order to close the above equations. However, then one needs to solve the second order equation for H, given by Eq. (2.104) and the first order equation for $\delta\rho$, given by Eq. (2.100), together. In order to close the system of equations, given that we are interested in a DM halo distribution, we now assume that the radial sound speed $c_s^{(r)}$ is identically zero, which implies $\delta p_{\rm r} = 0$. For simplicity of this presentation and consistency with the DM profile considered in this chapter, we further take $\bar{p}_{\rm r} = 0$ from now on. In which case, we obtain the following equation for $\delta\rho$, in terms of H and H',

$$\frac{\delta\rho}{\bar{\rho}} = \left(\frac{1-2g+5g^2}{2(1-g)g}\right) H + \left(\frac{r(1+g)}{2(1-g)}\right) H' \ . \tag{2.105}$$

Note that the above equation can also be expressed in terms of K and H in the following manner:

$$\begin{aligned}\delta\rho =& \frac{(\ell+2)(\ell-1)g(\bar{\rho}+2\bar{p}_t)}{(g-1)^2} K \\ & - \frac{\bar{\rho}+g^2(\bar{\rho}-4\bar{p}_t)+g\{2\ell(\ell+1)\bar{p}_t+(\ell^2+\ell-4)\bar{\rho}\}}{(g-1)^2} H \ .\end{aligned} \tag{2.106}$$

To see the equivalence between these two equations for $\delta\rho$, one simply needs to use the relation, $2\bar{p}_t = \{(1-g)\bar{\rho}/2g\}$. Substituting the above solution for $\delta\rho$, along with $\bar{p}_r = 0 = \delta p_r$, in Eq. (2.104), we obtain the final differential equation for the metric perturbation H,

$$\begin{aligned}& H'' + \left(\frac{1+g}{rg} + \frac{16\pi r\bar{p}_t}{1-g} + \frac{4\pi r(1-3g)\bar{\rho}}{g(g-1)}\right) H' \\ & + \left(-\frac{1+(\ell+2)(\ell-1)g+g^2}{r^2g^2} + \frac{32\pi\bar{p}_t}{g} + \frac{16\pi\bar{\rho}}{g(1-g)}\right) H = 0 \ ,\end{aligned} \tag{2.107}$$

which can also be expressed in the following suggestive form using background Einstein's equations:

$$\begin{aligned}& H'' + \left(\frac{1+g}{rg} + \frac{8\pi r\bar{\rho}}{1-g}\right) H' \\ & + \left(-\frac{1+(\ell+2)(\ell-1)g+g^2}{r^2g^2} + \frac{8\pi\bar{\rho}(1+g^2)}{g^2(1-g)}\right) H = 0 \ .\end{aligned} \tag{2.108}$$

This is the master equation for static even modes in the case $\bar{p}_r = 0 = \delta p_r$, which we will solve to find out the electric type TLNs associated with the gravitational perturbation of a non-rotating BH immersed in a DM halo. We now move on to the discussion of the two observables, the QNMs and the TLNs.

2.4 Quasi-normal modes of the Schwarzschild-Hernquist BH

Having presented all the relevant equations associated with both the matter and the gravitational perturbations, in this section we will discuss one of the observable associated with perturbation of a BH spacetime, namely the quasi-normal modes (QNMs). We will discuss the QNMs in the odd sector only. We will compare their values for the non-relativistic Hernquist profile versus the relativistic Schwarzschild-Hernquist profile.

In the odd sector, one can introduce a Regge-Wheeler-like master function, and hence the master equation for the odd sector can be reduced to the following form

$$\frac{d^2\Psi_{\rm RW}}{dr_*^2} + \left[\omega^2 - V_{\rm RW}^{\rm up/down}\right]\Psi_{\rm RW} = 0 \ , \tag{2.109}$$

where, $\Psi_{\rm RW} = (\sqrt{fg}/r)h_1$, and the expressions for the potentials $V_{\rm RW}^{\rm up/down}$ have been presented in Eqs. (2.46) and (2.50), respectively. The asymptotic solutions to this equation take the form $\Psi_{\rm RW} \sim \exp(\pm i\omega r_*)$ and correspond to modes propagating outwards and inwards at spatial infinity and at the horizon. The quasi-normal mode eigenvalue problem is defined by requiring the modes to be purely outgoing at infinity and purely ingoing at the horizon. Explicitly, the boundary conditions read

$$\Psi_{\rm RW} \sim \begin{cases} e^{i\omega r}, \ r \to \infty, \\ (r - r_{\rm H})^{-i\omega r_{\rm H}}, \ r \to r_{\rm H} \, . \end{cases} \tag{2.110}$$

Here, $r_{\rm H}$ denotes the location of the event horizon. Once such boundary conditions are imposed, Eq. (2.109) admits a discrete set of complex eigenvalues, which are referred to as the QNMs.

Following the boundary conditions and the master equation for the axial sector, we have solved numerically for the QNM frequencies for the $\ell = 2$ mode using a sixth-order WKB approximation method [148]. We compared the QNM frequencies derived from the Schwarzschild-Hernquist model, presented in 2.2.2, to the ones obtained from the analytical model derived in [67] based on the

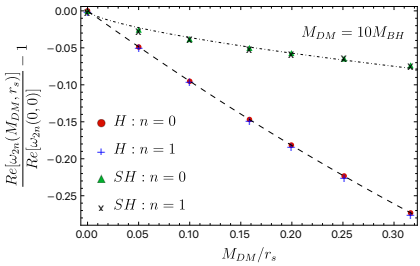

(a) Shift of the real part of the QNM frequency for $M_{\rm DM} = 10M_{\rm BH}$.

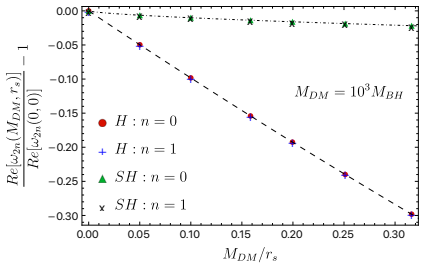

(b) Shift of the real part of the QNM frequency for $M_{\rm DM} = 10^3 M_{\rm BH}$.

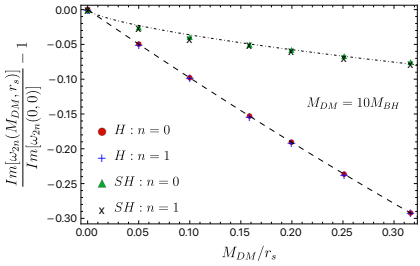

(c) Shift of the imaginary part of the QNM frequency for $M_{\rm DM} = 10M_{\rm BH}$.

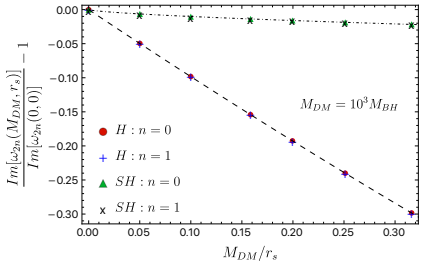

(d) Shift of the imaginary part of the QNM frequency for $M_{\rm DM} = 10^3 M_{\rm BH}$.

Figure 2.4: Shifts in the $\ell = 2$ mode frequency for the fundamental ($n = 0$) and the first overtone ($n = 1$) for both the Hernquist and Schwarzschild-Hernquist halos as a function of M_{DM}/r_s: (a) real part shift with $M_{DM} = 10M_{\rm BH}$; (b) real part shift with $M_{DM} = 10^3 M_{\rm BH}$; (c) imaginary part shift with $M_{DM} = 10M_{\rm BH}$; (d) imaginary part shift with $M_{DM} = 10^3 M_{\rm BH}$. The dashed lines are the best linear fits for the Hernquist model; the dot-dashed lines are the best fits for the Schwarzschild-Hernquist model.

Hernquist density profile. Both the Hernquist and the Schwarzschild-Hernquist models for DM only depend upon two dimensionless parameters ($M_{\rm DM}/M_{\rm BH}$), and ($r_{\rm s}/M_{\rm BH}$). In 2.4 we have plotted the relative shift of the $\ell = 2$ QNM frequencies $\omega_{2n}(M_{\rm DM}, r_{\rm s})$, with respect to the Schwarzschild value $\omega_{2n}(0, 0)$ for the fundamental mode $n = 0$ and for the first overtone $n = 1$. The plotted values were obtained from the 'down' perturbation definition. For the Hernquist DM halo, the frequency shifts are linear in the dimensionless ratio ($M_{\rm DM}/r_{\rm s}$), i.e.

$$\frac{\omega_{2n}(M_{DM}, r_s)}{\omega_{2n}(0,0)} - 1 = -\frac{M_{DM}}{r_s} + \mathcal{O}\left(\frac{M_{DM}^2}{r_s^2}\right) . \tag{2.111}$$

This results can be understood in terms of the correction to the light ring

frequency, which in the WKB approximation relates directly to the quasi-normal mode frequency, see e.g. [73, 67] for more details. In the case of the Schwarzschild-Hernquist distribution, the shifts can instead be fitted with a power law

$$\frac{\omega_{2n}(M_{DM}, r_s)}{\omega_{2n}(0,0)} - 1 = -c \left(\frac{M_{DM}}{r_s}\right)^{3/2} + \mathcal{O}\left(\frac{M_{DM}^2}{r_s^2}\right), \tag{2.112}$$

with, $c = c(M_{\rm DM})$ is some mass-dependent coefficient. We have numerically derived that c can be well approximated as $c(M_{\rm DM}) = (1/2)\, M_{\rm DM}^{-1/3}$ over a large parameter range. This, along with the scaling in Eq. (2.112), are one of the main results of this chapter.

To summarize, in the case of Hernquist DM density profile, the shifts in the QNM frequency show a universal scaling with the ratio $(M_{\rm DM}/r_{\rm s})$, whereas in the case of Schwarzschild-Hernquist profile, the scaling with $(M_{\rm DM}/r_{\rm s})$ is different, and in addition it is weighted by the mass-dependent term $c(M_{\rm DM})$. This is summarised in 2.5. It is important to mention that the same scaling emerges while studying the variation to the light ring frequency $\Omega_{\rm LR} \equiv (\sqrt{f(r_{\rm LR})}/r_{\rm LR})$ as a function of the Schwarzschild-Hernquist halo parameters. Intriguingly, the above scaling holds true for both the real as well as the imaginary part of the QNM frequency.

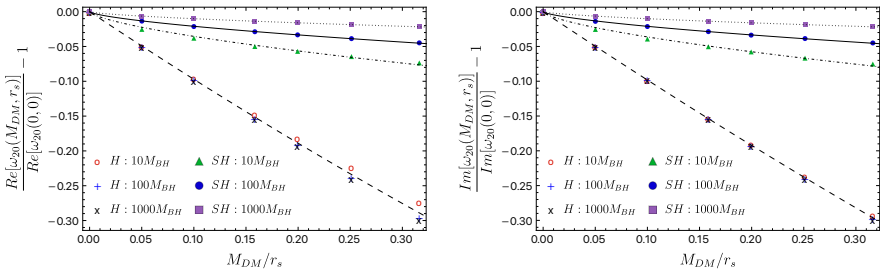

(a) Relative shift in the real part of the QNM frequency compared to the Schwarzschild BH.

(b) Relative shift in the imaginary part of the QNM frequency compared to the Schwarzschild BH.

Figure 2.5: The shift in the $\ell = 2$, $n = 0$ mode frequency for the Hernquist and Schwarzschild-Hernquist DM halos as a function of the dimensionless ratio $(M_{\rm DM}/r_{\rm s})$: (a) relative real part shift; (b) relative imaginary part shift, both with respect to their Schwarzschild value.

We showed in 2.3.2 that the effective potential of the Regge-Wheeler equation depends upon how the fluid four-velocity is being perturbed. Depending on whether, $\delta u^\mu = 0$, or, $\delta u_\mu = 0$, we have two different effective potentials,

given by Eqs. (2.46) and (2.50). This suggests that these two definitions will give distinct QNM spectrum. In Figure 2.6 we plot the relative differences in between the 'up' and 'down' frequencies for the fundamental mode as well as two overtones. The discrepancy in between the two potentials is of order 0.1 % and it is suppressed when the DM halo mass increases.

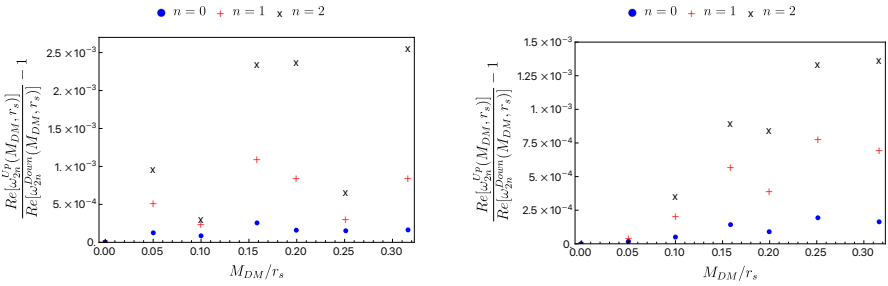

Figure 2.6: Relative difference in the real part of the $\ell = 2$ mode frequencies between the 'up' and the 'down' sector for the fundamental ($n = 0$), first ($n = 1$) and second ($n = 2$) overtone for the Schwarzschild-Hernquist DM halo profile as a function of the dimensionless ratio ($M_{\rm DM}/r_{\rm s}$) for different DM masses: (a) $M_{\rm DM} = 10M_{\rm BH}$, (b) $M_{\rm DM} = 100M_{\rm BH}$

Let us finally mention how one could obtain the QNMs in the even sector. In 2.3.3 we have obtained four coupled ordinary differential equations for the metric perturbations K, H_1, and the matter perturbations $\delta\rho$ and $D^{\rm up}$. In the range $2M_{\rm BH} < r < 4M_{\rm BH}$, since there is no matter, one can use Eqs. (2.93) and (2.94) to solve for the Zerilli master equation. The solution, which is ingoing at the horizon, is well-known in terms of Heun functions, using which we deduce the following boundary condition for the functions K, H_1, $\delta\rho$ and $D^{\rm up}$ at $4M_{\rm BH}$: $K(4M_{\rm BH})$ and $H_1(4M_{\rm BH})$ are deduced from the Zerilli ingoing function, while $\delta\rho(4M_{\rm BH}) = 0$ and $D^{\rm up}(4M_{\rm BH}) = 0$. We then use these boundary conditions to evolve the system of four ordinary first order differential equations up to a radial cutoff $r_{\rm C}$. At large radius, we can assume that the matter content is negligible and use the known 'up' solution of the Zerilli equation with outgoing boundary conditions at infinity. We deduce from Eqs. (2.93) and (2.94) the resulting boundary conditions for $K(r_{\rm C})$ and $H_1(r_{\rm C})$. In order to have a well-posed system we keep the boundary conditions $D^{\rm up}(r_{\rm C})$ and $\delta\rho(r_{\rm C})$ as free parameters. We then evolve the system inwards using the four ordinary first order differential equations. We perform a shooting method, where we equate the solutions at an intermediate radius between $4M_{\rm BH}$ and $r_{\rm C}$, fixing the real and imaginary parts of the frequency as well as the boundary conditions $D^{\rm up}(r_{\rm C})$ and $\delta\rho(r_{\rm C})$. There is a discrete set of solutions which are the frequencies of the QNMs.

2.5 Tidal Love numbers of a black hole in a dark matter halo

In this section, we consider the BH-spike system as a self-gravitating object subject to an external tidal field. We study the tidal Love numbers (TLNs) of the original non-relativistic Hernquist profile and compare them with the relativistic Schwarzschild-Hernquist profile described earlier in this work. The tidal Love numbers quantify the response of an object when subject to the influence of an external gravitational field. We will assume such tidal field can be sourced by the gradient of the gravitational field of a secondary BH in the primary BH-DM halo system. The external tidal field can be expanded in polar and axial multiple moments, with amplitudes $\mathcal{E}^{\ell m}$ and $\mathcal{B}^{\ell m}$ when projected on a spherical harmonics basis $Y^{\ell m}(\theta,\phi)$ [50]. As a result of this interaction with a weak tidal field, the mass and current multipole moments of the system (M_ℓ, S_ℓ) change proportionally to the external field. The system's multipole moments can be obtained from the asymptotic expansion of the metric functions, via

$$g_{tt} = -1 + \frac{2M}{r} + \sum_{\ell\geq 2}\left(\frac{2}{r^{\ell+1}}\left[\sqrt{\frac{4\pi}{2\ell+1}}M_\ell\, Y^{\ell 0} + (\ell' < \ell\,\text{pole})\right]\right.$$
$$\left. - \frac{2}{\ell\,(\ell-1)}r^\ell\left[\mathcal{E}_\ell Y^{\ell 0} + (\ell' < \ell\,\text{pole})\right]\right), \tag{2.113}$$

$$g_{t\varphi} = \frac{2J}{r}\sin^2\theta + \sum_{\ell\geq 2}\left(\frac{2}{r^\ell}\left[\sqrt{\frac{4\pi}{2\ell+1}}\frac{S_\ell}{\ell}\,S_\varphi^{\ell 0} + (\ell' < \ell\,\text{pole})\right]\right.$$
$$\left. + \frac{2r^{\ell+1}}{3\ell\,(\ell-1)}\left[\mathcal{B}_\ell S_\varphi^{\ell 0} + (\ell' < \ell\,\text{pole})\right]\right), \tag{2.114}$$

with $S^{\ell m} = \sin(\theta)Y^{\ell m}_{,\theta}$. We can then define the electric (even) and magnetic (odd) tidal Love numbers as [131, 71, 69],

$$k_\ell^E = -\frac{1}{2}\frac{\ell\,(\ell-1)}{R^{2\ell+1}}\sqrt{\frac{4\pi}{2\ell+1}}\frac{M_\ell}{\mathcal{E}_\ell}\,, \tag{2.115}$$

$$k_\ell^B = -\frac{3}{2}\frac{\ell\,(\ell-1)}{(\ell+1)\,R^{2\ell+1}}\sqrt{\frac{4\pi}{2\ell+1}}\frac{S_\ell}{\mathcal{B}_\ell}\,, \tag{2.116}$$

with R a characteristic scale of the system.

TLNs have been computed for compact astrophysical objects like neutron stars [131] as well as for exotic objects like BH mimickers, boson stars [71],

superradiant DM clouds [33, 70]. TLNs identically vanish for Schwarzschild BHs and for static perturbations of Kerr BHs [81, 150, 80]. Observing a non-zero tidal deformability of a BH would then be a odds with four-dimensional GR and would be a smoking-gun signature of new physics or of the presence of a consistent environment [192].

We compute the TLNs of the Schwarzschild-Hernquist system for both the axial as well as the polar sector of gravitational perturbations. In the axial sector, there are two different equations obtained from the 'up' and the 'down' choices of perturbations mentioned earlier, and we discuss how the TLNs differ for both of these cases. Moreover, for the non-relativistic profile, the TLNs can be determined analytically up to linear order in the ratio of DM mass and halo radius, while for the relativistic profile we will use a robust numerical method for determining the TLNs. We start with the axial sector.

2.5.1 Odd sector

Our starting point is the static limit $\omega = 0$ of the linearized perturbations of Einstein's equations. As discussed in 2.3.2, we found that there are two natural definitions for the matter sector perturbations: either one can fix $\delta(v^\mu) = 0$, which we refer to as the 'up' definition, or, one can fix $\delta(v_\mu) = 0$ which we refer to as the 'down' definition. In the static limit, the metric perturbation h_1 vanishes, thanks to Eq. (2.44). The Regge-Wheeler function is rescaled by the frequency, in order to have a non-trivial static limit, and is related to h_0. The master equation for the axial variable h_0 (associated with the $\delta g_{t\phi}$ component) in the static limit is given by setting $\omega = 0$ in Eq. (2.47). We will discuss these two cases separately for both relativistic and non-relativistic DM profiles.

The 'up' axial TLNs for the non-relativistic Hernquist profile

Using the 'up' definition of the fluid perturbations, and in the static limit, we find the metric perturbation h_0 to satisfy Eq. (2.47). However, the rescaled Regge-Wheeler function, which is related to h_0, satisfies Eq. (2.45). Thus for consistency between these two equations, we must impose $U^{up} = 0$, which yields

$$g h_0'' - 4\pi r \left(\bar{p}_{\rm r} + \bar{\rho}\right) h_0' - \left[\frac{(\ell+2)(\ell-1)}{r^2} + \frac{2g}{r^2} + 8\pi\left(\bar{\rho} - \bar{p}_{\rm r} + 2\bar{p}_{\rm t}\right)\right] h_0 = 0\,. \tag{2.117}$$

Inserting the background fluid quantities, namely $(\bar{\rho}, \bar{p}_{\rm r}, \bar{p}_{\rm t})$, it becomes challenging to obtain an analytic solution for the metric element h_0 in full generality. We thus expand h_0 in terms of the small parameter $\epsilon \sim (M_{\rm DM}/r_s)$.

For a realistic astrophysical scenario, with values of various scales given by Eq. (2.14), the above introduced smallness parameter ϵ becomes,

$$\epsilon \equiv \frac{GM_{\rm DM}}{c^2 r_s} \sim 10^{-4} \ . \tag{2.118}$$

As evident, the above quantity is indeed a small number and hence we can expand the relevant expressions in powers of the smallness parameter ϵ. Following which, we may write $h_0 = h_0^{(0)} + \epsilon h_0^{(1)} + \mathcal{O}(\epsilon^2)$, where the zeroth order term satisfies the standard equation for a static axial perturbation around the Schwarzschild BH,

$$h_0^{(0)\prime\prime} - \left[\frac{\ell(\ell+1)r - 4M_{\rm BH}}{r^2(r-2M_{\rm BH})}\right] h_0^{(0)} = 0 \ . \tag{2.119}$$

Note that we have at hand an (even smaller) second small parameter

$$\eta \equiv \frac{GM_{\rm BH}}{c^2 r_s} \sim 10^{-12} \ . \tag{2.120}$$

Focusing on the $\ell = 2$ case, the solution to the above zeroth order equation takes the following form,

$$\begin{aligned} h_0^{(0)} &= C_1 r^2 (r - 2M_{\rm BH}) \\ &+ C_2 \Big[\frac{2M_{\rm BH}^3 + 2M_{\rm BH}^2 r + 3M_{\rm BH} r^2 - 3r^3}{12 M_{\rm BH}^4 r} - \frac{r^2(r-2M_{\rm BH})}{8M_{\rm BH}^5} \ln\left(1 - \frac{2M_{\rm BH}}{r}\right) \Big] \ . \end{aligned} \tag{2.121}$$

In order to have regularity of $h_0^{(0)}$ and its derivatives at the horizon, we must set $C_2 = 0$. Hence, we obtain, the following solution for the zeroth order metric perturbation in the axial sector: $h_0^{(0)} = C_1 r^2 (r - 2M_{\rm BH})$. As a consequence the $\ell = 2$ magnetic TLN of Schwarzschild BH vanishes, because there is no decaying mode in the solution for the response to the tidal perturbation. This is consistent with earlier findings in the literature.

Let us now turn our attention to the first order perturbation of the $\ell = 2$ axial TLN due to the presence of DM halo. In the case of the non-relativistic Hernquist profile, we obtain the following equation for the metric perturbation, which is first order in the smallness parameter ϵ,

$$\begin{aligned} h_0^{(1)\prime\prime} - \left[\frac{\ell(\ell+1)r - 4M_{\rm BH}}{r^2(r-2M_{\rm BH})}\right] h_0^{(1)} &= \left[\frac{2r_s(r_s + 2M_{\rm BH})}{(r+r_s)^3}\right] h_0^{(0)\prime} \\ &+ \left[\frac{2r_s(\ell-1)(\ell+2)}{r(r+r_s)^2} + \frac{4r_s(r_s+2M_{\rm BH})(r-M_{\rm BH})}{r(r+r_s)^3(r-2M_{\rm BH})}\right] h_0^{(0)} \ . \end{aligned} \tag{2.122}$$

Therefore, the zeroth order term acts as a source for the differential equation satisfied by the first order term. In the case of $\ell = 2$, substituting $h_0^{(0)} = C_1 r^2(r - 2M_{\rm BH})$, the above differential equation for the first order perturbation $h_0^{(1)}$ becomes

$$h_0^{(1)\prime\prime} - \left[\frac{6r - 4M_{\rm BH}}{r^2(r - 2M_{\rm BH})}\right] h_0^{(1)} = C_1 \frac{2r_s r}{(r + r_s)^3}[4r^2 + r\,(9r_s + 2M_{\rm BH}) - 2M_{\rm BH}(7r_s + 6M_{\rm BH})]\,. \tag{2.123}$$

The above differential equation can be solved and the function $h_0^{(1)}$ admits a lengthy analytical solution with two arbitrary constants. The solution involves a homogeneous part, which resembles Eq.(2.121), with two arbitrary constants, D_1 describing the growing mode and D_2 describing the decaying mode, along with a particular solution dependent on C_1. Imposing regularity at the horizon and discarding the redundant growing mode of the homogeneous solution (setting $D_1 = 0$), we obtain a unique solution for D_2, proportional to C_1. The $\ell = 2$ magnetic TLN is extracted from the ratio of the coefficients of the $\mathcal{O}(r^{-2})$ and $\mathcal{O}(r^3)$ terms in the asymptotic expansion of h_0, times a suitable numerical coefficient. For $\ell = 2$, this overall numerical factor turns out to be $-(1/3)$. At leading order in ϵ, we take C_1 as the leading order r^3 term of $h_0^{(0)}$ while we extract the r^{-2} term from $h_0^{(1)}$. Instead of providing the full answer, we will now keep only the leading result in the expansion in the small number ϵ, yielding

$$k_{\ell=2}^{\rm B(up)} = \frac{M_{\rm DM} r_s^4\,[5 + 12\log(r_s/R)]}{3R^5}\,, \tag{2.124}$$

where, we have introduced an effective radial scale R, in order to make the argument of the logarithmic term dimensionless.

The characteristic length scale R, introduced above, can be defined in several ways. If we choose $R = (M_{\rm DM} + M_{\rm BH})$, then the above result will coincide with the axial TLN derived in [67]. However, this choice is inconsistent with the perturbation scheme. Indeed, one would then have $k_{\ell=2}^{\rm B(up)} = O(\epsilon^{-4})$ instead of $k_{\ell=2}^{\rm B(up)} = O(\epsilon^1)$. If we set $R = M_{BH}$ then the TLN would be $O(\epsilon\eta^{-5})$ which is inconsistent with the perturbative scheme. Consistently with the perturbative scheme, we normalize the TLN with respect to r_s. The TLN becomes $k_{\ell=2}^{\rm B(up)} = \frac{5}{3}\epsilon$, which scales correctly in ϵ, and differs from [69, 67].

The 'down' axial TLNs: Non-relativistic Hernquist profile

Alike the previous section, determining the 'up' axial TLNs, here also, consistency between Eq. (2.49) and Eq. (2.47) requires imposing $\delta(u_\mu) = 0$, which yields the following constraint

$$U^{\rm up} = -\frac{4\pi(\bar{\rho}+\bar{p}_{\rm t})}{f} h_0 \ . \tag{2.125}$$

Thus, in the 'down' definition for the fluid perturbations, the perturbation equation for h_0, in the static limit, reduces to

$$g h_0'' - 4\pi r\,(\bar{p}_{\rm r}+\bar{\rho})\,h_0' - \left[\frac{(\ell+2)(\ell-1)}{r^2} + \frac{2g}{r^2} - 8\pi\,(\bar{\rho}+\bar{p}_{\rm r})\right] h_0 = 0\,. \tag{2.126}$$

Following the discussion in the 'up' case, here also we insert the background fluid quantities, e.g., $g(r)$, $\bar{\rho}$, $\bar{p}$ in the above equation and then expand h_0 to first order in ϵ. This yields two differential equations, one for the zeroth piece $h_0^{(0)}$ and the other one for the first-order piece $h_0^{(1)}$. The differential equation satisfied by $h_0^{(0)}$ is identical to Eq. (2.121), while, the first-order perturbation $h_0^{(1)}$ satisfies a modified equation:

$$h_0^{(1)\prime\prime} - \left[\frac{\ell(\ell+1)r - 4M_{\rm BH}}{r^2(r-2M_{\rm BH})}\right] h_0^{(1)} = \left[\frac{2r_s(r_s+2M_{\rm BH})}{(r+r_s)^3}\right] h_0^{(0)\prime}$$
$$+ \left[\frac{2r_s\left\{(\ell-1)(\ell+2)(r+r_s) - 2(r_s+2M_{\rm BH})\right\}}{r(r+r_s)^3}\right] h_0^{(0)} \ . \tag{2.127}$$

Using the fact that the solution for $h_0^{(0)}$, which is regular at $r = 2M_{\rm BH}$, reads $h_0^{(0)} = C_1 r^2(r-2M_{\rm BH})$, along with setting $\ell = 2$, the above differential equation for $h_0^{(1)}$ reduces to,

$$h_0^{(1)\prime\prime} - \left[\frac{6r - 4M_{\rm BH}}{r^2(r-2M_{\rm BH})}\right] h_0^{(1)} = C_1 \frac{2r_s r}{(r+r_s)^3}\left[4r^2 + r\,(5r_s - 6M_{\rm BH}) - 8r_s M_{\rm BH}\right] \ . \tag{2.128}$$

Repeating the same analysis as in the 'up' case, elaborated in 2.5.1, we obtain the axial TLN for the $\ell = 2$ mode, associated with the down sector to read

$$k_{\ell=2}^{\rm B(down)} = \frac{M_{\rm DM} r_s^4\,[1 - 4\log(r_s/R)]}{3R^5} \ . \tag{2.129}$$

Here also R is characteristic length scale of the system, which we choose to be r_s, consistently with the perturbative scheme which requires that the TLN

scales as ϵ. The fractional change in the $\ell = 2$ axial TLN between the 'up' and the 'down' definition of perturbations is given by,

$$\Delta k^{\rm B}_{\ell=2} \equiv \frac{k^{\rm B(up)}_{\ell=2} - k^{\rm B(down)}_{\ell=2}}{k^{\rm B(up)}_{\ell=2}} = \frac{4}{5} \,, \tag{2.130}$$

which is a $\mathcal{O}(1)$ quantity. Therefore, the difference between the axial TLNs for the 'up' and the 'down' definition of perturbations is significant.

The 'up' axial TLNs for the Schwarzschild-Hernquist profile

The static axial perturbations, described by h_0, are again given by Eq. (2.117), irrespective of the DM profile under consideration. In the case of a relativistic Schwarzschild-Hernquist profile, it is challenging to obtain analytical solutions for the metric element h_0, even at linear order in the smallness parameter ϵ, due to complicated nature of the density profile and mass function. Since our interest for the determination of the TLNs is in the intermediate regime, we will consider the tidal effects up to a scale $r \ll r'_s \sim 10^{16} M_{\rm BH}$ for the range of parameters considered in Eq. (2.14). The DM density profile then reads:

$$\bar{\rho} = \lambda\, A \left(1 - \frac{4M_{\rm BH}}{r}\right)^{w} \left(\frac{M_{\rm BH}}{r}\right)^{q} , \tag{2.131}$$

where, estimations for λ, w and q have been given in 2.2.2. Integration of the above density profile will yield the mass function $m(r)$, which will be given by a hypergeometric function.

Since the relativistic dimensionless parameter

$$\epsilon_R \equiv \lambda A M_{BH}^2 \sim 5 \times 10^{-8} \lambda \tag{2.132}$$

sets the global scale of the DM density profile, we shall expand the expressions to order $\mathcal{O}(\epsilon_R)$, neglecting terms of $\mathcal{O}(\epsilon_R^2)$. Thus, we can expand the axial metric perturbation as, $h_0 = h_0^{(0)} + \epsilon_R h_1^{(0)} + \mathcal{O}(\epsilon_R^2)$ and expand Eq. (2.117) to the relevant order. For the $\ell = 2$ mode, the zeroth order perturbation $h_0^{(0)}$ satisfies again Eq. (2.119), which has the following regular solution: $h_0^{(0)} = C_1 r^2 (r - 2M_{\rm BH})$. Substituting back this solution for the zeroth order term, along with the density profile and the mass function, the differential equation for $h_0^{(1)}$ can be obtained. Due to its long and complicated expression, we have not quoted it here.

Given this differential equation, we have solved it numerically with the following boundary conditions: $h_0^{(1)}(4M_{\rm BH}) = 0$ and $\partial_r h_0^{(1)}(4M_{\rm BH}) = 0$. Both of which

stem from the results that the DM profile ends at $r = 4M_{\rm BH}$, and hence at $r = 4M_{\rm BH}$, the perturbations must coincide with the Schwarzschild counterpart. Similarly, one can also solve the differential equation in the intermediate zone through an asymptotic series, which involves C_1, as well as two additional constants D_1 and D_2. Subsequent matching of this asymptotic solution with the near-zone fixes the two constants D_1 and D_2 in terms of C_1, and hence one obtains the TLN associated with the $\ell = 2$ mode as,

$$k_{\ell=2}^{\rm B(up)} \simeq -279.86\, \frac{M_{\rm BH}^5}{R^5} \epsilon_R \ . \tag{2.133}$$

Consistently with the perturbation scheme, we set $R = M_{\rm BH}$ as standard for the computation of the TLN of a black hole, so that the TLN is linear in ϵ_R. We have also verified that the above numerical result for the TLN is stable with respect to change in the matching radius, which validates our numerical scheme.

The above TLN associated with the relativistic profile is also of the same order as that of the non-relativistic profile, albeit with an overall negative sign.

The 'down' axial TLNs for the Schwarzschild-Hernquist profile

The same expansion can be used to solve Eq. (2.126), stemming from the 'down' perturbation definition. Here also the zeroth order term satisfies the axial perturbation equation for the Schwarzschild spacetime, while the first order term satisfies a complicated equation. One can solve this equation in the near zone with identical boundary conditions, $h_0^{(1)}(4M_{\rm BH}) = 0$ and $\partial_r h_0^{(1)}(4M_{\rm BH}) = 0$, and also solve the equation in the far zone. Matching of the solution and its derivative between the near and the far zone uniquely fixes the arbitrary constants and, after fixing $R = M_{\rm BH}$ as above, yields the following TLN for the axial $\ell = 2$ mode,

$$k_{\ell=2}^{\rm B(down)} \simeq -102.1 \epsilon_R \, . \tag{2.134}$$

Alike the case of 'up' perturbation, for the 'down' perturbation as well the TLN is negative, and similar to the non-relativistic profile, for the relativistic case as well the relative difference in the TLN between the 'up' and 'down' perturbation schemes is of $\mathcal{O}(1)$, in particular,

$$\Delta k_{\ell=2}^{\rm B} \equiv \frac{k_{\ell=2}^{\rm B(up)} - k_{\ell=2}^{\rm B(down)}}{k_{\ell=2}^{\rm B(up)}} \approx 0.63 \, . \tag{2.135}$$

Thus the relative difference of the TLNs between these two definitions is of order unity, though individually the corresponding TLNs are small. This finishes our

discussion involving TLNs of BHs immersed in both non-relativistic as well as relativistic DM profiles in the axial sector. We now turn our attention to the TLNs in the polar sector.

2.5.2 Even sector

Having discussed the axial TLNs of BHs with a DM halo, associated with the $\ell = 2$ mode, in the previous section, here we present the corresponding results for the even sector. The starting point, once again, is the $\omega \to 0$ limit of the perturbation equations for the polar sector. As discussed in 2.3.3, in this limit, one can obtain a single second-order ordinary differential equation for the metric perturbation $H(r)$, which we have presented in Eq. (2.108). As already emphasized, in the polar sector, there are no distinctions between the 'up' and the 'down' components. Thus we start by solving the corresponding equation for non-relativistic Hernquist DM profile and hence determining the TLNs.

Polar TLNs: Non-relativistic Hernquist profile

Alike the axial sector, Eq. (2.108) does not admit an explicit solution for the pressure and density associated with the non-relativistic Hernquist profile. Thus we proceed by expanding the metric perturbation H as $H = H^{(0)} + \epsilon H^{(1)} + \mathcal{O}(\epsilon^2)$, where $\epsilon = (M_{\rm DM}/r_s)$, and solve it order by order. First of all we note that for the non-relativistic Hernquist profile, Eq. (2.108) can be simplified to the following form,

$$H'' + \left[\frac{2\{r - m(r)\}}{r\{r - 2m(r)\}} + \frac{4\pi r^2 \bar{\rho}}{m(r)}\right] H' + \left[-\frac{\ell(\ell+1) r\{r - 2m(r)\} + 4m(r)^2}{r^2\{r - 2m(r)\}^2} + \frac{8\pi r \bar{\rho}\{r^2 - 2rm(r) + 2m(r)^2\}}{m(r)\{r - 2m(r)\}^2}\right] H = 0. \tag{2.136}$$

After substituting the background expressions for the mass function $m(r)$ and density $\bar{\rho}(r)$ and expanding in powers of ϵ, the zeroth and first order terms satisfy the following differential equations

$$H^{(0)\prime\prime} + \frac{2(r - M_{\rm BH})}{r(r - 2M_{\rm BH})} H^{(0)\prime} - \frac{4M_{\rm BH}^2 - 2\ell(\ell+1) r M_{\rm BH} + \ell(\ell+1) r^2}{r^2 (r - 2M_{\rm BH})^2} H^{(0)} = 0 \ , \tag{2.137}$$

$$H^{(1)\prime\prime} + \frac{2(r - M_{\rm BH})}{r(r - 2M_{\rm BH})} H^{(1)\prime} - \frac{4M_{\rm BH}^2 - 2\ell(\ell+1) r M_{\rm BH} + \ell(\ell+1) r^2}{r^2 (r - 2M_{\rm BH})^2} H^{(1)}$$

$$= \frac{2r_s\left[M_{\rm BH}(r_s+4M_{\rm BH})-r(r_s+3M_{\rm BH})\right]}{M_{\rm BH}(r_s+r)^3}H^{(0)\prime}$$
$$+\frac{2r_s\left[r_s\ell(\ell+1)M_{\rm BH}-2r_sr+M_{\rm BH}\left\{\left(\ell^2+\ell-4\right)r+4M_{\rm BH}\right\}\right]}{M_{\rm BH}r(r_s+r)^3}H^{(0)}\,. \tag{2.138}$$

Alike the axial TLNs, here also we focus on the $\ell=2$ mode. At the leading order in ϵ, the differential equation for $H^{(0)}$ can be solved analytically and the solution reads,

$$\begin{aligned}H^{(0)} =& C_1\frac{3r(r-2M_{\rm BH})}{M_{\rm BH}^2}\\ &+\frac{C_2}{M_{\rm BH}^2r(2M_{\rm BH}-r)}(M_{\rm BH}(r-M_{\rm BH})\left(2M_{\rm BH}^2+6M_{\rm BH}r-3r^2\right)\\ &+\frac{3}{2}r^2(r-2M_{\rm BH})^2\ln\left(1-\frac{2M_{\rm BH}}{r}\right))\,,\end{aligned} \tag{2.139}$$

where C_1 and C_2 are arbitrary constants of integration. The regularity of the solution at the horizon requires that we set C_2 to zero and hence the solution reduces to $H^{(0)}=C_1 3r(r-2M_{\rm BH})/M_{\rm BH}^2$. Substituting the above regular solution for $H^{(0)}$, the differential equation for $H^{(1)}$ reduces to,

$$\begin{aligned}&H^{(1)\prime\prime}+\frac{2(r-M_{\rm BH})}{r(r-2M_{\rm BH})}H^{(1)\prime}+\frac{2\left(2M_{\rm BH}^2-6M_{\rm BH}r+3r^2\right)}{r^2(r-2M_{\rm BH})^2}H^{(1)}\\ &=C_1\frac{12r_s\left[M_{\rm BH}^2(7r_s+8M_{\rm BH})+2r^2(r_s+M_{\rm BH})-7M_{\rm BH}r(r_s+M_{\rm BH})\right]}{M_{\rm BH}^3(r_s+r)^3}\,.\end{aligned} \tag{2.140}$$

It follows from the above equation that $H^{(1)}$ admits an analytic solution, which we have not presented here due to its complicated nature. The solution has two constants D_1, associated with growing mode, and D_2, associated with decaying mode, coming from the homogeneous solution, and it also involves C_1 arising from the inhomogeneous part. Since the leading order perturbation involves a growing mode, and we are interested in the first order correction to the TLN, it follows that it will be proportional to the ratio (D_2/C_1). This is because the TLN can be extracted from the coefficients of the $\mathcal{O}(r^2)$ and $\mathcal{O}(r^{-3})$ components, both of which are combinations of C_1 and D_2. This ratio can then be determined by imposing regularity at the horizon. With the appropriate numerical factors defined in [71], modulo the normalization with respect to the

characteristic length scale of the problem, we obtain,

$$k^{\rm E}_{l=2} = \frac{2M_{\rm DM} r_s^4 \left[1 + 6\log(r_s/R)\right]}{R^5} \,. \tag{2.141}$$

For the choice of the characteristic scale $R = r_s$, the TLN scales as $(M_{\rm DM}/r_s)$, and hence is a linear quantity in ϵ. This is consistent with our findings in the axial sector.

Polar TLNs: Relativistic Schwarzschild-Hernquist profile

Having described the TLN of a BH immersed in a non-relativistic Hernquist DM profile, we will now present the results for the relativistic Schwarzschild-Hernquist profile. As in the axial sector, here also the zeroth order perturbation $H^{(0)}$ satisfies the polar perturbation equation for the Schwarzschild spacetime, while the first order term satisfies a complicated equation. One can solve this equation in the near zone with the boundary conditions, $H^{(1)}(4M_{\rm BH}) = 0$ and $\partial_r H^{(1)}(4M_{\rm BH}) = 0$, and also solve the equation in the far zone in terms of an appropriate power series. Matching of the solution and its derivative between the near and the far zone uniquely fixes the arbitrary constants and, after setting $R = M_{\rm BH}$ yields the following TLN for the polar $\ell = 2$ mode,

$$k^{\rm E}_{\ell=2} = 645.9\epsilon_R \,. \tag{2.142}$$

Note that, even though the axial and the polar TLNs have the same scaling they have different signs and magnitude, while the axial TLNs are negative, the polar TLNs are positive. We checked the value of the TLN is stable upon changing the matching radius, which validates our numerical method.

2.6 Discussion

The geometry of a black hole immersed in a dark matter halo and its response as well as relaxation to external perturbation will help in deciphering the presence of a dark matter environment, as well as establishing the density profile of the dark matter distribution from the GW measurements. The key feature of the dark matter distribution is its anisotropic nature: the radial pressure is negligible (assuming the accretion rate to be small compared to any other time scale in the problem), while the tangential pressure is non-zero. Finding out such a geometry started from Ref. [67], even though the dark matter density profile considered there was non-relativistic. Since the dark matter particles probe the region close to the horizon, it is important to study the relativistic

generalization of the same, which was achieved in [210]. However, the fall-off behaviour for the dark matter density profile was inadequate, leading to serious issues, e.g., infinite energy. In this work, we have derived, starting from the non-relativistic Hernquist dark matter profile, the relativistic profile for the dark matter distribution, using the approach of Ref. [205], and have referred to it as the Schwarzschild-Hernquist profile. The relativistic dark matter density profile, so derived, vanishes at $r = 4M_{\rm BH}$, has a sharp spike located at $r \approx 6M_{\rm BH}$, and has the appropriate fall-off behaviour at large distances. It is worth pointing out that the peak of the relativistic dark matter spike is several orders of magnitude higher compared to the non-relativistic scenario. All of these features agree with the work [211], which was derived independently, and which nearly numerically agrees with our model.

Our construction of the relativistic dark matter profile brings an intriguing result involving the existence of multiple light rings. As is well known, existence of multiple light rings require the existence of stable and trapped photon orbits, which will eventually lead to instabilities of linear perturbations. Following the recent construction of geometries, which are solutions to the Einstein's equations with matter fields violating energy conditions, and having multiple light rings [123], we have also investigated the existence of such solutions within our phase space supported by an anisotropic dark matter distribution. We found that, indeed, there exist matter configurations that obey the dominant energy condition, while they admit multiple light rings, or, more precisely, light rings and anti-light rings in the sense of [91]. Such matter configurations span a small region of parameter space, which we consider unphysical due to the very high matter densities involved, but we cannot rule them out just from known energy conditions. This suggests that realistic matter configurations do not have multiple light rings, but also that new energy conditions might exist that rule out such configurations, in line with independent work [30, 168] .

Besides pointing out various properties of the relativistic dark matter distribution, we have provided the complete formulation of linear perturbations of the coupled system of a dark matter profile supported by anisotropic matter and a central black hole, for both the axial and the polar sector. In comparison with the existing literature, we have considered an arbitrary radial pressure, which is independent from the pressure on the tangential directions. We wrote our final set of equations in readable and reproducible format on a Github repository. During our analysis, we have invalidated the claim of [159] that a gauge-invariant third order master Zerilli-type equation exists for such perturbations. We also noted some differences with the earlier written equations in the literature [67]: within the axial sector we have obtained two different equations, both in the dynamic as well as in the static situation, depending on whether we set the perturbation of contravariant or, covariant components of

the fluid four-velocity to zero. Physically, these conditions correspond to distinct assumptions on the nature of the fluid perturbations. We have cross-checked our equations with two independent Mathematica codes, one based on the xAct package and another one based on the RGtensor package. We furthermore cross-checked the compatibility of the matter and the Einstein's equations. In addition, we have also discussed the static limit and the equations important for assessing the tidal Love numbers of the coupled BH-dark matter system. Thus our results have a much broader applicability: they hold for linear perturbation analysis of any anisotropic system, including anisotropic neutron stars [181].

In the dynamical sector, we have solved the master Regge-Wheeler-like equation for axial perturbations, with ingoing boundary condition at the horizon and outgoing boundary condition asymptotically. Our results demonstrate a key difference between the non-relativistic and relativistic dark matter distribution: for the non-relativistic case, the fractional change in the quasi-normal mode frequencies, as compared to the Schwarzschild black hole, scales linearly with $(M_{\rm DM}/r_{\rm s})$; while for the relativistic profile, the fractional change in the quasi-normal mode frequencies scale as $(M_{\rm DM}/r_{\rm s})^{3/2}$, with a mass dependent pre-factor. We therefore found a striking signature for a relativistic dark matter profile. Since our result is based on the Hernquist distribution, it would be interesting in the future to investigate how general are these scaling laws for more generic matter profiles. Moreover, there are indeed differences between the quasi-normal mode frequencies computed using either choice of matter perturbations (setting either the covariant or contravariant components of the perturbation of the fluid velocity to zero), but the difference is much smaller as compared to the quasi-normal mode frequencies themselves. The fractional change in the quasi-normal mode frequencies, as reported in this work have been numerically computed for dark matter profiles with unrealistic values, e.g., $M_{\rm DM}/M_{\rm BH} = 100$, for numerical stability reasons. For astrophysical scenarios with $M_{\rm DM}/M_{\rm BH} = \mathcal{O}(10^6)$, the fractional changes in the quasi-normal mode frequencies will be $\mathcal{O}(10^{-4})$, making it very difficult to distinguish between the Schwarzschild and the Schwarzschild-Hernquist black hole.

Besides the quasi-normal mode frequencies, we have also derived both the axial and the polar tidal Love numbers for a black hole immersed in a relativistic as well as non-relativistic dark matter halo for realistic values of the dark matter profile. Our results agree with those in Ref. [67], for the non-relativistic Hernquist dark matter profile, except for the choice of the characteristic radius. Ref. [67] takes this characteristic radius to be related to the mass of the dark matter halo, leading to a Love number which scales according to the ratio of dark matter total mass and breaking radius of the halo inconsistently with the perturbative approach considered. Instead, we have chosen this characteristic radius to be the breaking radius of the dark matter halo, leading to a tidal Love

number which scales consistently with the perturbative scheme. Our results suggest that for realistic dark matter distribution, the tidal Love number for a non-relativistic distribution is $\mathcal{O}(10^{-4})$ while it suppressed to $\mathcal{O}(10^{-5})$ for a relativistic distribution with a central black hole of a million solar masses. Hence it is challenging to see the effect of the dark matter halo through the tidal Love number measurements, alike the situation for the quasi-normal modes. In addition, we have shown that the relative difference between the choice of matter perturbations lead to leading order $\mathcal{O}(1)$ changes of the tidal Love numbers. It is therefore crucial to model the fluid perturbations in detail in order to obtain meaningful predictions for the tidal Love numbers.

In the process we have developed our own numerical methods to compute the tidal Love numbers for a black hole within the relativistic halo, with the result being highly numerically stable. In this numerical approach, we formulate an asymptotic analytic expansion of the perturbation variable at large radius, and at the same time solve for the relevant differential equation at arbitrary precision to low radius, so that we obtain the solution at small radius to high numerical precision. The tidal Love numbers are then obtained by matching the asymptotic solution with the near-zone solution at an intermediate radius. The resulting tidal Love numbers are found to be independent of the matching radius, as long as it belongs to a suitable range dictated by controlled numerical errors. This provides a robust scheme for deriving the tidal Love numbers for physically realistic values of the dark matter distribution.

All in all, our results conclusively suggests that for realistic values of the dark matter distribution, both the quasi-normal modes, as well as the tidal Love numbers are modified by terms $\mathcal{O}(10^{-4})$ or lower. This suggests that the tidal Love numbers and the quasi-normal modes may not be able to provide a smoking gun signature for the existence of dark matter environments using the currently planned detectors. Rather the dynamical friction arising out of an extreme-mass-ratio inspiral within the dark matter environment can lead to significant dephasing of the GW signal and appears to be the proper avenue for exploring properties of dark matter environments [210, 211, 82, 179, 215].

2.7 Data availability

We provide three Mathematica notebooks in the Github repository 10.5281/zenodo.15772894. The first notebook summarizes the equations of even parity perturbations around a spherically symmetric background sourced by an anisotropic fluid and their properties. The second notebook provides the computation of tidal Love numbers and our stable numerical scheme. The third

notebook details the Schwarzschild-Hernquist black hole and provides a solution obeying the dominant energy condition which admits two light rings and one anti-light ring.

Chapter 3

Boson stars solutions from nonlinear sigma models

3.1 Introduction

The study of gravitating particle-like objects — self-gravitating solutions without a horizon or a singularity — forms an important chapter in the history of general relativity, dating back to Wheeler's geons [223, 193]. Today, at the dawn of the era of gravitational wave astronomy [5], the interest in this type of objects has spiked. Indeed, among the many possibilities these experiments offer us is the search for (horizonless) exotic compact objects, alternative to black holes, which would produce characteristic gravitational wave signatures [75, 74]. Many candidates for exotic compact objects have been proposed in the literature, *e.g.* [182, 171, 169, 92, 134, 62, 170], but among them, boson stars [139, 158, 220] stand out as the best motivated ones, as they have a robust dynamical foundation [152, 118, 149] and they could be part of the dark matter content of the universe [139, 207, 162].

Boson stars are self-gravitating condensates of massive bosons prevented from collapsing by the Heisenberg uncertainty principle. These objects arise as solutions of general relativity coupled to massive bosonic fields (either scalar or Proca fields) with a continuous symmetry. The existence of this symmetry allows these fields to generate a stationary stress-energy tensor and a conserved charge by rotating in field space.

The simplest theory leading to boson stars corresponds to a complex scalar field Φ invariant under phase shifts $\Phi \to e^{i\alpha}\Phi$, with a Lagrangian of the form

$$\mathcal{L}_\Phi = -\frac{1}{2}\partial_\mu \Phi \partial^\mu \bar{\Phi} - V\left(|\Phi|^2\right) . \tag{3.1}$$

This kind of models, with a variety of potentials $V\left(|\Phi|^2\right)$, have been extensively studied in the literature. The properties of boson stars change widely depending on the potential, and some of the most studied models are mini boson stars [143, 204] — with a non-interactive potential — massive boson stars [85] — including a quartic self-interaction [145]— solitonic boson stars [151, 115, 153] — which unlike the others, persist in flat spacetime — or axion boson stars [121, 94] — with a periodic potential inspired by QCD. Other related solutions are the recently proposed ℓ-boson stars that arise in a system with N complex Klein-Gordon fields [8, 9, 137, 7]. It would be impossible to list here all the existing boson star models, so we refer to [158, 176, 220] and the references therein for a comprehensive review.

Despite this zoo of models, one can make the case that there are interesting and natural extensions of this family of theories yet to be explored. In fact, instead of just changing the potential, one could more generally promote (4.30) to a nonlinear sigma model

$$\mathcal{L}_\phi = -\frac{1}{2}G_{AB}(\phi)\partial_\mu \phi^A \partial^\mu \phi^B - V\left(\phi^A\right) . \tag{3.2}$$

Here, the scalars ϕ^A (with $A = 1, \ldots, N$) can be regarded as coordinates in a target space: the scalar manifold. The kinetic matrix $G_{AB}(\phi)$ is the metric in this manifold, which in general can be curved. These models, too, can exhibit continuous symmetries required for the construction of boson stars. This happens whenever the scalar manifold possesses an isometry. In fact, this kind of models are commonplace in supergravity and compactified string theory effective actions, where the scalar manifold is very often a symmetric space [186]. Also in those theories, a potential $V(\phi^A)$ generally arises when the symmetries are gauged. Thus, this is a very natural extension of (3.1) motivated by high-energy physics. This is even more significative taking into account that the scalar field can typically reach Planckian values in a boson star [133], and hence one would be probing the theory all the way up to Planck scale, where these nonlinearities become relevant.

The goal of this chapter is to show the existence and study the properties of boson stars in some of these nonlinear sigma models inspired by string theory. Besides their connection with fundamental physics, these models are also interesting from a phenomenological point of view, as they can be regarded as nonlinear completions of the standard model (3.1). While for small field

values the nonlinear models will reduce to (3.1), significant differences may arise for the most massive and compact boson stars, where the nonlinear effects kick in. Thus, they provide an interesting variation in the zoo of boson star solutions.

Quite surprisingly, these models have barely been studied in the boson star literature, and the few existing analyses [218, 128] — both focusing on O(3) models — have not yet provided a thorough exploration of the space of theories and solutions. Here we provide a detailed analysis of the effect of the curvature of the nonlinear sigma model on boson stars and show that it dramatically affects their masses and compactnesses. Thus, the sigma model metric is as relevant (or more) as the potential in determining the properties of boson stars.

The chapter is organized as follows. In section 3.2 we review the nonlinear sigma models that will be the focus of our study. In section 3.3 we couple these models to gravity and study their spherically symmetric boson star solutions. We analyze some of their properties focusing on the dependence of their mass and compactness on the curvature of the sigma model. We discuss the relation between the energy scale of the nonlinear sigma model and the mass of boson stars in 3.4. Finally, we conclude in 3.5 by discussing our results as well as future directions.

3.2 Nonlinear sigma models

In this section we study the two-dimensional nonlinear sigma models (*i.e.*, with two scalars) that are of potential interest for the construction of boson stars. We start discussing a particularly interesting model before presenting the general case.

3.2.1 Axion-dilaton model

The axion-dilaton system[1] is ubiquitous in the context of supergravity and string theory [186]. The kinetic term of this model takes the form

$$\mathcal{L}_K = -\frac{1}{2}(\partial\phi)^2 - \frac{1}{2}e^{2\gamma\phi}(\partial a)^2\,, \tag{3.3}$$

[1] One should not confuse the (stringy) axion-dilaton model with the (QCD) axion model of [121] — these are totally unrelated theories. We also remark that, although the axion-dilaton system has sometimes been mentioned in the boson star literature [175], a proper analysis of its solutions, taking into account its nonlinear character, has not been carried out.

where ϕ is the dilaton, a is the axion and γ is a parameter that determines the strength of the coupling between both scalars. A very typical value in string theory scenarios is $\gamma = 1$ (in Planck units), but other values are possible.

The scalar manifold is the hyperbolic space and as such the kinetic term exhibits $\mathrm{SL}(2,\mathbb{R})$ symmetry. In order to make it manifest, it is convenient to work with the complex scalar field

$$\tau = \gamma a + i e^{-\gamma\phi}\,, \tag{3.4}$$

in terms of which the Lagrangian reads

$$\mathcal{L}_K = -\frac{\partial_\mu \tau \partial^\mu \bar{\tau}}{2\gamma^2 \mathrm{Im}(\tau)^2}\,. \tag{3.5}$$

Then, one can check that $\mathcal{L}_K$ is invariant under the $\mathrm{SL}(2,\mathbb{R})$ group in the form of Möbius transformations

$$\tau' = \frac{c_1\tau + c_2}{c_3\tau + c_4}\,, \qquad \text{where } \; c_1c_4 - c_2c_3 = 1\,, \tag{3.6}$$

with $c_i \in \mathbb{R}$.

To complete our model, we need to provide a mass term for the scalars. This must preserve some of the symmetries of the kinetic term if the theory is to possess boson star solutions. It is not possible to have a potential that preserves the whole $\mathrm{SL}(2,\mathbb{R})$ group, but however it is enough to focus on the $\mathrm{U}(1)$ subgroup given by the transformation

$$\tau' = \frac{\tau\cos(\alpha/2) + \sin(\alpha/2)}{\cos(\alpha/2) - \tau\sin(\alpha/2)}\,, \quad \alpha \in [0, 2\pi)\,. \tag{3.7}$$

Then, we look for a potential $U(\tau, \bar{\tau})$ that is invariant under such transformation. In particular, invariance of U under the infinitesimal transformation $\delta\tau = \frac{1}{2}(1+\tau^2)$ implies that

$$\delta U = \frac{1}{2}(1+\tau^2)\partial_\tau U + \frac{1}{2}(1+\bar{\tau}^2)\partial_{\bar{\tau}} U = 0 \tag{3.8}$$

Solving this equation we find the the potential must have the form $U = U(\mathcal{T}^2)$, where $\mathcal{T}^2$ is the basic invariant

$$\begin{aligned}\mathcal{T}^2 &= \frac{1}{\gamma^2}\left(\frac{1+|\tau|^2}{\mathrm{Im}(\tau)} - 2\right) \\ &= \frac{4}{\gamma^2}\sinh^2\left(\frac{\gamma\phi}{2}\right) + a^2 e^{\gamma\phi}\,.\end{aligned} \tag{3.9}$$

Summarizing, our theory with a massive axidilaton with U(1) symmetry is in general given by

$$\mathcal{L} = -\frac{\partial_\mu \tau \partial^\mu \bar{\tau}}{2\gamma^2 \mathrm{Im}(\tau)^2} - U\left(\mathcal{T}^2\right) , \tag{3.10}$$

and it only remains to choose a specific potential. A natural choice would be a polynomial in $\mathcal{T}^2$, the simplest choice being just $U(\mathcal{T}^2) = \frac{1}{2}\mu^2\mathcal{T}^2$, where μ is the mass of the field. As we explain below, this is the analogous of a non-interactive potential in the case of a curved sigma model — see Footnote 3.

3.2.2 Maximally symmetric models

The axion-dilaton model is a maximally symmetric sigma model in the sense that its target manifold — the hyperbolic space — is maximally symmetric.[2] We can also consider its positive-curvature version, the O(3) model, where the target manifold is the sphere. We can write the two theories in a unified form as follows. Starting from the axion-dilaton model (3.10) we perform the change of variables

$$\Phi = \frac{2}{\gamma}\frac{1+i\tau}{1-i\tau} , \tag{3.11}$$

in terms of which the Lagrangian reads

$$\mathcal{L} = -\frac{\partial_\mu \Phi \partial^\mu \bar{\Phi}}{2\left(1-\frac{\gamma^2}{4}|\Phi|^2\right)^2} - U\left(\frac{|\Phi|^2}{\left(1-\frac{\gamma^2}{4}|\Phi|^2\right)}\right) , \tag{3.12}$$

where we used that

$$\mathcal{T}^2 = \frac{|\Phi|^2}{\left(1-\frac{\gamma^2}{4}|\Phi|^2\right)} . \tag{3.13}$$

When expressed in this form we observe that the theory only depends on γ^2, allowing us to extend it to $\gamma^2 < 0$. In fact, while for $\gamma^2 > 0$ the scalar manifold is the hyperbolic space — hence the $\mathrm{SL}(2,\mathbb{R})$ symmetry — for $\gamma^2 < 0$ it corresponds to the 2-sphere, so we get an O(3) sigma model. For $\gamma = 0$ it reduces to the linear sigma model (3.1). Indeed, these are the three possible maximally symmetric sigma models, where γ^2 is nothing but (minus) the curvature of the scalar manifold.

[2] Of course, the potential always breaks this symmetry down to U(1).

3.2.3 General case

Another interesting aspect about (4.35) is that now the U(1) symmetry is manifest, as it acts on Φ in the usual way

$$\Phi \to e^{i\alpha}\Phi\,. \tag{3.14}$$

In fact, in Appendix B.1 we show that every two-dimensional nonlinear sigma model with a U(1) holomorphic isometry can be written in the "canonical" form

$$\mathcal{L}_{\Phi}^{\mathrm{U}(1)} = -K\left(|\Phi|^2\right)\partial_\mu\Phi\partial^\mu\bar{\Phi} - V\left(|\Phi|^2\right)\,, \tag{3.15}$$

with a certain kinetic function $K\left(|\Phi|^2\right)$ and potential $V\left(|\Phi|^2\right)$. The Lagrangian (3.12) is in this sense the canonical form of the maximally symmetric theories.

In closing this section, let us take note of the conserved current associated to the unbroken U(1) symmetry of these models,

$$J_\mu = iK\left(|\Phi|^2\right)\left(\bar{\Phi}\partial_\mu\Phi - \Phi\partial_\mu\bar{\Phi}\right)\,. \tag{3.16}$$

3.3 Boson stars

3.3.1 Theory

Let us now couple the general U(1) invariant model (3.15) to gravity,

$$S = \frac{1}{16\pi G}\int d^4x\sqrt{-g}\left[R + \mathcal{L}_{\Phi}^{\mathrm{U}(1)}\right]\,. \tag{3.17}$$

We remark that the scalar field is expressed in Planck units, hence the common factor of $(16\pi G)^{-1}$. We will come back to this when discussing the energy scale of the sigma model in Section 3.4.

The equations of motion of this theory read

$$G_{\mu\nu} = K\left(\partial_{(\mu}\Phi\partial_{\nu)}\bar{\Phi} - \frac{1}{2}g_{\mu\nu}\partial_\alpha\Phi\partial^\alpha\bar{\Phi}\right) - \frac{1}{2}Vg_{\mu\nu}\,, \tag{3.18}$$

$$0 = K\nabla^2\Phi + K'\bar{\Phi}\left(\partial\Phi\right)^2 - \Phi V'\,, \tag{3.19}$$

where $G_{\mu\nu}$ is the Einstein tensor and $K' = dK/d|\Phi|^2$, $V' = dV/d|\Phi|^2$. We focus here on the family of models (3.12), so we choose

$$K\left(|\Phi|^2\right) = \frac{1}{2\left(1 - \frac{\gamma^2}{4}|\Phi|^2\right)^2}\,. \tag{3.20}$$

In addition, we use the following potential

$$V\left(|\Phi|^2\right) = \frac{\mu^2|\Phi|^2}{2\left(1-\frac{\gamma^2}{4}|\Phi|^2\right)}\,, \tag{3.21}$$

where μ represents the mass of the bosons. This is analogous to a non-interactive mass term in the case of a curved sigma model,[3] while interaction terms would correspond to higher powers of the same combination. We do not include those since our goal is to study the effect of the curvature of the sigma model on boson stars, rather than the effect of the potential. Thus, we stick to the minimally interacting potential (3.21).

3.3.2 Boson star ansatz

We look for spherically symmetric solutions of the form

$$ds^2 = -f(r)dt^2 + \frac{dr^2}{g(r)} + r^2 d\Omega_{(2)}^2\,, \tag{3.22}$$

$$\Phi = \Phi_0(r)e^{-i\omega t}\,, \tag{3.23}$$

where $\Phi_0(r)$ is real. The harmonic time dependence of Φ ensures that the stress-energy tensor is stationary even if the scalar field is not. Now, instead of working with $\Phi_0(r)$, we find it interesting to work with the variable

$$\phi(r) = \begin{cases} \frac{2}{\gamma}\,\mathrm{argtanh}\left(\frac{\gamma\Phi_0(r)}{2}\right) & \text{if } \gamma^2 > 0 \\ \Phi_0(r) & \text{if } \gamma = 0 \\ \frac{2}{|\gamma|}\arctan\left(\frac{|\gamma|\Phi_0(r)}{2}\right) & \text{if } \gamma^2 < 0\,. \end{cases} \tag{3.24}$$

This can be identified with the original dilaton in (3.3) in the case of $\gamma^2 > 0$. With this, we find that the tt and rr components of Einstein equations (3.18) read

$$rg' + g - 1 = -2r^2\rho \tag{3.25}$$

$$g\left(\frac{rf'}{f} + 1\right) - 1 = 2r^2 p\,, \tag{3.26}$$

[3] This is the only potential for which plane waves $\Phi = Ae^{-ik_\mu x^\mu}$, with $k^2 = -\mu^2$, remain exact solutions. Hence this is the closest one can get to free fields in the case of a curved sigma model.

while the scalar equation (3.19) yields

$$\phi'' + \frac{1}{2}\phi'\left(\frac{f'}{f} + \frac{g'}{g} + \frac{4}{r}\right) + \frac{\omega^2}{fg}\mathcal{S}_{2\gamma}(\phi) = \frac{\mu^2}{g}\mathcal{S}_\gamma(\phi)\,. \tag{3.27}$$

Here the density $\rho = f^{-1}T_{tt}$ and radial pressure $p = gT_{rr}$ are given by

$$\rho = +\frac{\mu^2}{8}\mathcal{S}^2_{\gamma/2}(\phi) + \frac{g}{8}\phi'^2 + \frac{\omega^2}{8f}\mathcal{S}^2_\gamma(\phi)\,, \tag{3.28}$$

$$p = -\frac{\mu^2}{8}\mathcal{S}^2_{\gamma/2}(\phi) + \frac{g}{8}\phi'^2 + \frac{\omega^2}{8f}\mathcal{S}^2_\gamma(\phi)\,, \tag{3.29}$$

and we have introduced the notation

$$\mathcal{S}_\gamma(\phi) := \begin{cases} \frac{1}{\gamma}\sinh(\gamma\phi) & \text{if } \gamma^2 > 0 \\ \phi & \text{if } \gamma = 0 \\ \frac{1}{|\gamma|}\sin(|\gamma|\phi) & \text{if } \gamma^2 < 0\,. \end{cases} \tag{3.30}$$

We note that the appearance of the function $\mathcal{S}_\gamma(\phi)$ is the key effect of the nonlinear sigma models. We also remark that in the case $\gamma^2 < 0$ the variable $\phi(r)$ is compact, as it lies in the interval $-\pi|\gamma| < \phi < \pi|\gamma|$.

Boson stars are horizonless solutions that are regular at the origin. To ensure smoothness, we must impose $g(0) = 1$, and the Taylor expansion of the functions f, g and ϕ around $r = 0$ must only contain even powers of r,

$$\begin{aligned} f(r) &= f_0 + \sum_{n=1}^{\infty} f_{2n} r^{2n}\,, \\ g(r) &= 1 + \sum_{n=1}^{\infty} g_{2n} r^{2n}\,, \\ \phi(r) &= \phi_0 + \sum_{n=1}^{\infty} \phi_{2n} r^{2n}\,. \end{aligned} \tag{3.31}$$

The whole series is determined by f_0 (which must be taken positive) and the central value of the scalar field ϕ_0. For instance, the $\mathcal{O}(r^2)$ coefficients are given by

$$f_2 = \frac{1}{6}\omega^2\mathcal{S}^2_\gamma(\phi_0) - \frac{1}{12}f_0\mu^2\mathcal{S}^2_{\gamma/2}(\phi_0)\,, \tag{3.32}$$

$$g_2 = -\frac{\left(f_0\mu^2\mathcal{S}^2_{\gamma/2}(\phi_0) + \omega^2\mathcal{S}^2_\gamma(\phi_0)\right)}{12 f_0}\,, \tag{3.33}$$

$$\phi_2 = \frac{1}{6}\left(\mu^2 S_\gamma\left(\phi_0\right) - \frac{\omega^2 S_{2\gamma}\left(\phi_0\right)}{f_0}\right), \tag{3.34}$$

and one can similarly find the subsequent terms.

On the other hand, at infinity we require that the solution be asymptotically flat. This will happen if,

$$\begin{aligned} f(r\to\infty) = g(r\to\infty) = 1\,, \\ \phi(r\to\infty) = 0\,. \end{aligned} \tag{3.35}$$

The condition on f fixes the value of f_0, while the condition on g is automatically satisfied taking into account Eq. (3.25) and that $r^2\rho \to 0$ at infinity. On the other hand, ϕ has the familiar Yukawa-type behavior near infinity,

$$\phi(r) \sim \frac{\phi_+}{r} e^{r\sqrt{\mu^2-\omega^2}} + \frac{\phi_-}{r} e^{-r\sqrt{\mu^2-\omega^2}} \tag{3.36}$$

For $\omega^2 < \mu^2$ we have a exponentially growing mode and a exponentially decaying one, and hence asymptotic flatness is only achieved for $\phi_+ = 0$. However, for a given choice of ϕ_0 and ω the solution defined by the regularity conditions (3.31) typically contains both modes and hence is not asymptotically flat.[4] Thus, the asymptotic flatness condition provides an eigenvalue problem that only has solutions for discrete values of ω that depend on ϕ_0. These are the bound states representing boson stars. These solutions can be labeled by an integer n that characterizes the number of nodes of the scalar field. Numerical investigations of the nonlinear stability of boson stars have found that excited field stars are unstable against perturbations and will either decay to the ground state via gravitational cooling, collapse into a BH or radiate the field to infinity [26, 158]. Therefore, here we will focus on the ground state solution $n = 1$. Finally, for $\omega^2 > \mu^2$ the scalar field radiates and we do not have confined solutions.

3.3.3 Numerical strategy

In order to solve the differential equations (3.26), (3.25), (3.27) we can always work in natural units with $\mu = 1$ by performing $r \to r/\mu$, $\omega \to \omega\mu$. In addition, it is also interesting to set $f_0 = 1$, which is equivalent to performing the rescalings

$$t = \tilde{t}/\sqrt{f_0}\,, \quad f = f_0\tilde{f}\,, \quad \omega = \sqrt{f_0}\tilde{\omega}\,. \tag{3.37}$$

The value of f_0 can then be retrieved once a solution is found by using that $\lim_{r\to\infty}\tilde{f}(r) = 1/f_0$

[4] In practice, those solutions cannot be extended to infinity as they typically develop a singularity at some finite r.

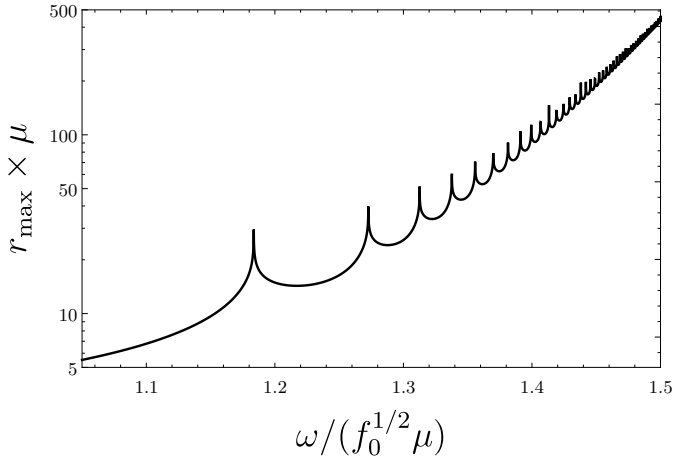

Figure 3.1: Radius of existence of the numerical solutions with $\phi_0 = 0.5$, $\gamma = 1$ as a function of ω. Boson stars are the solutions whose domain extends to infinity and they correspond to the peaks shown in this curve, with the ground-state boson star being the leftmost peak.

We solve (3.26), (3.25), (3.27) numerically using the expansion (3.31) at order r^4 to set our initial conditions near $r = 0$ (we used $r_{\text{in}} = 10^{-3}$).

Generically, for a given ω, the numerical solution breaks down at some finite $r = r_{\max}$ and hence it does not extend to infinity. This blowup of the numerical integration appears because the exponentially growing mode of the scalar field is being excited. However, when ω approaches some special values, the domain of validity grows indefinitely, pointing the existence of asymptotically flat solutions. We show this maximal radius in Figure 3.1 for $\gamma = 1$ and $\phi_0 = 1/2$. The peaks in the curve correspond to the boson star solutions, with the leftmost peak being the ground state $n = 1$. In order to find ω with higher accuracy, we then employed a bisection-type method that searches the position of these peaks. As we can observe, the peaks are extremely sharp, and in order to obtain accurate enough solutions one needs to find ω with many digits of precision. The problem becomes stiffer for larger values of $|\gamma|$ and ϕ_0 (corresponding to the most compact solutions), which makes obtaining those solutions particularly challenging. We provide additional details on our numerical approach in Appendix B.2.

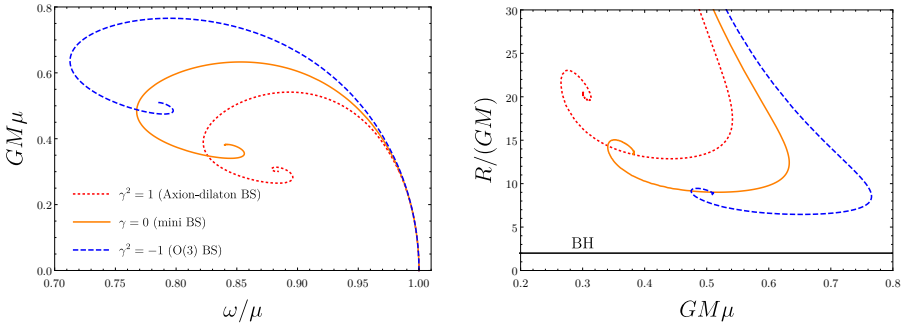

Figure 3.2: Left: existence curve (ω, M) for ground-state boson stars with different values of γ. Right: compactness $R/(GM)$ as a function of the mass for the same families of boson stars.

3.3.4 Mass, charge and radius

Once a numerical solution has been found, we can obtain some of its properties. Let us introduce the mass function $m(r)$ by

$$g(r) = 1 - \frac{2Gm(r)}{r}\,. \tag{3.38}$$

The total ADM mass of the solutions is given by the asymptotic value

$$M = \lim_{r\to\infty} m(r)\,. \tag{3.39}$$

On the other hand, boson stars do not have a sharp surface, but it is usual to define their radius R as the value of r that contains 99% of the mass. Thus, R is implicitly defined by

$$\frac{m(R)}{M} = 0.99\,. \tag{3.40}$$

We shall define the compactness as the ratio $R/(GM)$, which takes a minimum value of 2 for a Schwarzschild black hole.[5] Finally, the conserved U(1) charge reads

$$Q = \frac{\omega}{4G}\int_0^\infty dr \frac{r^2\mathcal{S}_\gamma^2(\phi)}{\sqrt{f(r)g(r)}} \tag{3.41}$$

[5]We take note of the confusion that a *greater* compactness means a *smaller* $R/(GM)$. Other authors refer to the inverse of this quantity as the compactness in order to avoid this issue. However, we prefer to report the values of $R/(GM)$ because it is a more intuitive number.

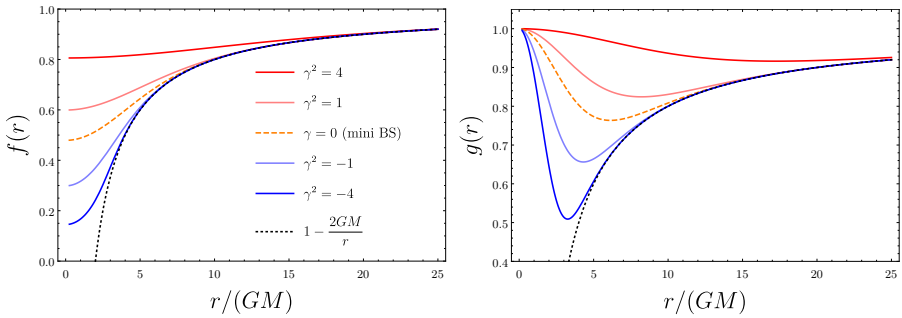

Figure 3.3: Metric functions $f(r)$ and $g(r)$ for the maximum mass solutions corresponding to several values of γ. For comparison, we also show the Schwarzschild functions $f(r) = g(r) = 1 - 2GM/r$ (black dotted line).

3.3.5 Results

In the left panel of Figure 3.2 we show the existence curve M versus ω for ground-state mini boson stars, axion-dilaton stars with $\gamma^2 = 1$ and and O(3) stars with $\gamma^2 = -1$. These curves are generated by varying the value of ϕ_0 from 0 (corresponding to the deconfinement limit $\omega \to \mu$) to a maximum value that depends on the case. We see that the existence curves in all cases have the same qualitative profile as for mini boson stars, with the characteristic spiral shape. We observe quantitative differences though: the axion-dilaton solutions reach smaller masses and exist for a smaller range of frequencies than the mini boson stars. The opposite effect is observed for the O(3) model: these solutions reach higher masses and exists for a bigger range of frequencies. These effects become more drastic as we increase γ^2 (in absolute value). On the other hand, in the deconfinement limit $\omega \to \mu$ (so $\phi_0 \to 0$) the three curves converge. This is expected since for small values of ϕ the curvature of the scalar manifold becomes irrelevant and all the models reduce to the mini boson star one.

The right panel of Figure 3.2 shows the compactness $R/(GM)$ for these families of boson stars. Here we can see that O(3) stars are not only more massive, but also more compact. Therefore, it appears that a positively curved sigma model leads to more extreme boson stars, while negative curvature tends to make them more diffuse.

The maximum mass solution in these diagrams plays an important role. Generally, one expects only the branch of solutions that connects the maximum mass solution to the $\omega \to \mu$ solution to be stable. Those that lie beyond the

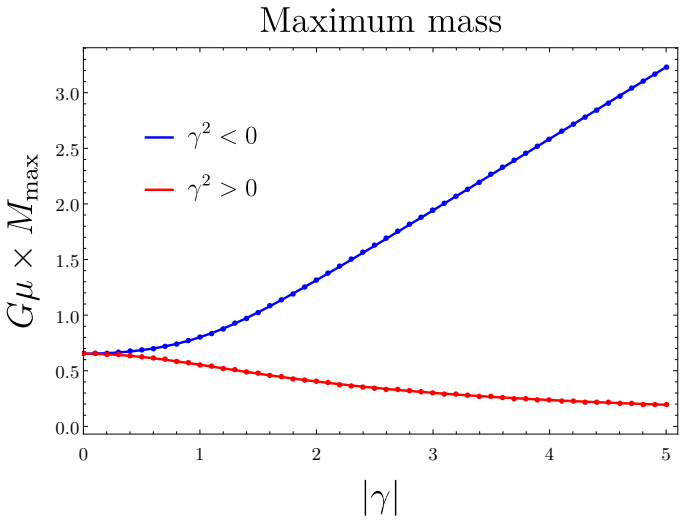

Figure 3.4: Maximum mass of boson stars as a function of $|\gamma|$ for the $\mathrm{SL}(2,\mathbb{R})$ ($\gamma^2 > 0$) and O(3) ($\gamma^2 < 0$) models. When $|\gamma|$ is large, the maximum mass of O(3) stars is proportional to $|\gamma|$, while in the case of $\mathrm{SL}(2,\mathbb{R})$ stars we find that it is inversely proportional.

maximum mass solution are in principle unstable.[6] Within the naively stable branch, the maximum mass solutions are also the most compact ones, which makes them particularly interesting. We thus focus on these solutions in what follows.

We show the profile of the metric functions $f(r)$ and $g(r)$ for the maximum mass solutions for several values of γ in Figure 3.3. Here we show the radius in units of the corresponding mass M for an easier comparison, but we recall that for a fixed μ all of these solutions have different masses. This figure clearly shows that the O(3) boson stars are more compact and produce a deeper gravitational well than their axion-dilaton counterparts. In fact, the effect is very drastic. Already for $\gamma = 2$ the axion-dilaton stars become so disperse that they can probably be well described by the Newtonian approximation. The other side of the coin is that O(3) stars resemble more and more a black hole as we increase $|\gamma|$.

It is then interesting to look at the dependence on γ of these solutions. In Figure 3.4, we show the maximum mass as a function of $|\gamma|$, for $\gamma^2 > 0$ and

[6] However, the non-linear character of the theories at hand could change this behavior, so it would be interesting to perform an analysis of the stability of the solutions.

$\gamma^2 < 0$, while in Figure 3.5 we show the compactness of these solutions.

Let us take a look first at the O(3) solutions. The most obvious thing we observe in Figure 3.4 is that the relation between $M_{\rm max}$ and $|\gamma|$ quickly becomes linear for large $|\gamma|$. In fact, by performing a linear fit to the numerical data we find that

$$M_{\rm max}^{\rm O(3)} \approx 0.565 \frac{|\gamma|}{G\mu} \tag{3.42}$$

when $|\gamma| \gg 1$. The compactness of these solutions — as illustrated in the left plot of Figure 3.5 — also increases with $|\gamma|$, with a maximum compactness that would be reached for $|\gamma| \to \infty$. It is difficult to estimate this value since it depends on the asymptotic behavior of $R/(GM)$ as a function of $|\gamma|$, which we do not know a priori. Our data strongly suggests a power-law decay and, by trying different fits, it favors an expansion of the form $R/(GM) = C_0 + C_1|\gamma|^{-1} + C_3|\gamma|^{-3} + \mathcal{O}(|\gamma|^{-5})$. By assuming this, we obtain the following fit

$$\left.\frac{R}{GM}\right|_{M_{\rm max}^{\rm O(3)}} \approx 3.29 + \frac{3.2}{|\gamma|} + \mathcal{O}\left(|\gamma|^{-3}\right) \quad \text{for } |\gamma| \gg 1\,. \tag{3.43}$$

Thus, for large $|\gamma|$ these stars are close to the compactness $R \sim 3GM$, which is usually the threshold for ultracompact objects — those with light rings. While our numerical solutions up to $|\gamma| = 5$ do not show light rings, we cannot at this point discard their existence for larger values of $|\gamma|$, for which the numerical computations become more involved.[7]

On the other hand, the behaviour of axion-dilaton stars ($\gamma^2 > 0$) is radically opposite to their O(3) counterparts, with their maximum mass and compactness quickly decreasing with γ. Performing a fit of the form $M_{\rm max} = M_0 + M_1/\gamma + M_2/\gamma^2 + \ldots$, we find that the results are consistent with $M_0 = 0$, *i.e.*, the mass tends to zero for large γ. Indeed, we find that

$$M_{\rm max}^{\rm SL(2,\mathbb{R})} \approx \frac{1.1}{G\mu\gamma} + \mathcal{O}\left(\gamma^{-2}\right) \quad \text{for } \gamma \gg 1\,. \tag{3.44}$$

In addition, the ratio $R/(GM)$ (right plot of Figure 3.5) grows very fast for large values of γ. Our results indicate that it scales with γ^2 when $\gamma \gg 1$, and in fact, a simple quadratic polynomial fit captures our numerical values with very good accuracy in all the range of γ:

$$\left.\frac{R}{GM}\right|_{M_{\rm max}^{\rm SL(2,\mathbb{R})}} \approx 12.4 + 5.48\gamma^2\,. \tag{3.45}$$

[7] Light rings do arise in boson stars in the unstable branch, as already happens in the case of mini boson stars [87]. Our results show that in the case of O(3) stars, light rings arise closer to the maximum mass solution as we increase $|\gamma|$, but it is unclear at this point whether for larger $|\gamma|$ these solutions move into the stable branch.

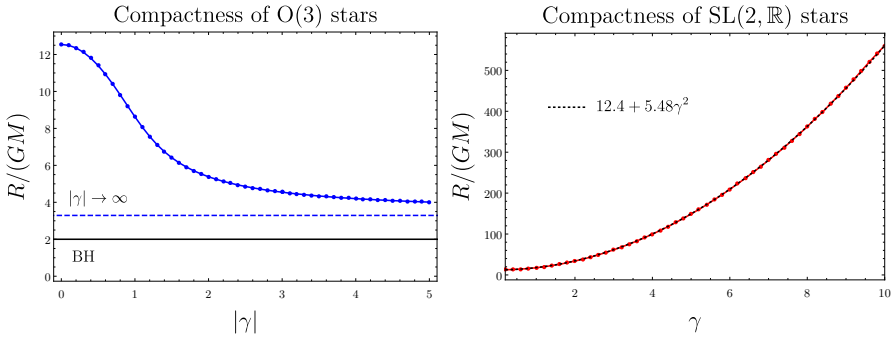

Figure 3.5: Compactness of the maximum mass O(3) and $\mathrm{SL}(2,\mathbb{R})$ boson stars as a function of $|\gamma|$. The dashed line in the left plot represents the limit of the compactness of the O(3) solutions when $|\gamma| \to \infty$, approximately $R/(GM) \approx 3.29$. In the right plot, along with our numerical results for the compactness of $\mathrm{SL}(2,\mathbb{R})$ stars, we show a quadratic fit that seems to capture perfectly the behavior of $R/(GM)$ for all values of γ.

Thus, these solutions quickly acquire very low compactnesses compared to those of mini boson stars and therefore, their gravitational field is essentially Newtonian.

Finally, we provide a few additional properties of the maximum mass solutions for a selection of values of γ in Table 3.1. It is worth emphasizing that in all the cases the charge of solutions is very similar to the mass — they are roughly proportional across all values of γ. In addition, we observe that the frequency of the $\mathrm{SL}(2,\mathbb{R})$ solutions approaches $\omega \to \mu$ when γ is large, naturally corresponding to the decompactification limit. In the case of O(3) stars, the frequency tends to a non-zero constant. In fact, our results suggest that $\omega \to \frac{2}{3}\mu$ for $|\gamma| \to \infty$.

3.4 Energy and mass scales

In the theory (3.17), we expressed the scalar field in Planck units for convenience, and as a result, the curvature scale of the sigma model, γ, is a dimensionless number. However, in order to obtain a more physically correct picture, one should work with the canonically normalized scalar field, $\hat{\Phi} = \frac{\Phi}{\sqrt{16\pi G}}$, which has dimensions of energy. As a consequence, its scalar manifold has a dimensionful curvature k corresponding to some characteristic energy scale, $|k| = E^{-2}$. The

γ	ϕ_0	ω/μ	$M \times G\mu$	$Q \times G\mu$	$R/(GM)$
0	0.5431	0.8529	0.6330	0.6530	12.4
1	0.4078	0.8932	0.5362	0.5538	17.6
2	0.2222	0.9433	0.3947	0.4034	33.9
5	0.0523	0.9868	0.1914	0.1938	149.0
i	0.6855	0.7949	0.7653	0.8012	8.54
$2i$	0.5983	0.7139	1.2065	1.3144	5.33
$5i$	0.2637	0.6771	2.8564	3.2307	3.97

Table 3.1: Properties of the maximum mass boson stars for several values of γ: scalar field at the origin, frequency, mass, charge and compactness. We remark that the numerical computation requires to determine ω with many more digits of precision than those we are showing.

parameter γ of our models is related to the dimensionful curvature by

$$\gamma^2 = -\frac{k}{16\pi G}\,. \tag{3.46}$$

Or, in terms of the energy scales,

$$|\gamma| = \frac{M_{\rm P}}{\sqrt{16\pi}E}\,. \tag{3.47}$$

Now, notice that, in general, the energy scale E of the nonlinear sigma model need not coincide with Planck scale, and it is very natural to assume that $E \ll M_{\rm P}$. Therefore, a large value of $|\gamma|$, like the ones we have studied, is indeed a natural possibility. Writing our formulas (3.42) and (3.44) for the maximum mass in terms of the energy scale E, we get

$$M_{\rm max}^{\rm O(3)} = 0.0798\frac{M_{\rm P}^3}{\mu E}\,, \quad M_{\rm max}^{\rm SL(2,\mathbb{R})} = 7.8\frac{M_{\rm P}E}{\mu}\,. \tag{3.48}$$

These relations are important as they tell us the range of energy scales for which these models give rise to astrophysical-size boson stars. The O(3) boson stars have masses comparable to the Chandrasekhar limit of fermions with mass $m_f^2 \sim E\mu$. Thus, these solutions can reach stelar masses for a wide range of values of E and μ. For instance $E \sim \mu \lesssim 1$GeV would yield solar-mass boson stars. However, in the SL$(2,\mathbb{R})$ case with $E \sim \mu$, the maximum mass is Planckian, hence making this model unviable to describe massive compact objects. The model could nevertheless still be viable if $E \gg \mu$ and the bosons are ultralight, and especially if $E \sim M_{\rm P}$ (so that $\gamma \sim 1$, as usually happens in string theory and supergravity). In that situation the SL$(2,\mathbb{R})$ stars would just be comparable to mini boson stars, although somewhat less massive and compact.

Interestingly, the radius of (maximum mass) boson stars is of the same order of magnitude in both models, and roughly given by $R \sim M_{\rm P}/(E\mu)$. We note that this is much larger than the Compton wavelength of the bosons if $E \ll M_{\rm P}$. The huge difference in masses means that, within the same radius, the O(3) model describes almost ultra-compact objects, while the $\mathrm{SL}(2,\mathbb{R})$ stars can be arbitrarily diffuse.

3.5 Discussion

We have studied boson star solutions in the O(3) and $\mathrm{SL}(2,\mathbb{R})$ sigma models. We have considered the case of minimally interacting potentials (3.21) in order to focus on the effect of the sigma model curvature on the boson stars. Our results are clear: positive curvature (O(3)) leads to massive and very compact solutions, while negative curvature ($\mathrm{SL}(2,\mathbb{R})$) produces light and (relatively) diffuse objects. In fact, the masses and compactnesses of these objects differ by many orders of magnitude if the energy scale of the nonlinear sigma model is below Planck scale — see (3.48) — but the differences are important even when $E \sim M_{\rm P}$. Therefore, the main conclusion is that the curvature of the sigma model is a crucial factor (as important as the potential) in determining the properties of boson stars. While we focused on maximally symmetric sigma models, it would of course be interesting to study how this general conclusion translates to sigma models with non-constant curvature. These, perhaps, could lead to even more drastic effects.

The case of O(3) boson stars is particularly interesting, as these objects can acquire very high compactnesses even with a minimal potential. Indeed, our analysis showed that there are presumably stable solutions with a maximum compactness of $R \sim 3.29GM$. For comparison, this is almost twice the maximum compactness of (stable) massive boson stars [12] and similar to that of solitonic boson stars [72], which are some of the most compact examples known in the literature. These O(3) boson stars are on the verge of becoming ultracompact, that is, developing light rings. Although we did not find solutions with light rings in the naively stable branch, these could perhaps exist for even larger values of the O(3) model curvature, which become increasingly difficult to explore numerically.[8] It would be otherwise interesting to explore if other potentials — including self-interactions — could increase the compactness of the solutions even more. Likewise, one may wonder if in the case of $\mathrm{SL}(2,\mathbb{R})$ stars, interacting potentials may increase their masses in a substantial way.

[8] On the other hand, it is interesting that despite being so compact these objects do not acquire light rings, since these are known to generate a nonlinear instability in horizonless objects [88].

The next natural step in the study of these boson stars would entail the analysis of their linear perturbations and stability. As we mentioned, the maximum mass boson star usually marks the limit of existence of stable solutions, but since these models have a non-standard kinetic term it would be important to investigate if this is still the case. The study of perturbations is furthermore interesting in order to determine observational properties of boson stars, such as their quasinormal modes [161] or tidal Love numbers [173, 71]. On the other hand, studying the image of these boson stars, and determining to what extent they can mimic a black hole, would also prove interesting [129, 199, 201, 200].

Another obvious extension of this work would be studying rotating boson stars, some examples of which were already found in Ref. [128] in the case of O(3) stars. It would again be interesting to focus on the regime of large curvature of the sigma model in order to investigate if rotating solutions acquire special features in that case.

Finally, one of our motivations to study nonlinear sigma models was their connection to supergravity and string theory. Although the models we have studied can be part of a supergravity action, they do not capture the whole story yet. In a supergravity version of these models, there would be a few differences. On the one hand, the unbroken U(1) symmetry would typically be gauged, and thus boson stars would be charged [138] hence generating electromagnetic fields. On the other hand, the scalar potential, the sigma model metric and the coupling between the scalar and vector fields would be constrained by supersymmetry. Thus, supergravity would provide a rich (yet restricted) set of theories in which boson star solutions arise naturally. The study of these solutions — which connect some of our most fundamental theories with objects of astrophysical interest[9] — poses a promising avenue of research.

[9]They would also have a theoretical interest, as boson stars play a role in string theory through the AdS/CFT correspondence [61, 59, 60, 177].

Chapter 4

Scalar fields from nonlinear sigma models on black hole spacetimes

In this chapter we will employ numerical relativity tools to study the theories introduced in chapter 3 on black hole spacetimes in the fully nonlinear regime. We will start with a summary of NR formalism and techniques useful in this work, so to make the text sufficiently self contained. The following section is mainly based from [35].

4.1 Elements of numerical relativity

The first step towards developing a method to solve the four-dimensional Einstein field equations on a computer is to cast it in the form of an initial value, or Cauchy, problem. This amounts to consistently express the gravitational field and its first derivative with respect to time at an initial time instance, which requires to decompose the global four-dimensional spacetime into three spatial directions and a time dimension. This procedure is known as *3+1 decomposition*. It is therefore assumed that the spacetime is foliated by non-intersecting three-dimensional spacelike surfaces Σ defined as surfaces with constant scalar function t, which can be thought of a global time function. A vector field proportional to the gradient of the function t can be defined as a vector normal to the 3-surfaces,

$$n^\mu = -\alpha\, g^{\mu\nu}\, \nabla_\nu t. \tag{4.1}$$

The function α defines the proper time change between 3-surfaces along the normal n^μ and it is called the *lapse* function. The lapse function is related to the norm of $\nabla_\mu t$ so that the normal vector has unit norm $n_\mu n^\mu = -1$. One can now define the induced metric on the 3-surfaces Σ as a combination of the 4-d metric and the normal vector field

$$\gamma_{\mu\nu} = g_{\mu\nu} + n_\mu n_\nu. \tag{4.2}$$

Another useful quantity encoding the geometry of the full spacetime manifold is the extrinsic curvature of the spatial slices, defined as the Lie derivative of the induced metric along the flow on n^μ, i.e.

$$K_{\mu\nu} = -\frac{1}{2}(\mathcal{L}_{\mathbf{n}}\gamma)_{\mu\nu}. \tag{4.3}$$

This equation makes clear that the extrinsic curvature encodes the changes in the metric $\gamma_{\mu\nu}$ between spacelike slices, modulo coordinate transformations. It is possible to express the relevant equations in a tetrad basis adapted to the chosen foliation, with e_i^μ three spatial vectors defined onto Σ, and

$$e_0^\mu = t^\mu = \alpha n^\mu + \beta^\mu. \tag{4.4}$$

The newly-defined vector t^μ is such that $t^\mu \nabla_\mu t = 1$ for any spatial *shift* vector β^μ. When t^μ is chosen to connect points with the same spatial coordinates on different 3-slices, then the vector β^μ encodes how such spatial coordinates move on Σ with respect to the normal vector. Then, in the basis $\{e_0^\mu, e_i^\mu\}$, the shift and normal vectors have components

$$\beta^\mu = (0, \beta^i), \qquad n^\mu = (\alpha^{-1}, -\alpha^{-1}\beta^i). \tag{4.5}$$

The relationship between the foliation and the quantities introduced until here is sketched in Figure 4.1. From here, it is possible to decompose the metric tensor of the full spacetime into the tetrad, to get

$$g_{\mu\nu} = \begin{pmatrix} -\alpha^2 + \beta_i\beta^i & \beta_i \\ \beta_j & \gamma_{ij} \end{pmatrix} \tag{4.6}$$

or, in the well-known line element form

$$\mathrm{d}s^2 = -\alpha^2 \mathrm{d}t^2 + \gamma_{ij}(\mathrm{d}x^i + \beta^i \mathrm{d}t)(\mathrm{d}x^j + \beta^j \mathrm{d}t). \tag{4.7}$$

Thus, the field quantity (γ_{ij}, K_{ij}) are the data defined on the three-surfaces Σ that are to be integrated forward in time. To proceed, one needs to cast the

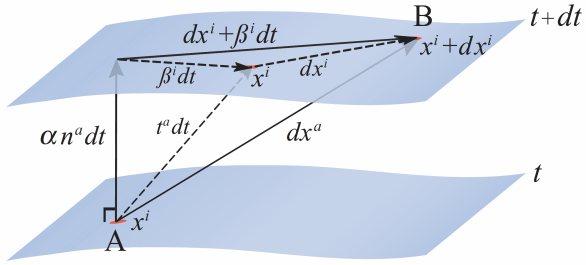

Figure 4.1: Spacetime decomposition into a $3+1$ scheme and related important vectors. The sketch is reproduced from [35].

Einstein field equations in terms of the three-metric and extrinsic curvature, supplemented by some constraint equations granting the embedding of such 3-dimensional quantities into the global spacetime manifold. Starting from the right-hand-side, the stress-energy tensor can be decomposed into its components as

$$\begin{aligned} \rho &= n_\mu n_\nu T^{\mu\nu}, & S_i &= -\gamma_{i\mu} n_\nu T^{\mu\nu}, \\ S_{ij} &= \gamma_{i\mu}\gamma_{j\nu} T^{\mu\nu}, & S &= \gamma^{ij} S_{ij}\,, \end{aligned} \tag{4.8}$$

where $n^\mu = (\partial_t^\mu - \beta^k \partial_k^\mu)/\alpha$ in the adapted coordinates. Projecting the curvature tensors onto the 3-dimensional slices and onto the normal direction one obtains two constraints equations and replacing the projections into the Einstein field equations one is able to get evolution equations for γ_{ij} and K_{ij}. In particular, one obtains the *Hamiltonian constraint*

$$R + K^2 - K_{ij}K^{ij} = 16\pi\,\rho, \tag{4.9}$$

the *Momentum constraint*

$$D_j K_i^j - D_i K = 8\pi\, S_i, \tag{4.10}$$

where the symbol D stands for the covariant derivative compatible with the metric of the spatial slices, together with the evolution equations

$$\begin{aligned} \mathcal{L}_{\mathbf{t}} K_{ij} =& - D_i D_j \alpha + \alpha(R_{ij} - 2K_{il}K_j^l + K K_{ij}) \\ & - 8\pi\,\alpha\left(S_{ij} - \frac{1}{2}\gamma_{ij}(S-\rho)\right) + \mathcal{L}_\beta K_{ij}, \end{aligned} \tag{4.11}$$

$$\mathcal{L}_{\mathbf{t}} \gamma_{ij} = -2\alpha K_{ij} + \mathcal{L}_\beta \gamma_{ij}. \tag{4.12}$$

These are known as the standard $3+1$ or ADM equations, after Arnowitt, Deser and Misner [17]. Thus, the ADM decomposition yields constraints equations

with no time derivatives relating quantities on a single hypersurface, and first-order in time evolution equations defining the change of the dynamical quantities between different hypersurfaces.

However, directly implementing the equations (4.11)-(4.12) would result in an unstable numerical evolution, with certain modes growing faster than exponentially. This property can be more easily seen after performing a first-order reduction of the equations, i.e. introducing new auxiliary variables to make the equations of motions contain only first-order derivatives[1]. Then, the problem would reduce schematically to

$$\partial_t \boldsymbol{u} + \boldsymbol{A}^i \, \partial_i \boldsymbol{u} = \boldsymbol{S}, \tag{4.13}$$

with $\boldsymbol{u}$ the solution vector, $\boldsymbol{A}^i$ a set of $n \times n$ velocity matrices and $\boldsymbol{S}$ the source terms. Choosing a unit vector $\boldsymbol{n}^i$, one defines the *characteristic matrix* $\boldsymbol{P} = \boldsymbol{A}^i n_i$. In the convention of [35], the system (4.13) is

- **strongly hyperbolic**, if $\boldsymbol{P}$ has real eigenvalues and a complete set of eigenvectors for each n^i;
- **weakly hyperbolic**, if $\boldsymbol{P}$ has real eigenvalues but not a complete set of eigenvectors.

A system which is strongly hyperbolic has a *well-posed* solution, i.e., given some suitable initial data, the solution exists, it is unique and it depends continuously on the initial data. Moreover, the solution grows at most exponentially, while this is not the case for a weakly hyperbolic system. This means that the solution $\boldsymbol{u}(t)$ satisfies, for some norm $||.||$ on the space of solutions,

$$||\boldsymbol{u}(t)|| \leq \Lambda e^{kt} ||\boldsymbol{u}(0)||, \tag{4.14}$$

with $\boldsymbol{u}(0)$ the initial data and Λ, k two constants independent on the initial data. It has been shown that the ADM equations, after a first-order reduction, are weakly hyperbolic [146]. Two key methods have been introduced to cast the ADM equations into a strongly-hyperbolic form, the BSSN [209, 36] and CCZ4 [10] formalisms. It is worth to mention that other methods have been explored to solve the instability of the $3+1$ decomposition, namely the *generalised harmonic coordinates* approach, which lead to the first BH binary simulation [194]. The method does not rely on a $3+1$ decomposition, but works directly with the four-dimensional Einstein equations, introducing some gauge functions related to the trace of the connection coefficients. This method leads to second-order in time differential equations.

[1] The ADM equations are generally presented as second-order in space. Their first-order reduction simplifies the discussion of hyperbolicity.

The BSSN formalism is based on the introduction of a conformal rescaling of the ADM equations, as well as the introduction of trace-free independent variables. A conformal factor $\psi = e^{\phi}$ is introduced so that the spatial metric becomes

$$\gamma_{ij} = \psi^4 \tilde{\gamma}_{ij} = e^{4\phi} \tilde{\gamma}_{ij}, \tag{4.15}$$

with $\det(\tilde{\gamma}_{ij}) = 1$, and the extrinsic curvature is decomposed into a conformal traceless part and a trace piece

$$K_{ij} = e^{4\phi} \tilde{A}_{ij} + \frac{1}{3} \gamma_{ij} K. \tag{4.16}$$

An additional quantity is introduced, the conformal connection functions

$$\tilde{\Gamma}^i = \tilde{\gamma}^{ij} \Gamma^k_{jk} = -\partial_j \tilde{\gamma}^{ij}, \tag{4.17}$$

with $\tilde{\Gamma}^i_{jk}$ the Christoffel symbols of the conformal metric. Thus, the BSSN formalism considers as independent variables the set $\{\phi, \tilde{\gamma}_{ij}, \tilde{A}_{ij}, K, \tilde{\Gamma}^i\}$. The evolution equations for these dynamical variables are presented in appendix C.

The Z4 formalism adds some constraint damping terms to the BBSN equations [51]. Such terms improve the accuracy of the integration, controlling the numerical noise. The damping terms are introduced directly in the Einstein field equations of the full spacetime

$${}^{(4)}R_{\mu\nu} + 2\nabla_{(\mu} Z_{\nu)} - 2\kappa_1 n_{(\mu} Z_{\nu)} + \kappa_1 (1 + \kappa_2) g_{\mu\nu} n_\rho Z^\rho = 8\pi \left(T_{\mu\nu} - \frac{1}{2} g_{\mu\nu} T \right), \tag{4.18}$$

where Z^μ is a vector that is required to vanish on solutions to the field equations and κ_1, κ_2 some constant damping parameters. These parameters were introduced in [122] and the constraints are effectively damped for $\kappa_1 > 0$, $\kappa_2 > -1$. The field equation (4.18) is then decomposed in the 3+1 formalism and made conformal and covariant (CCZ4). The BBSN variables are thus complemented by the components of the Z^μ vector, i.e.

$$\Theta = -n_\mu Z^\mu, \qquad \Theta^i = \gamma^i{}_\mu Z^\mu. \tag{4.19}$$

The three-vector Θ^i is then combined with the covariant Christoffel symbols,

$$\hat{\Gamma}^i = \tilde{\Gamma}^i + 2\tilde{\gamma}^{ik} \Theta_k. \tag{4.20}$$

Let us remark that in the latest implementations of the CCZ4 formalism [196], the conformal factor has been defined as

$$\tilde{\gamma}_{ij} = \chi \gamma_{ij}, \tag{4.21}$$

such that $\chi = (\det(\gamma_{ij}))^{-1/3}$. Thus, the dynamical variables in the CCZ4 scheme are the set $\{\chi, \tilde{\gamma}_{ij}, K, \tilde{A}_{ij}, \Theta, \hat{\Gamma}^i\}$. Again, we provide the evolution equations for these quantities in appendix C. Both these methods are strongly hyperbolic and give rise to well-posed solutions. We will make use of both schemes in the rest of the chapter.

To continue, one needs to specify the choice of the gauge variables (α, β^i), which is equivalent to a choice of coordinates evolution in between the slices. The choice of a gauge guaranteeing a well-behaved evolution is non-trivial. The easiest choice is the *geodesic slicing* $\alpha = 1$, $\beta^i = 0$, but it is be prone to forming coordinate singularities. An important family of gauge choices is the *Bona-Masso* slicing condition [52],

$$\partial_t \alpha = -\alpha^2 f(\alpha) K, \tag{4.22}$$

with $f(\alpha)$ an arbitrary positive function of the lapse. A special case arises for $f(\alpha) = 2/\alpha$, which results in $\alpha = 1 + \ln(\det(\gamma_{ij}))$. This is a singularity-avoiding slicing of the lapse. Together with the following conditions on the shift,

$$\partial_t \beta^i = \frac{3}{4} B^i, \quad \partial_t B^i = \partial_t \tilde{\Gamma}^i - \eta B^i, \tag{4.23}$$

with $\tilde{\Gamma}^i = \tilde{\gamma}^{jk}\tilde{\Gamma}^i_{jk}$ and η a positive constant, these choices are known as *moving puncture gauge*.

A key ingredient of a stable numerical simulation are well-behaved initial conditions. One needs to specify the values of the system's variables on the initial time spacelike hypersurface Σ, in a way that satisfies the hamiltonian and momentum constraint equations. These equations give rise to our constraints, which have to be supplemented with gauge choices and the initial value of the propagating GR degrees of freedom and their time derivatives. In imposing initial conditions, one should be careful about the uniqueness of the solution, as different metrics could satisfy the constraints for the same matter content and boundary conditions. A simple example are the Schwarzschild and Kerr metrics, both vacuum spacetime solutions that are asymptotically flat, but the problem of uniqueness is especially relevant when the matter distribution is a fundamental field ϕ [20].

Similarly to the BSSN and CCZ4 schemes, it is useful to decompose the constraint equations into a Conformal Transverse-Traceless (CCT) form. As before, the spatial metric is taken to be the product of a conformal factor and a unit-determinant metric $\gamma_{ij} = \psi^4 \tilde{\gamma}_{ij}$, with $\det \tilde{\gamma}_{ij} = 1$. Then, one separates the extrinsic curvature into a traceless and and trace part

$$K_{ij} = \psi^{-2} \tilde{A}_{ij} + \frac{1}{3} \gamma_{ij} K, \tag{4.24}$$

which allows to write the hamiltonian constraint as

$$8\tilde{D}^2\psi - \psi\tilde{R} - \psi^5 K^2 + \psi^5 K_{ij}K^{ij} = -16\pi\psi^5\rho, \tag{4.25}$$

with $\tilde{D}^2 = \tilde{\gamma}^{ij}\tilde{D}_i\tilde{D}_j$. To proceed, the traceless tensor $\tilde{A}_{ij}$ is decomposed into a transverse-traceless part and a longitudinal one related to the gradient of a vector

$$\tilde{A}^{ij} = \tilde{A}^{ij}_{\mathrm{TT}} + \tilde{A}^{ij}_{\mathrm{L}}, \tag{4.26}$$

with

$$\tilde{A}^{ij}_{\mathrm{L}} = \tilde{D}^i W^j + \tilde{D}^j W^i - \frac{2}{3}\tilde{\gamma}^{ij}\tilde{D}_k W^k. \tag{4.27}$$

Then, the momentum constraint becomes

$$\left(\tilde{\Delta}_{\mathrm{L}} W\right)^i - \frac{2}{3}\psi^6\tilde{\gamma}^{ij}\tilde{D}_j K = 8\pi\psi^{10}S^i, \tag{4.28}$$

with $\tilde{\Delta}_{\mathrm{L}}$ the vector Laplacian. Equation (4.28) is then solved for W^i after specifying $\tilde{\gamma}_{ij}$, K to be a flat metric and a constant value, and the hamiltonian constraint (4.25) is then solved for ψ. In the rest of the chapter, we will make use of a recently introduced variation to this formalism, that specifies the conformal factor ψ and solves for K, known as the CCTK method [20]. This allows to solve an algebraic equation for K,

$$K^2 = 12\psi_0^{-5}\partial^i\partial_i\psi_0 + \frac{3}{2}\psi_0^{-12}\bar{A}_{ij}\bar{A}^{ij} + 24\pi\rho, \tag{4.29}$$

instead of an elliptic equation for ψ, that might suffer from uniqueness issues. In equation (4.29), a initial guess for ψ is introduced, as $\psi = \psi_0 + u$, with u satisfying equation (4.25) when linearized with respect to ψ. This method has been shown to ensure stability of the solutions and rapid convergence in several NR applications like spacetimes with a scalar field matter component, which will be discussed in the following sections.

4.2 Introduction

With the motivation of understanding environmental effects around GW sources, we will focus on a DM environment composed by the scalar fields introduced in chapter 3. As discussed in the introduction 1, GW signals could carry information about the environments their sources are evolving in. The exchange of energy and angular momentum between the binary and such environments modify the inspiral behaviour with respect to a vacuum GR evolution. Achieving a detailed understanding of these effects is necessary to characterise the

environment and possibly extract new information about its constituents and it is crucial to identify systematics and biases in the data analysis pipelines.

Light scalar fields have been largely considered in the literature as possible DM candidates, as they emerge naturally from extensions to the Standard Model (SM) as well as from String Theory (ST) [18, 124]. The most common theory of this kind is the one of a complex scalar field Φ with a Lagrangian of the form

$$\mathcal{L}_\Phi = -\frac{1}{2}\partial_\mu \Phi \partial^\mu \bar{\Phi} - V\left(|\Phi|^2\right). \tag{4.30}$$

Such systems have been extensively discussed in the literature, usually taking the potential to be a mass term $V \sim \mu^2|\Phi|^2$. Such candidates have been shown to have a rich phenomenology when interacting with compact objects. For instance, they can build superradiant states around rapidly spinning BHs, which can in turn imprint specific signatures on the inspiral of a light secondary object [56, 34, 31]. Recent works have shown that scalar fields can grow non-trivial over-densities around equal-mass binaries that are long-lived and induce a dephasing of the inspiral [27, 25]. Different choices for the potential term have also been explored. Self-interactions of the scalar field have been shown to impact the total GW dephasing and, more generally, the system's phenomenology, with attractive self-interactions leading to a disruption of the cloud known as *bosenova* [25].

We will consider here an extension to the theories (4.30), which is given by promoting the kinetic term to a nonlinear sigma model,

$$\mathcal{L}_\phi = -\frac{1}{2}G_{AB}(\phi)\nabla_\mu \phi^A \nabla^\mu \phi^B - V\left(\phi^A\right). \tag{4.31}$$

In these theories, a set of scalars $\{\phi^A\}_{A=1,\dots,N}$ can be thought of as coordinates on a space called scalar manifold, with metric G_{AB}. In general, this space can be curved. Such models emerge naturally in supergravity and compactifications of string theories [64, 54, 66] and have been thoroughly discussed in chapter 3. This chapter presents the implementation of such theories in the numerical-relativity (NR) code `GRChombo` [13, 196] and has the goal of characterising the influence of the sigma model parameters on the field's phenomenology in its full nonlinear regime. Previous works have discussed nonlinear sigma models with numerical techniques in the context of critical collapse [157, 156]. We present the first implementation of these models in a full NR code and in the context of isolated BHs and binary BH inspirals. This work is possible because of the modular and flexible structure of this code, which allows to study exotic physical systems and fundamental fields in GR [113, 127, 112, 105, 116, 166] as well as beyond-GR effects motivated by string theory or EFTs in the regime where nonlinear terms can be important [111, 110, 15, 14, 97, 98, 16].

The chapter is organised as follows. In Section 4.3 we recall the nonlinear sigma models that will be the object of our work. In Section 4.4 we outline the implementation of the theory (4.31) in the `GRChombo` code and we present the numerical results. In section 4.4.1 we describe the evolution of such fields on the background of an isolated black hole and characterise the accretion process for various curvatures of the sigma model. In section 4.4.2 we treat the case of a binary black hole evolution in the presence of this type of scalar field. Finally, we conclude in 4.5 by discussing our results and outlining possible future directions.

We follow the conventions in Wald's book [221]. Greek letters $\mu, \nu \ldots$ denote spacetime indices and they run from 0 to d; Latin letters $i, j, \ldots$ denote indices on the spatial hypersurfaces and they run from 1 to 3. We set $G = c = 1$.

4.3 Nonlinear sigma models

Let us recall briefly the theories were derived in [66] to study spherically symmetric soliton solutions (boson stars). Motivated by fields arising in supergravity and string theory [186], we consider the general theory given by

$$\mathcal{L} = -\frac{\partial_\mu \tau \partial^\mu \bar{\tau}}{2\gamma^2 \mathrm{Im}(\tau)^2} - U\left(\mathcal{T}^2\right), \tag{4.32}$$

with

$$\mathcal{T}^2 = \frac{1}{\gamma^2}\left(\frac{1+|\tau|^2}{\mathrm{Im}(\tau)} - 2\right). \tag{4.33}$$

The field τ generates a scalar manifold that is maximally symmetric, thus this is a maximally-symmetric sigma model. One can also construct the negative or positive-curvature sigma models, with a hyperbolic space or a sphere as the scalar manifold. This is to say that the Lagrangian (4.32) is invariant under $\mathrm{SL}(2,\mathbb{R})$ or $\mathrm{O}(3)$ symmetry, respectively. We can write the two theories in a unified form as follows. By changing variables into (4.32) to

$$\Phi = \frac{2}{\gamma}\frac{1+i\tau}{1-i\tau}, \tag{4.34}$$

the sigma model Lagrangian becomes

$$\mathcal{L} = -\frac{\partial_\mu \Phi \partial^\mu \bar{\Phi}}{2\left(1-\frac{\gamma^2}{4}|\Phi|^2\right)^2} - \frac{\mu^2|\Phi|^2}{2\left(1-\frac{\gamma^2}{4}|\Phi|^2\right)}, \tag{4.35}$$

which is only dependent on γ^2 and we introduced a potential term polynomial in $\mathcal{T}^2$ with μ the mass of the field. Then, with $\gamma^2 > 0$ the scalar manifold is the hyperbolic space, with $\mathrm{SL}(2,\mathbb{R})$ symmetry group, whereas with $\gamma^2 < 0$ it is the 2-sphere, O(3) symmetry. For $\gamma = 0$ it reduces to the complex scalar field (4.30).

The field Φ is invariant under the U(1) symmetry, whose Noether charge is associated to particle number conservation. Complex scalar fields behaving asymptotically as $\Phi \sim \phi_0 e^{i\mu t}$ give rise to a stationary stress-energy tensor and, thus, stationary energy density. Scalar fields with these properties have been extensively studied, as they evade the no-hair theorem assumptions and allow the growth of a non-trivial profile around isolated BHs [136, 130].

4.4 Numerics

In this section, we discuss the implementation of the equations of motion arising from (4.35) in the `GRChombo` code. `GRChombo` is an adaptive mesh refinement based code developed to perform numerical simulations with hybrid MPI/Open MP parallelism [13, 196]. We note that this code is developed and made open source by the GRTL collaboration [2]. The code implements both BSSN and CCZ4 formalisms with the moving puncture gauge to handle BH singularities and it is widely used as a tool to explore questions in fundamental physics. It is complemented by an apparent horizon solver to identify BHs in the domain and it makes possible to extract several important quantities like the gravitational radiation at the boundary and the spacetime ADM mass.

When varying the sigma model Lagrangian with respect to the field, one gets the Einstein-Klein Gordon equation

$$\nabla_\mu \nabla^\mu \Phi + \frac{\gamma^2 \bar{\Phi} \nabla_\mu \Phi \nabla^\mu \Phi}{2\left(1 - \frac{\gamma^2}{4}|\Phi|^2\right)} - 2\Phi \left(1 - \frac{\gamma^2}{4}|\Phi|^2\right)^2 U'(|\Phi|^2) = 0\,, \tag{4.36}$$

where we redefine the potential as dependent on $|\Phi|^2$ only for compactness, with

$$U(|\Phi|^2) = -\frac{\mu^2 |\Phi|^2}{2\left(1 - \frac{\gamma^2}{4}|\Phi|^2\right)}, \tag{4.37}$$

and $U'(x) = \mathrm{d}U/\mathrm{d}x$. Varying the Lagrangian with respect to the metric yields the Einstein field equations with the stress-energy tensor associated to the field Φ. In order to evolve this set of equations on a computer, we project them on a

[2] GRTL GitHub page.

$(3+1)$ slicing following the Arnowitt-Deser-Misner formalism [17]. We write the line element in the form

$$\mathrm{d}s^2 = -\alpha^2 \mathrm{d}t^2 + \gamma_{ij}(\mathrm{d}x^i + \beta^i \mathrm{d}t)(\mathrm{d}x^j + \beta^j \mathrm{d}t)\,, \tag{4.38}$$

with (α, β^i) the lapse functions and shift vector and γ_{ij} the 3-dimensional spatial metric.[3] The field's stress energy tensor is decomposed in the components

$$\begin{aligned} \rho &= n_\mu n_\nu T^{\mu\nu}, \qquad S_i = -\gamma_{i\mu} n_\nu T^{\mu\nu}, \\ S_{ij} &= \gamma_{i\mu}\gamma_{j\nu} T^{\mu\nu}, \quad S = \gamma^{ij} S_{ij}\,, \end{aligned} \tag{4.39}$$

with $n^\mu = (\partial_t^\mu - \beta^k \partial_k^\mu)/\alpha$ the future-directed unit-norm four-vector. We explicitly provide the equations for the stress-energy tensor quantities and the equations of motion of the field in the $(3+1)$ decomposition in Appendix C.3. Let us remark here that the inclusion of the modified Klein-Gordon equation followed by the scalar fields we consider does not alter the well-posedness properties of the evolution equations obtained in the BSSN or CCZ4 method. This is because no additional higher-order derivatives of the metric quantities are introduced.

We obtain initial conditions that satisfy the Hamiltonian and Momentum constraints with the code `GRTresna` [21], which uses the recently proposed CTTK method [20] based on the standard Conformal Transverse-Traceless decomposition. In particular, we use the "hybrid CTTK" method (see [20] for further details) to solve the constraints equations, which enables us to obtain second-order convergent initial data (see Appendix C.4).

For the runs with single BH we use a computational domain of $L = 512M$ with the BH situated at the centre of the grid, and $N = 64$ grid points on the coarsest level. We employ 9 levels of refinement with a refinement ratio of $2:1$ (fixed mesh refinement), which results in a finest resolution of $dx_{finest} = M/32$ on the finest grid, giving ~ 75 grid points across the BH horizon in the quasi-isotropic Kerr coordinates [160] that we use to set the initial conditions for the metric.

For the binary BH (BBH) mergers we have chosen $L = 1024M$, with $N = 128$ grid points on the coarsest level, with 10 levels of refinement, which results in a resolution of $dx_{finest} = M/64$ on the finest grid, which gives again roughly 75 points across the horizon of each BH prior to their merger. We employ adaptive mesh refinement (AMR), using the tagging criterion explained in Section 4 of [196].

[3] Let us note here that the 3d metric γ_{ij} should not be confused with the field's parameter γ^2, which will always appear as a squared scalar.

For both type of simulations we use 4^{th} order finite differences to discretise the spatial derivatives and a standard 4^{th} order Runge-Kutta time integrator to step forward in time.

4.4.1 Isolated black hole

We simulate the evolution of the scalar field (4.35) around a Schwarzschild BH for different masses of the scalar field as well as sigma model curvatures. We take as initial condition a uniform field distribution, such that $\Phi|_{t=0} = \phi_0$, with $\phi_0 \in \mathbb{R}$, and $\Pi|_{t=0} = -i\mu\phi_0$, with $\Pi = \frac{1}{\alpha}(\partial_t\Phi - \beta^i\partial_i\Phi)$ the conjugate momentum of the field. Some tapering of the initial distribution towards the grid's boundaries was implemented in the simulations to reduce boundary artefacts. When varying the scalar field mass μ, we adjust the field amplitude so that the initial density stays of order $\rho|_{t=0} \sim \mu^2\phi_0^2 \sim 10^{-9}M^{-2}$. This value is consistent with previous numerical work on scalar fields on BH spacetimes [83, 25] and it is comparable to matter densities in DM halos grown adiabatically or through superradiance, while larger than current constraints of DM densities in galactic environments. We choose extrapolating boundary conditions with a first-order scheme for the scalar field variables, to allow a non-zero oscillating value at infinity. This allows for a superposition of ingoing and outgoing modes. We checked that this choice of boundary conditions did not significantly impact the simulations results for different sizes of the simulation box, and we used a large domain length to minimise boundary artifacts. We plot the radial density profile in the vicinity of the BH at different times in Figure 4.2. We choose the values of γ^2 to be $\pm 10^5$ so that $M|\gamma^2|\sqrt{\rho}|_{t=0} \sim 3$, which mimics the same behaviour as in [66].

In all cases, the scalar field accretes on the central BH at early times and the density grows in the inner region of the domain. For a small field mass $\mu M = 0.1$, the $\mathrm{SL}(2,\mathbb{R})$ sigma model, with $\gamma^2 > 0$, produces a denser and more compact distribution than the trivial case. On the other hand, the O(3) model, $\gamma^2 < 0$, yields lower central densities and a spread-out profile. Thus, $\gamma^2 > 0$ gives an attractive self-interacting dynamics that enhances the field accretion, whereas $\gamma^2 < 0$ shows a repulsive self-interaction. For a heavier mass of the scalar field $\mu M = 1$, the three cases generate the same accretion profile. The mass term dominates the dynamics over the non-linear self-interactions induced by the scalar manifold's curvature. For the heavier mass simulations, we use a time step given by $dt_{\text{multiplier}} = 0.0625$ (with $\Delta t_{coarsest} = L/N \cdot dt_{\text{multiplier}}$),[4] which allows to resolve the scalar field oscillations on the coarsest level.

[4] This is four times smaller than the one we generally use ($dt_{multiplier} = 0.25$), which is given by the Courant–Friedrichs–Lewy (CFL) condition of our discretisation scheme.

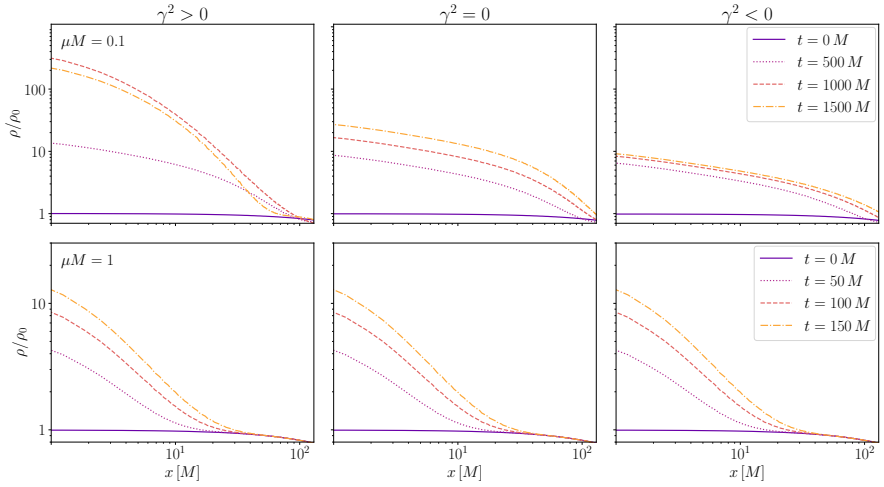

Figure 4.2: Radial density profile around a Schwarzschild BH for different values of γ^2. The top panels are obtained with a scalar field mass of $\mu M = 0.1$. The bottom panels correspond to a scalar mass of $\mu M = 1$.

4.4.2 Binary black hole

We simulate a binary black hole with BHs of equal masses $m_{(1)} = m_{(2)} = 0.48847892320123M$, initial separation $12.21358M$ and initial momenta $p_{(i)}/M = (\pm 0.0841746, \mp 0.000510846, 0)$. These initial conditions were tuned to have quasi-circular initial orbits in the absence of a dark matter cloud, a total ADM mass of $M_{ADM} = M$, and such that the two black holes merge in approximately ten orbits. We superpose the solutions for two boosted black holes as described in [35, 53], using a perturbative solution for the conformal factor that is accurate up to order $(P^i P_i)^2$, and we choose again an initial uniform distribution for the scalar field such that $(\Phi_{t=0}, \Pi_{t=0}) = (\phi_0, -i\mu\,\phi_0)$. Then we solve the Hamiltonian and momentum constraints using the CTTK approach as mentioned above.

When studying the dephasing of the waveforms in the different BBH systems considered, we have chosen to align them at a given frequency in the same way as in [16], which enables us to get more consistent results which are less affected by the ejection of the junk radiation. The frequency of the gravitational wave as a function of time can be estimated by computing the gradient of the trajectories of the punctures or the gradient of the phase of the gravitational wave and we have chosen the initial frequency to be $f_0 = 0.00716/M$, which

corresponds to the time slice that we refer to as t_0.

Light candidate, $\mu M = 0.3$

We first consider a scalar field mass of $\mu M = 0.3$. The Compton wavelength of the field $\lambda_C = 2\pi/\mu \sim 20$ is then larger than the initial separation of the binary. We run three simulations with the same initial conditions and $\gamma^2 \in \{10^5, 0, -10^5\}$ respectively. We plot the density evolution on the $z = 0$ plane in Figure 4.3, normalised with respect to the uniform density at time $t = 0$.

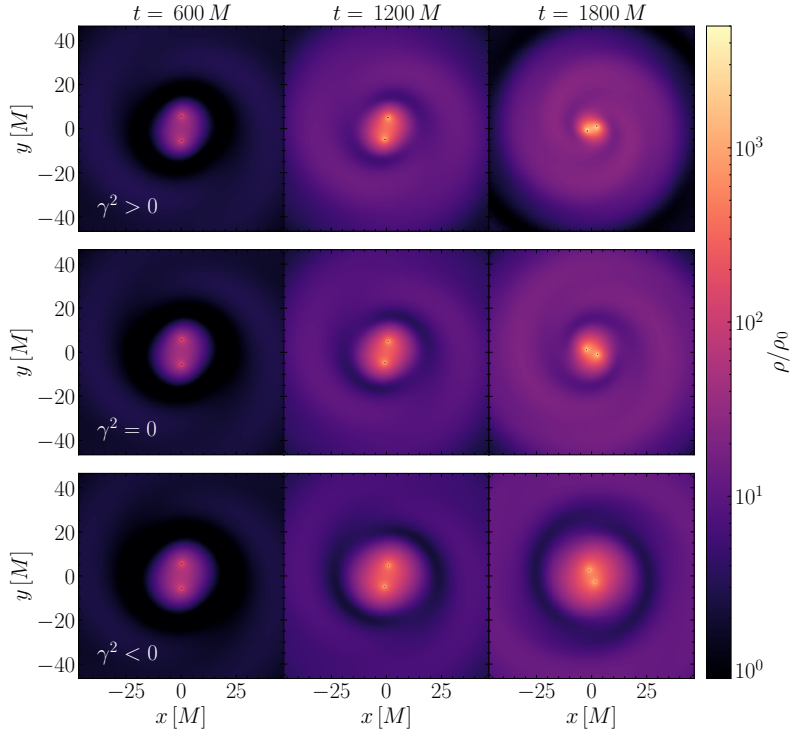

Figure 4.3: Scalar field density evolution around an equal-mass BBH for $\mu M = 0.3$ and $\gamma^2 = 10^5$ (top), $\gamma^2 = 0$ (middle), $\gamma^2 = -10^5$ (bottom).

For all scalar manifold's curvatures, the field builds up an over-density around both BHs, that grows in magnitude as the binary shrinks. Comparing the distributions at late times, the case $\gamma^2 > 0$ forms a compact cloud around the

BBH, that rapidly decays with the radius to lower density values. On the other hand, $\gamma^2 < 0$ gives rise to a more diffused cloud, which reaches lower densities in the region in between the binary components and decays more slowly with the radius. This would suggest that $\gamma^2 > 0$ behaves like an attractive self-interacting field, whereas $\gamma^2 < 0$ displays a repulsive self-interaction, resulting in a spread-out distribution. We remind that the $\gamma^2 = 0$ case reduces to a non-interacting, minimally-coupled massive scalar.

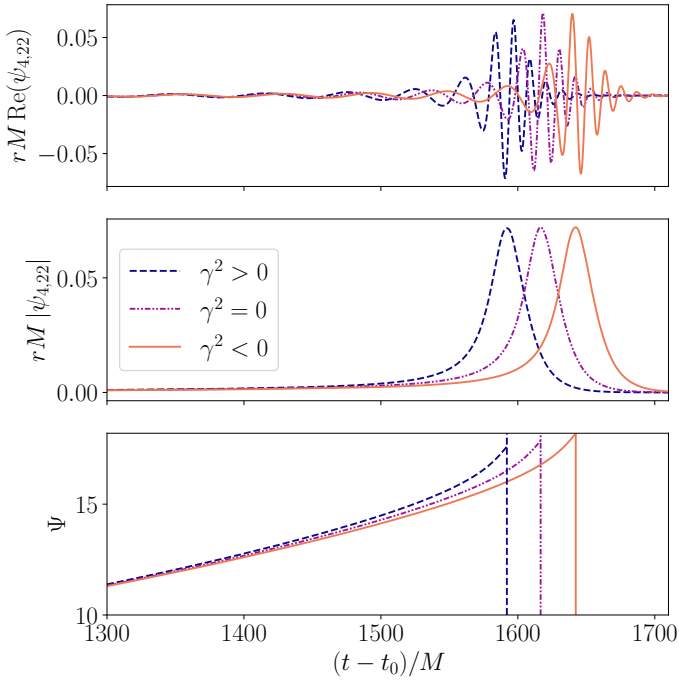

Figure 4.4: GW emission of an equal-mass BBH for $\mu M = 0.3$. The top panel shows the real part of the Weyl scalar ψ_4 extracted at $r = 50M$, while the middle panel plots its absolute value. The bottom panel shows the accumulated orbital phase Ψ.

The impact of the sigma model curvature on the inspiral is displayed in Figure 4.4. Both positive and negative curvatures induce a dephasing of the GW emission with respect to the non-interacting case. The positive curvature case merges first, in agreement with the intuition that $\gamma^2 > 0$ corresponds to attractive self-interactions. In the same way, $\gamma^2 < 0$ makes the inspiral phase

last longer than in the non-interacting case. The bottom panel of the figure shows the accumulated orbital phase in the three inspirals, which we define as half the complex phase of the $l = m = 2$ mode of the Weyl scalar ψ_4.

Heavier candidate, $\mu M = 0.6$

We perform the same analysis as the one presented in section 4.4.2 with a scalar field of double the mass, i.e. we now consider $\mu M = 0.6$. The Compton wavelength is thus $\lambda_C \sim 10M$, comparable to the initial separation of the BHs. In Figure 4.5 we plot the scalar field density at different times of the evolution for the same three choices of γ^2 as in the previous section. A first inspection of the density distributions shows a more complex cloud structure than for the light particle cases. The shorter Compton wavelength imprints a stronger wave-like behaviour to the field at scales commensurate to the BHs orbital radii.

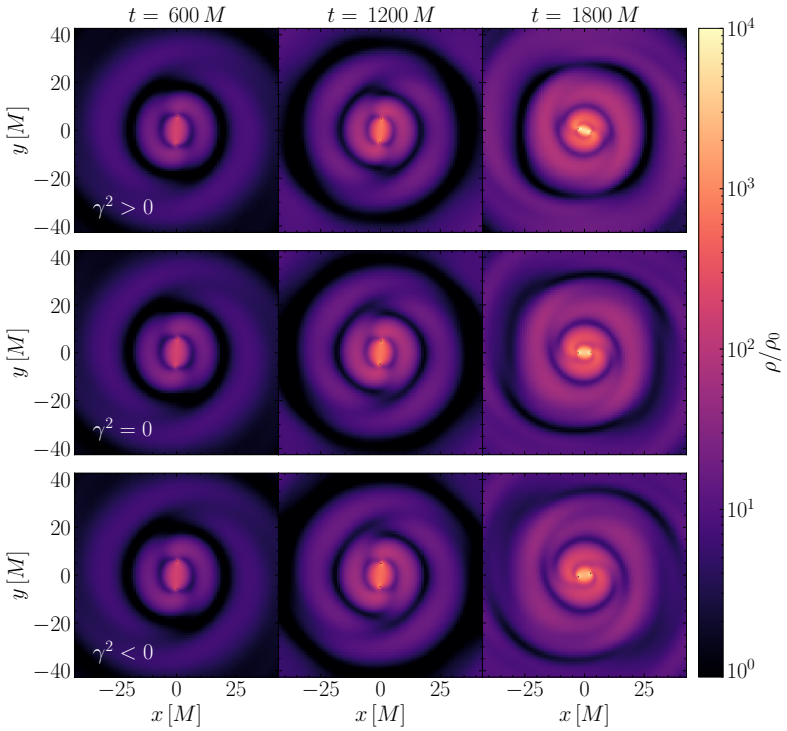

Figure 4.5: Scalar field density evolution around an equal-mass BBH for $\mu M = 0.6$ and $\gamma^2 = 10^5$ (top), $\gamma^2 = 0$ (middle), $\gamma^2 = -10^5$ (bottom).

The field's mass impacts significantly the inspiral dynamics and the phenomenology of the emitted GWs. These are plotted in Figure 4.6. Contrary to the results of section 4.4.2, the $\gamma^2 > 0$ field yields now the longest inspiral time, while $\gamma^2 = 0$ and $\gamma^2 < 0$ merge at the same time.

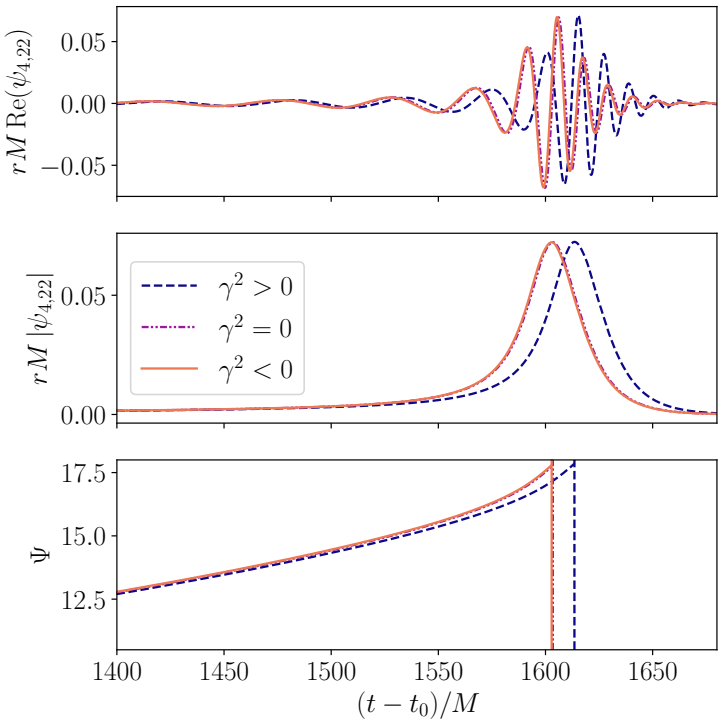

Figure 4.6: GW emission of an equal-mass BBH for $\mu M = 0.6$. The top panel shows the real part of the (2,2) mode of the Weyl scalar ψ_4 extracted at $r = 50M$, while the middle panel plots its absolute value. The bottom panel shows the accumulated orbital phase Ψ.

This result demonstrates the importance of self-interactions and non-standard kinetic term on the field dynamics and its impacts on a BBH evolution. Recent work [23] showed that for a binary with a non-interacting massive scalar field, the dephasing is maximised when the Compton wavelength is comparable to the initial orbital separation $\lambda_C \sim d$. For the sigma model with positive curvature, this does not hold true: Figure 4.7 compares the GW emitted by the binary

with the two choices of field's masses. The heavier field corresponds to a longer inspiral phase.

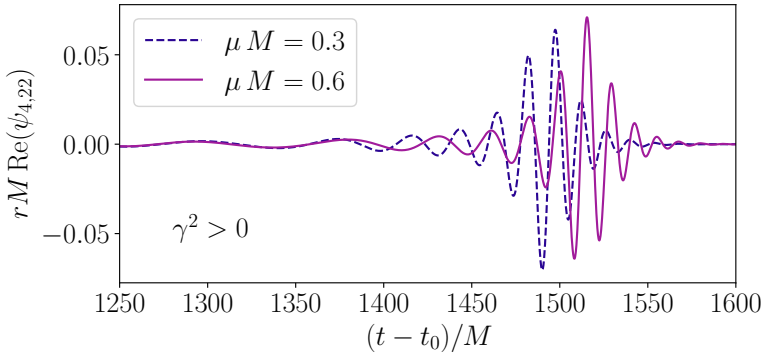

Figure 4.7: Real part of the (2,2) mode of the Weyl scalar for $\mu M = 0.3$ (dashed line) and $\mu M = 0.6$ (continuous line) with $\gamma^2 = 10^5$. The binary interacting with heavier field merges at a later time.

The complex structure and density distribution of the scalar cloud can therefore exert a radial pull on the binary components, competing with dynamical friction in driving the inspiral. We can test this idea by computing the scalar field total mass in the outer region of the system, i.e. for $r > r_{BHs}$ with r_{BHs} the distance of the binary components from the centre of mass, namely $r_{BHs} = \sqrt{r_1^2 + r_2^2}$, where r_i is the distance of every black hole from the centre of mass. We estimate the mass via the volume integral

$$m_\Phi = -\int_{\mathcal{V}} \mathrm{d}^3\mathrm{x}\,\sqrt{\bar{\gamma}}\,\mathrm{T}^0_0 \sim \int_{\mathcal{V}} \mathrm{d}^3\mathrm{x}\,\sqrt{\bar{\gamma}}\,\alpha\,\rho\,, \tag{4.40}$$

in an analogous way as in [25], where $\bar{\gamma}$ is the determinant of the spatial metric. In Figure 4.8 we plot the resulting mass as a function of the inspiral time for the considered masses and sigma models. In both lighter and heavier cases, the curve with higher mass in the late part of the inspiral merges last. The additional mass distributed around the binary because of the non-trivial kinetic and potential terms is therefore an important driver of the inspiral physics, together with dynamical friction. This is similar to the gravitational torque exerted by a protoplanetary disk on forming planets, that are then driven to migrate to different orbits. A comparison with this scenario is however difficult, as the physics of a gaseous circumstellar disk is driven by magneto-hydrodynamics and it is substantially more complex than the purely gravitational interactions

described here. A more thorough analysis of the torques acting on the inspiraling BHs as a function of the field's mass would anyway be insightful to clarify the source of the total dephasing.

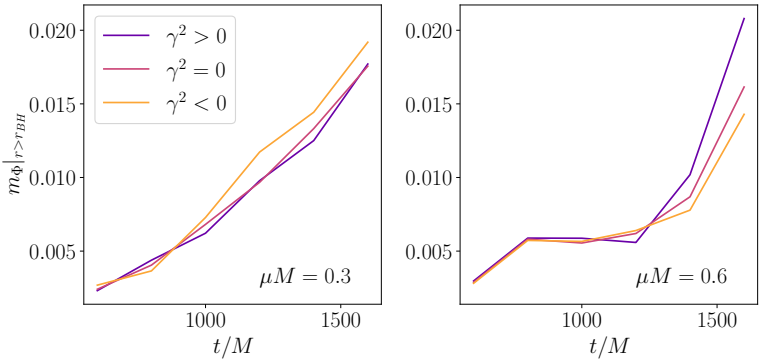

Figure 4.8: Integrated scalar field mass m_Φ in the region $r_{BHs} < r < 100M$ plotted as a function of the inspiral time for $\mu M = 0.3$ (left) and $\mu M = 0.6$ (right), as well as for the chosen scalar manifold curvatures.

In the BBH simulations we use a time step given by $dt_{\text{multiplier}} = 0.25$, which is likely to introduce some errors in resolving the scalar field oscillations at the coarsest level. This value was used to keep the simulations running in the available computing time. We estimate that this limitation does not hinder significantly the results, as the code converges properly as discussed in appendix C.4.

Ringdown phase

The frequency content of the ringdown stage is of key importance to perform high-precision tests of the Kerr hypothesis [106, 99] and can receive corrections from beyond-GR extensions [191, 65, 190, 78]. In Figure 4.9 we plot the absolute value of $\psi_{4,22}$ with $\mu M = 0.3$ and varying γ^2. In order to study the impact of the sigma models on the quasi-normal modes (QNMs) of the simulated binaries, we align the emitted waveforms at merger and fit an exponentially damped oscillating function to the $l = 2, m = 2$ component of ψ_4,

$$\psi_{4,22} = C + A\, e^{-w_1\, t} \cos(w_2\, t + B). \tag{4.41}$$

We perform the fit starting from $t - t_{merger} \sim 30M$, so to avoid the non-linear contributions from the merger, up to $t - t_{merger} \sim 70M$. For all choices of μM

and γ^2, we obtain frequencies consistent with

$$(\omega_R = 0.542 \pm 0.002,\, \omega_I = -0.083 \pm 0.001)\,, \tag{4.42}$$

with the uncertainties coming from fits on simulations with different resolutions, as discussed in Appendix C.4. We can compare those values with the analytical (2,2) mode of a Kerr vacuum BH with dimensionless spin $\chi = 0.69$, which is the final state of our simulations. The fitted QNMs differ from the reference value $\omega_{22}^{Kerr} = 0.527 - 0.081\,i$ [39] of $\sim 2\%$. The parameters explored with our simulations are thus insufficient to draw any conclusions about possible corrections to the QNM frequencies due to the sigma model curvature.

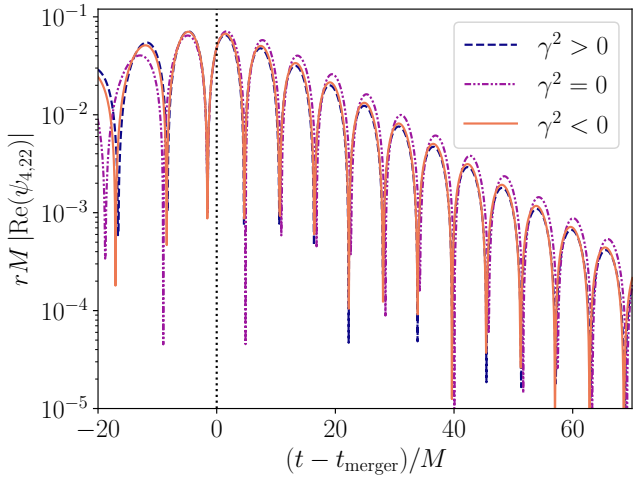

Figure 4.9: Merger and ringdown phases for a BBH with scalar field of $\mu M = 0.3$ and different γ^2. We align the GWs at the maximal amplitude. The Weyl scalar is extracted at $r_{ex} = 50M$.

In Figure 4.10 we plot the norm of the real part of the (2,2) mode of the Weyl scalar for $\mu M = 0.3$ and $\gamma^2 = 0$ at two different extraction radii, $r_{ext} = (50M, 100M)$. We plot the GW against the retarded time. The curves superimpose, showing that the tensor modes propagate with speed 1 on the simulation grid.

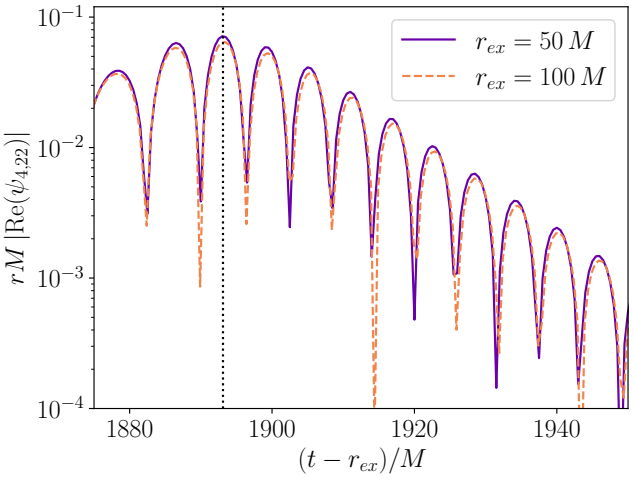

Figure 4.10: Waveform of a BBH merger with scalar field of $\mu M = 0.3$ and $\gamma^2 = 0$ extracted at different radii as a function of $t - r_{ex}$. The waveforms align, showing no velocity dispersion in the gravitational radiation.

Scalar emission

We characterise the scalar field dynamics extracting the scalar field value at several radii from the BBH centre of mass and projecting it on spherical harmonics. We focus our discussion on the behaviour of the $l = 2, m = 2$ mode, as it is the dominant one sourced by the quadrupolar GW emission. We also observe an oscillating $l = 0, m = 0$ mode, which contributes to the monopolar accretion on the binary and it is long-lived after the merger, as the field keeps accreting on the remnant. The massive nature of the field makes its propagation non-trivial [24]. In Figure 4.11 we plot the real part of the $(2, 2)$ mode of the complex scalar field Φ extracted at $r_{ex} = 50M$. The field oscillates rapidly during the inspiral.

The field exhibits a varying maximal amplitude that grows at first, before tapering down and transitioning to a short exponentially damped ringdown. In Figure 4.12 we plot the field's absolute value for the different choices of γ^2. As already shown by the energy-density distributions, the scalar amplitude is strongly dependent on the field interactions.

Moreover, the field mass introduces a translation into a frequency-dependent propagation velocity for the modes making up the emission. In Figure 4.13 the

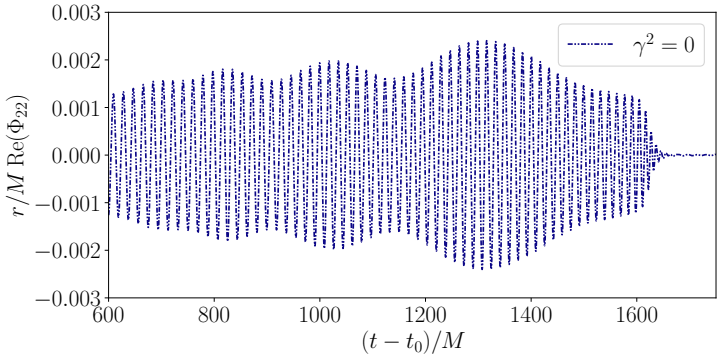

Figure 4.11: Scalar radiation from the $l = 2$, $m = 2$ mode with $\mu M = 0.3$ and $\gamma^2 = 0$. The field shows a time-dependent maximal amplitude.

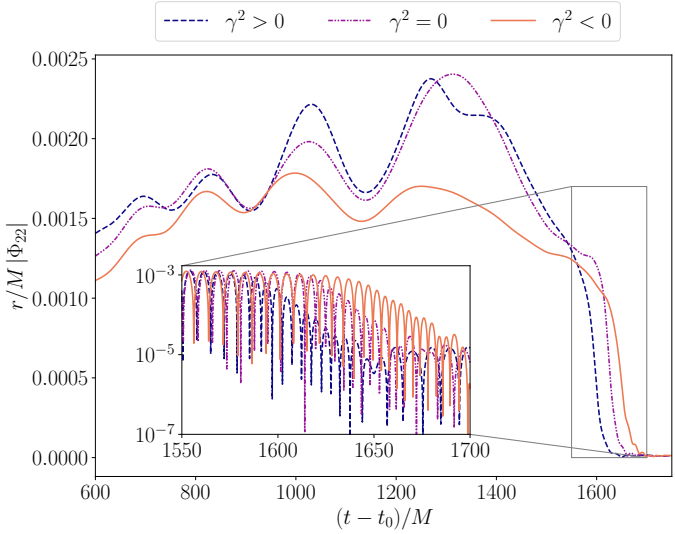

Figure 4.12: Absolute value of Φ_{22} for different values of γ^2. The inset plots the absolute value of $\mathrm{Re}(\Phi_{22})$ around the time of merger.

scalar waves are extracted at different radii and plotted as a function of the retarded time. The curves do not match, as different frequencies components propagate at different speeds.

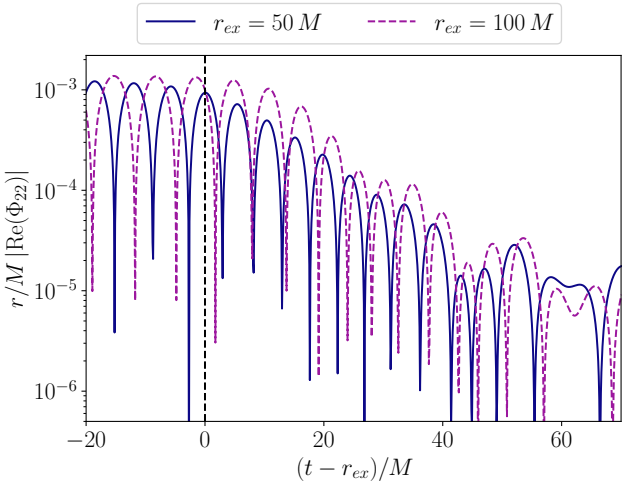

Figure 4.13: Scalar waveform of the $(2, 2)$ mode at extraction radii $r_{ex} = 50M$ and $r_{ex} = 100M$. We plot the results for $\gamma^2 = 0$.

Besides the scalar waves emission in the ringdown phase, it would also be instructive to consider the scalar field's density profile after merger. Unfortunately, we stopped the numerical simulations shortly after the coalescence into a final single BH in the majority of cases presented above, in order to save computational resources. In the heavier field case, i.e. $\mu M = 0.6$, we let the simulations run up to $t = 2400\,M$. We plot the resulting density distributions for the different scalar manifold curvatures on Figure 4.14. In the attractive case $\gamma^2 > 0$, we observe first a decrease in density, followed by a growth of the density profile in the vicinity of the BH remnant, which suggest the onset of the usual accretion process studied in section 4.4.1. However, this phenomenon is not observed for $\gamma^2 = 0$ or $\gamma^2 < 0$. These cases show a decreasing value of the density over the short simulation timescale. This might be due by some residual dissipation of excited field states after the merger, with a longer time window before the start of the standard field accretion. However, to draw any significant conclusion, one should perform longer simulations. These would help clarify the fate of the bosonic cloud after an inspiral and could shine light on the behaviour of such cloud in the event on hierarchical mergers.

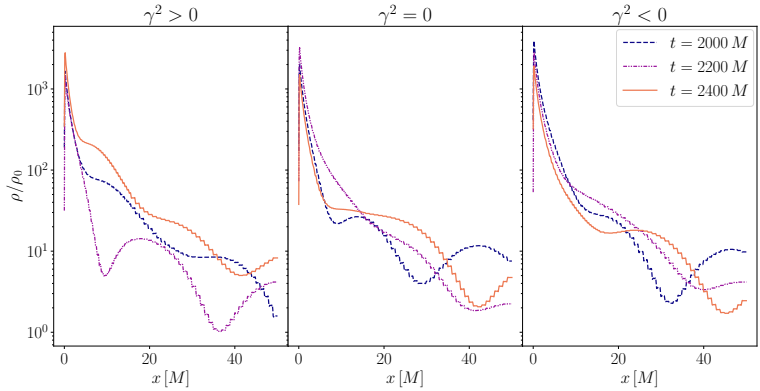

Figure 4.14: Density profiles after merger for $\mu M = 0.6$ and different values of γ^2.

4.5 Summary and discussion

In this work, we numerically studied the dynamics of the 2-dimensional maximally symmetric sigma models $\mathrm{SL}(2,\mathbb{R})$ and $\mathrm{O}(3)$. We evolved the theories' equations of motion in the code `GRChombo`, starting from constraints-obeying initial data obtained from `GRTresna`. We characterised the accretion of a uniform scalar field onto a non-rotating BH. For light values of the field mass, the $\mathrm{SL}(2,\mathbb{R})$ model exhibits attractive self-interaction with respect to a non-interacting massive field, with a larger and more compact over-density. The $\mathrm{O}(3)$ instead shows a repulsive behaviour. For larger values of the field mass, however, the mass term in the potential dominates over the self-interactions and the accretion is independent of the sigma model curvature. Our simulations show that scalar fields from sigma models can grow clouds from accretion over short timescales. The final state of such halos depends on the sigma model curvature as well as on the field mass.

We evolved an equal-mass binary BH inspiral for ~ 10 orbits, with different scalar manifold's curvatures and field mass, starting with the same initial separation and momenta for the BHs and background scalar field density. When the field Compton wavelength is larger than the initial BH separation, the field grows a circumbinary cloud during the inspiral. The cloud is more compact for the $\mathrm{SL}(2,\mathbb{R})$ model while it is more diffused in the $\mathrm{O}(3)$ case. The matter distribution effect on the binary results in a dephased GW emission. The $\mathrm{SL}(2,\mathbb{R})$ model extracts more energy from the BBH, which then merges earlier than in the non-interacting case. The $\mathrm{O}(3)$ model yields a longer inspiral

than in the non-interacting case. A summary of these results is displayed in Table 4.1, as a function of the theory's parameters. This is provisional, as the parameter space was not explored extensively to minimize computational costs while capturing the phenomenology.

	$\mathrm{SL}(2,\mathbb{R})$ ($\gamma^2 > 0$)	O(3) ($\gamma^2 < 0$)
Isolated BH		
$\mu M = 0.1$	Attractive SI	Repulsive SI
$\mu M = 1$	No difference	No difference
BBH		
$\mu M = 0.3$	Early merger	Delayed merger
$\mu M = 0.6$	Delayed merger	No difference

Table 4.1: Summary of simulation outcomes as a function of the scalar field mass and target manifold curvature. SI stands for self-interaction. The outcomes are compared to a non-interacting scalar field ($\gamma = 0$) of the same mass.

We therefore show the relevance of the non-trivial kinetic term for the field's phenomenology in astrophysical environments. Expanding the potential term at first order in γ^2 is equivalent to a $\lambda/4|\Phi|^4$ self-interaction potential with $\lambda = \mu^2\gamma^2/2$. However, contrary to the results given in [25], with $\lambda < 0$ inducing attractive self-interactions, here it is the $\gamma^2 > 0$ case to exhibit such behaviour. We also point out that we do not observe a cloud disruption from *bosenova* explosion, as reported in [25] in the attractive case. This result suggests that the curvature dependence of the kinetic term suppresses the *bosenova* onset. A direct comparison with the parameters and result of [25] is spoiled by the dependence on γ^2 of our kinetic term. More simulations with strong attractive self-interaction are therefore needed to better understand such phenomenon.

Our results are consistent with the conclusions of [66] characterising the soliton solutions of (4.35). The O(3) would support heavy and compact boson stars, while the $\mathrm{SL}(2,\mathbb{R})$ case would lead to light and diffuse stars. Scalar fields with a standard kinetic term and repulsive self-interactions have been shown to produce boson stars with large maximal mass, of order $\sqrt{\lambda}M_P^3/\mu^2$, with M_P the Planck mass, while attractive self-interactions would produce significantly lighter stars, with maximal masses of order $M_P/\sqrt{|\lambda|}$ [102, 220]. In our numerical simulations, the O(3) ($\mathrm{SL}(2,\mathbb{R})$) model displays again a repulsive (attractive) self-interaction phenomenology.

When thinking of the scalar field we simulate as a DM constituent, its physical mass $m = \hbar\mu/c$ is effectively unconstrained over a large domain by cosmological and astrophysical observations, with a lower bound at $m \sim 10^{-21}$ eV [135]. The scalar's self-interactions, however, are constrained by dwarf galaxies and early universe dynamics [155, 95]. The dimensionless self-interaction coupling is constrained as $\lambda \lesssim (m/\text{eV})^4$. For the mass used in our simulations,

$$\mu \sim 0.5M \Rightarrow m \sim 8 \cdot 10^{-17} \left(\frac{M}{10^6 M_\odot}\right)^{-1} \text{eV}, \tag{4.43}$$

this translates to a bound of

$$\lambda \lesssim 10^{-65} \left(\frac{M}{10^6 M_\odot}\right)^{-4}. \tag{4.44}$$

Then, for $|\gamma^2| = 10^5$ we get

$$\lambda = \frac{\mu^2\gamma^2}{2} \sim 7 \cdot 10^{-79} \left(\frac{M}{10^6 M_\odot}\right)^{-2}, \tag{4.45}$$

which is below the constrained values for astrophysical BH masses. The parameter γ in the sigma models is related to the dimensionful energy scale of the scalar manifold E as

$$|\gamma| = \frac{M_P}{\sqrt{16\pi}E}, \tag{4.46}$$

with M_P the Planck mass. It is natural to consider $E \ll M_P$, so that γ can be large.

This work is a first step in understanding the phenomenology of matter fields from sigma models in an astrophysical scenario. Further investigations are, however, needed to first of all explore the theory parameter space, to gain a better understanding of the dependence of GW observables on the matter sector properties. Similarly, we leave for future work to assess the detectability of such environmental effects. For instance, the dephasing of the signal induced by matter distributions could lead to biases in parameter estimation when matched to vacuum GR templates [202, 93].

Chapter 5

Conclusion

5.1 Summary of main results

The existence of dark matter is corroborated by an outstanding amount of astrophysical observations, but a complete understanding of its properties at small scales, as well as its fundamental composition remain long-standing open questions. Gravitational waves detections are opening a rich new window on the gravitational universe, uncovering an ever-growing population of merging black holes and neutron stars and paving the way to high-precision tests of General Relativity. It has been argued that such signals can carry precious fingerprints of DM physics, when GW sources evolve in a region where the DM grows some relevant overdensity. This thesis has explored two scenarios in which DM candidates with a different microphysics can interact with a black hole spacetime and induce signatures on its GW emission.

In chapter 2 we discussed a fluid-like DM model, typically arising from heavier candidate particles in the allowed mass spectrum. We derived a relativistic density profile around a Schwarzschild BH, starting from an initial galactic-like Hernquist profile and performing an adiabatic contraction of the particles distribution under the assumption that the central BH grows on a long timescale. The result is an effective DM spike model showing an enhanced central density with respect to the original profile and decaying sharply at the marginally bound circular orbit radius. We checked that the spacetime is well-behaved asymptotically, that the spacetime mass is finite and the energy conditions are satisfied. This model is being currently discussed in the literature and its imprint on GW sources evaluated [210, 211, 45]. A rotating spike model has

also been proposed [180].

We applied BH perturbation theory to this geometry and derived the perturbed Einstein equations for such dressed BH. We highlighted a freedom in setting some perturbed fluid elements to zero, giving rise to two distinct perturbation choices. Such choice leads to different master equations, which signals how attention should be paid to modelling the fluid's response to perturbations. We stress that one should be consistent with the perturbation scheme when studying different aspects of the first-order phenomenology. We then obtained a master equation for the axial sector of perturbations, closely related to the Regge-Wheeler equation in a Schwarzschild spacetime, and a master system of coupled equations between metric and matter perturbations in the polar sector, which reduces to the Zerilli equation in the absence of DM. From there, we obtained the quasi-normal modes for the axial sector and compared them to some non-relativistic distribution of matter discussed previously in the literature. We observe that the QNM frequencies pick up a correction with respect to the vacuum values. The corrections scale polynomially in a combination of halo's parameters, with a different power than in the non-relativistic case. Furthermore, the corrections are weighted by a factor of the halo's total mass, which tends to suppress the corrections for more massive and dilute halos. Similar works have been carried out in this direction, computing the QNM shits from matter distributions [190, 67] and addressing their detectability prospects [212].

When a static external gravitational field perturbs the Schwarzschild-Hernquist spacetime, this responds being tidally deformed. We computed the linear response coefficients, the tidal Love numbers, in both the axial and polar sectors. We developed a robust numerical scheme to obtain the TLNs and found agreement in the non-relativistic halo case. We show that the choice of perturbation scheme affects the TLNs, with relative differences of $\mathcal{O}(1)$ in the appropriate expansion parameter around vacuum GR. We show that the TLNs are again smaller in the relativistic halo with respect to the non-relativistic one and they differ in sign between parity sectors.

In chapter 3 we turned our attention to lighter DM candidates described in terms of field theory. We introduced a class of massive scalar fields with a kinetic term promoted to a nonlinear sigma model. We considered two-dimensional maximally symmetric sigma models, the hyperbolic scalar manifold with negative curvature and $\mathrm{SL}(2,\mathbb{R})$ symmetry group, as well as the spherical scalar manifold, with positive curvature and $\mathrm{O}(3)$ symmetry. We wrote both theories in a unified form, introducing a single complex scalar field and a free parameter proportional to negative the target space curvature.

Before considering possible effects of such theories on GW sources, we studied simple spherically symmetric solutions. We coupled the scalar fields minimally

to gravity and solved the Einstein field equations with a spherically symmetric ansatz, regular boundary conditions at the origin and asymptotic flatness. We identify solutions corresponding to bound states of the Klein-Gordon equation and compute their mass, radius and charge. We interpret these solutions as self-gravitating bosonic condensates, usually known as boson stars. This work characterises a straightforward phenomenological aspect of these theories, which is however important in the exploration of exotic compact objects and BH mimickers [171, 121, 72].

We characterized the properties of such boson star solutions as a function of the target space curvature. We showed that the sigma model curvature has a strong impact on the theory's phenomenology. O(3) stars can have masses in the order of the neutron star mass and can reach small compactness, up to $R \sim 3.3M$. On the other hand, $\mathrm{SL}(2,\mathbb{R})$ stars are lighter objects and with high compactness, i.e. they are diluted objects. We comment on the allowed mass range of the scalar fields and found that O(3) stars would have an astrophysically relevant size for a wide range of particle masses, while $\mathrm{SL}(2,\mathbb{R})$ stars would be of astrophysical scale only for ultralight particles.

After studying self-gravitating solutions to the theory, we proceeded in chapter 4 to numerically simulate scalar fields from nonlinear sigma models on isolated BH and binary BH spacetimes. We implemented the Einstein-Klein-Gordon system in the numerical relativity code `GRChombo` and in the initial values solver `GRTresna`.

Starting from an initial uniform scalar field distribution, we simulated the scalar accretion onto an isolated Schwarzschild BH and discussed its dependence on the field's mass. We compared a light scalar, of mass parameter $\mu M = 0.1$, and a heavier one, $\mu M = 1$. In the lighter case, the $\mathrm{SL}(2,\mathbb{R})$ model behaves like an attractive self-interacting field, producing a denser and more compact density distribution in the vicinity of the BH, while the O(3) model shows a repulsive self-interaction, with lower densities at the horizon and a dispersed density profile. For heavier scalar fields, the mass term dominates, and the accretion profiles become independent of the sigma model curvature.

Starting again from a uniform scalar field density, we simulated the last few orbits of an equal mass binary BH. We chose mass parameters giving a field's Compton wavelength comparable to the initial binary separation ($\mu M = 0.3$) and twice as large ($\mu M = 0.6$). In the lighter field case, both sigma models produce a cloud that encompasses the binary and survives the inspiral. The $\mathrm{SL}(2,\mathbb{R})$ model forms a more compact density distribution, which drives the inspiral through dynamical friction and leads to an earlier merger with respect to, in order, a reference non-interacting massive scalar, and the O(3) model, for which the cloud is more diffused. For the heavier mass, the $\mathrm{SL}(2,\mathbb{R})$ sigma model

counter-intuitively yields the longest inspiral. This suggests that the kinetic terms play a complex role in the dynamics and that the binary is subjected to non-trivial torques from the matter distribution. We observe no significant difference of the dephasing between the non-interacting reference case and the O(3) model. We commented on the ringdown frequencies of the remnant, for which we find no significant deviations from the Kerr spacetime in the explored parameter space. This work explores the possibility to perform full-fledged numerical simulations of DM environments motivated by high-energy Physics. It connects to the efforts of the `GRChombo` collaboration to study exotic GW sources in NR [83, 28, 25].

5.2 Outlook and future directions

This thesis focussed on studying the effects of model-specific environments onto GW sources. The results discussed in the previous chapters show that DM can indeed imprint significant signatures in the emission of GW and they add to the extensive work carried out in the last years to characterize them. GW are likely to be a promising channel for probing DM environments and exotic compact objects. Most dense environments of GW sources cause a dephasing of the inspiral phase, while inducing non-zero tidal deformability and characteristic shifts of the quasi-normal ringdown frequencies.

While this program is crucial to better understand the properties of interesting DM candidates in astrophysical systems and in the strong gravity regime, it does not face the important question of assessing the detectability of environmental effects. Recent results have discussed the chances of distinguishing an environment from vacuum GR with GW data, taking into account the environment's imprints in different phases of a compact binary coalescence separately. The shifts in quasi-normal modes induced by a DM halo have proven to be challenging to detect, even with the expected data from the next-generation GW experiments [212], while dephasing from the inspiral phase could help discerning between different environments [84] but it might still be plagued by degeneracies with vacuum GR parameters [202].

Thus, future research should produce waveform models combining information from all components of a coalescence, as well as including several effects on single pieces of the dynamics, like dynamical friction and tidal deformability in the inspiral. This would test the chance of enhancing detectability and breaking of parameters degeneracies with the global effects induced by a non-vacuum environment. Model-specific studies are key to understanding the order-of-magnitude scale of the environments' imprints and are suitable to develop a

self-consistent, relativistic model of the environment-GW binaries interactions. Moreover, this line of research is fundamental in identifying possible smoking-gun effects that can help reaching stronger evidence for the presence of an environment. However, model-agnostic pipelines including correlated deviations from vacuum-GR in the totality of the GW signal should also be developed, given the wide variety of candidate models and possible astrophysical environments that can affect the signals.

Efforts should as well go into understanding the formation channels and population characteristics of a dense DM environment around BHs and BH binaries. This will help defining the expected rates at which such environments would be relevant, and identifying the most affected GW sources. For example, recent developments suggested that adiabatic DM spikes could form in the early universe [45], which constitutes a plausible astrophysical formation channel for objects which existence was intensely debated in the literature. This should be combined with high-precision numerical simulations integrating a careful treatment of the matter dynamics, to evaluate the consequences of a binary mergers history on an environment [140]. The development of simulations handling the interactions of a multi-components environment, i.e. DM and baryonic matter obeying hydrodynamics coupled to gravity, can help in reaching a more complete understanding of these systems.

With the development of more accurate waveform models, attention should be directed to the implementation of detection and parameter estimation data analysis pipelines accounting for environmental perturbations to vacuum GR signals. Given the small size of the effect on single sources, stacking methods could be interesting to combine multiple events and gain statistical insight on common environments. In this context, some machine learning methods could be explored, to enhance the chance of detecting unmodeled signatures of an environment or of new physics [89]. Machine learning based interpolation could also be useful in efficiently generating waveforms over a wide range of parameters for environments for which accurate waveforms are computationally costly and obtained over a small set of parameters.

Through this work we showed how environmental effects, of different types and phenomenology, can play a significant role in the emission of GW from compact objects binaries. While current detectors are likely not affected by the effects discussed before, future observatories like LISA and ET will allow new probes of fundamental physics, DM environments and exotic compact objects. Further theoretical, numerical, and data analysis advancements are essential to fully exploit the rich phenomenology of these systems and uncover new physics beyond the Standard Model and General Relativity.

Appendix A

Additional material related to chapter 2

A.1 The perturbation equations in vacuum Einstein gravity

Let us now work out the case of polar gravitational perturbation in the context of vacuum Einstein gravity. In this case, the perturbed vacuum Einstein's equations become, $\delta G_{\mu\nu} = 0 = \delta R_{\mu\nu}$. we obtain, $H_0 = H_2 \equiv H(r)$. With this choice, the following differential equations can be obtained for the perturbations associated with the vacuum Einstein gravity,

$$K' + \left(\frac{r-3M}{r(r-2M)}\right) K - \frac{1}{r} H + \left(\frac{\ell(\ell+1)}{2i\omega r^2}\right) H_1 = 0 \ , \tag{A.1}$$

$$H_1' + \left(\frac{2M}{r(r-2M)}\right) H_1 + \frac{i\omega r}{r-2M} K + \frac{i\omega r}{r-2M} H = 0 \ , \tag{A.2}$$

$$H' + \left(\frac{r-3M}{r(r-2M)}\right) K + \left[\frac{i\omega r}{r-2M} + \frac{\ell(\ell+1)}{2i\omega r^2}\right] H_1 - \frac{r-4M}{r(r-2M)} H = 0 \ . \tag{A.3}$$

In addition, we have the following algebraic relation between these three perturbation quantities,

$$\left[\frac{2M(r-3M)}{r(r-2M)}-\frac{2\omega^2r^3}{r-2M}+(\ell-1)(\ell+2)\right]K + \left[2i\omega r+\frac{\ell(\ell+1)M}{i\omega r^2}\right]H_1-\left[\frac{6M}{r}+(\ell+2)(\ell-1)\right]H=0\ . \tag{A.4}$$

However, we have two additional equations,

$$K''+\left(\frac{3r-5M}{r(r-2M)}\right)K'-\frac{(\ell-1)(\ell+2)}{2r(r-2M)}K-\frac{1}{r}H'-\left(\frac{\ell(\ell+1)+2}{2r(r-2M)}\right)H=0\ , \tag{A.5}$$

$$K''-H''+\left[\frac{2(r-M)}{r(r-2M)}\right]K'-\left[\frac{2r}{r(r-2M)}\right]H' + \left(\frac{\omega^2r^2}{(r-2M)^2}\right)H+\left(\frac{\omega^2r^2}{(r-2M)^2}\right)K-\left(\frac{2i\omega r}{r-2M}\right)H_1'-\left[\frac{2i\omega(r-M)}{(r-2M)^2}\right]H_1=0\ . \tag{A.6}$$

The first equation from the above set can be derived in the following manner — (a) one first takes a derivative of Eq. (A.1), (b) then H_1' is replaced in terms of other perturbation quantities, using Eq. (A.2), (c) and finally one uses Eq. (A.1) to replace any remaining H_1. The derivation of Eq. (A.6) follows the following route: (i) subtracting Eq. (A.3) from Eq. (A.1), (ii) taking a derivative of the resulting expression, (iii) adding to it, the difference between Eq. (A.1) and Eq. (A.3), multiplied by $\{2(r-M)/r(r-2M)\}$ and finally (iv) using the expression for H_1' from Eq. (A.2). Thus, neither Eq. (A.5), nor Eq. (A.6) are independent equations. In particular, given Eq. (A.4), along with any two of the three equations from Eq. (A.1) to Eq. (A.3), the other can be derived.

Let us now try to derive the master equation. For that purpose, let us solve for $H(r)$ from Eq. (A.4) and then substitute the same in the differential equations for K, in Eq. (A.1), yielding,

$$K'+\left(\frac{r-3M}{r(r-2M)}\right)K+\left(\frac{\gamma_\ell+2}{2i\omega r^2}\right)H_1 - \frac{1}{(6M+\gamma_\ell r)}\left[\left(\frac{2M(r-3M)+r(r-2M)\gamma_\ell-2\omega^2r^4}{r(r-2M)}\right)K\right.$$

$$+\left(\frac{-2\omega^2 r^3+(\gamma_\ell+2)\,M}{i\omega r^2}\right)H_1\Bigg]=0\ . \tag{A.7}$$

where, we have defined $\gamma_\ell = (\ell+2)(\ell-1)$. Further simplification and rearrangement of the terms yield,

$$K'=\left[\alpha_0(r)+\alpha_2(r)\omega^2\right]K+\left[\beta_0(r)+\beta_2(r)\omega^2\right]\left(\frac{H_1}{\omega}\right), \tag{A.8}$$

with the following definitions for the known functions $\alpha_0(r)$, $\alpha_2(r)$, $\beta_0(r)$ and $\beta_2(r)$, respectively, as,

$$\alpha_0\equiv-\frac{-\gamma_\ell Mr+4M(r-3M)}{r\,(6M+\gamma_\ell r)\,(r-2M)}\ ,\qquad \alpha_2\equiv-\frac{2r^3}{(6M+\gamma_\ell r)\,(r-2M)}\ , \tag{A.9}$$

$$\beta_0\equiv-\frac{(\gamma_\ell+2)\,(4M+\gamma_\ell r)}{2ir^2\,(6M+\gamma_\ell r)}\ ,\qquad \beta_2\equiv\frac{2ir}{(6M+\gamma_\ell r)}\ . \tag{A.10}$$

On the other hand, the differential equation for H_1, as in Eq. (A.2), becomes,

$$\begin{aligned}H_1'&+\left(\frac{2M}{r(r-2M)}\right)H_1+\frac{i\omega r}{r-2M}K\\&+\frac{i\omega r^2}{(r-2M)\,(6M+\gamma_\ell r)}\Bigg[\left(\frac{2M(r-3M)+r(r-2M)\gamma_\ell-2\omega^2r^4}{r(r-2M)}\right)K\\&+\left(\frac{-2\omega^2r^3+(\gamma_\ell+2)\,M}{i\omega r^2}\right)H_1\Bigg]=0\ .\end{aligned} \tag{A.11}$$

This can also be expressed as,

$$\frac{H_1'}{\omega}=\left[\kappa_0(r)+\kappa_2(r)\omega^2\right]K+\left[\delta_0(r)+\delta_2(r)\omega^2\right]\left(\frac{H_1}{\omega}\right) \tag{A.12}$$

where, the coefficients κ_0, κ_2, δ_0 and δ_2 becomes,

$$\kappa_0\equiv-\frac{ir\left\{2\,(r-2M)\,(3M+\gamma_\ell r)+2M(r-3M)\right\}}{(r-2M)^2\,(6M+\gamma_\ell r)}\ , \tag{A.13}$$

$$\kappa_2\equiv\frac{2ir^5}{(r-2M)^2\,(6M+\gamma_\ell r)}\ , \tag{A.14}$$

$$\delta_0\equiv-\frac{2M\,(6M+\gamma_\ell r)+(\gamma_\ell+2)\,Mr}{r\,(r-2M)\,(6M+\gamma_\ell r)}\ , \tag{A.15}$$

$$\delta_2 \equiv \frac{2r^3}{(r-2M)\,(6M+\gamma_\ell r)} \ . \tag{A.16}$$

Let us introduce a new function $\Psi_{\rm Z}$, such that,

$$K = \alpha(r)\Psi_{\rm Z} + \beta(r)\frac{d\Psi_{\rm Z}}{dr_*} \ ; \tag{A.17}$$

$$\frac{H_1}{\omega} = \kappa(r)\Psi_{\rm Z} + \delta(r)\frac{d\Psi_{\rm Z}}{dr_*} \ . \tag{A.18}$$

where, the tortoise coordinate r_* is defined as, $(dr/dr_*) = (r-2M)/r$. Further, we demand,

$$\frac{d^2\Psi_{\rm Z}}{dr_*^2} = \left[V_{\rm Z} - \omega^2\right]\Psi_{\rm Z} \ . \tag{A.19}$$

Then, taking derivative of Eq. (A.17) with respect to the radial coordinate, we obtain,

$$\begin{aligned} K' &= \alpha'\Psi_{\rm Z} + \left[\beta' + \alpha\left(\frac{r}{r-2M}\right)\right]\frac{d\Psi_{\rm Z}}{dr_*} + \beta\left(\frac{r}{r-2M}\right)\frac{d^2\Psi_{\rm Z}}{dr_*^2} \\ &= \left[\alpha' + \beta\left(\frac{r}{r-2M}\right)\left(V_{\rm Z}-\omega^2\right)\right]\Psi_{\rm Z} \\ &+ \left[\beta' + \alpha\left(\frac{r}{r-2M}\right)\right]\frac{d\Psi_{\rm Z}}{dr_*}. \end{aligned} \tag{A.20}$$

While from Eq. (A.8), and then using Eqs. (A.17) and (A.20), we obtain,

$$\begin{aligned} K' &= \left[\alpha_0 + \alpha_2\omega^2\right]\left(\alpha\Psi_{\rm Z} + \beta\frac{d\Psi_{\rm Z}}{dr_*}\right) + \left[\beta_0 + \beta_2\omega^2\right]\left(\kappa\Psi_{\rm Z} + \delta\frac{d\Psi_{\rm Z}}{dr_*}\right) \\ &= \left[\alpha\left(\alpha_0 + \alpha_2\omega^2\right) + \kappa\left(\beta_0 + \beta_2\omega^2\right)\right]\Psi_{\rm Z} \\ &+ \left[\beta\left(\alpha_0 + \alpha_2\omega^2\right) + \delta\left(\beta_0 + \beta_2\omega^2\right)\right]\frac{d\Psi_{\rm Z}}{dr_*}. \end{aligned} \tag{A.21}$$

Comparing this with Eq. (A.20), we finally obtain,

$$\alpha\left(\alpha_0 + \alpha_2\omega^2\right) + \kappa\left(\beta_0 + \beta_2\omega^2\right) = \alpha' + \beta\left(\frac{r}{r-2M}\right)\left(V_{\rm Z} - \omega^2\right), \tag{A.22}$$

$$\beta\left(\alpha_0 + \alpha_2\omega^2\right) + \delta\left(\beta_0 + \beta_2\omega^2\right) = \beta' + \alpha\left(\frac{r}{r-2M}\right). \tag{A.23}$$

Thus equating coefficients of ω^2 and terms independent of ω, on both sides of the above expressions, we obtain,

$$\beta\alpha_2 + \delta\beta_2 = 0, \tag{A.24}$$

$$\beta\alpha_0 + \delta\beta_0 = \beta' + \alpha\left(\frac{r}{r-2M}\right), \tag{A.25}$$

$$\alpha\alpha_0 + \kappa\beta_0 = \alpha' + \beta\left(\frac{r}{r-2M}\right)V_{\rm Z}, \tag{A.26}$$

$$\alpha\alpha_2 + \kappa\beta_2 = -\beta\left(\frac{r}{r-2M}\right). \tag{A.27}$$

Choosing $\beta = 1$, we get,

$$\delta = -\frac{\alpha_2}{\beta_2} = \frac{-ir^2}{r-2M}\ , \tag{A.28}$$

$$\alpha = \left(\frac{r-2M}{r}\right)(\alpha_0 + \delta\beta_0) = \frac{\gamma_\ell\left(\gamma_\ell+2\right)r^2 + 6\gamma_\ell M r + 24M^2}{2r^2\left(6M+\gamma_\ell r\right)}, \tag{A.29}$$

$$\kappa = \alpha\delta - \frac{1}{\beta_2}\left(\frac{r}{r-2M}\right) = i\left[\frac{-\gamma_\ell r^2 + 3\gamma_\ell M r + 6M^2}{\left(6M+\gamma_\ell r\right)\left(r-2M\right)}\right]. \tag{A.30}$$

Thus finally,

$$\begin{aligned} V_{\rm Z} &= \left(\frac{r-2M}{r}\right)\left[\alpha\alpha_0 + \kappa\beta_0 - \alpha'\right] \\ &= \left(\frac{r-2M}{r}\right)\left[\frac{\gamma_\ell^2\left(\gamma_\ell+2\right)r^3 + 6M\gamma_\ell^2 r^2 + 36M^2\gamma_\ell r + 72M^3}{r^3\left(6M+\gamma_\ell r\right)^2}\right]. \end{aligned} \tag{A.31}$$

This is the Zerilli potential, associated with polar perturbation of the Schwarzschild spacetime.

Appendix B

Additional material related to chapter 3

B.1 All two-dimensional sigma models with a $U(1)$ isometry

Without loss of generality, a two-dimensional nonlinear sigma model can always be written as

$$\mathcal{L} = -H(\tau, \bar{\tau})\partial_\mu \tau \partial^\mu \bar{\tau} - V(\tau, \bar{\tau})\,, \tag{B.1}$$

for a complex scalar τ and real functions $H(\tau, \bar{\tau})$ and $V(\tau, \bar{\tau})$. Now we look for theories with a global symmetry, so let us assume that this Lagrangian is invariant under a holomorphic isometry,

$$\tau' = f(\tau; \alpha)\,, \quad \bar{\tau}' = \bar{f}(\bar{\tau}; \alpha)\,, \tag{B.2}$$

where f is a certain holomorphic function and α is a real parameter labeling the transformation, such that $f(\tau; 0) = \tau$. In addition, we are interested in the case in which the symmetry group is U(1), so

$$f(\tau; \alpha + 2\pi) = f(\tau; \alpha)\,. \tag{B.3}$$

Let us introduce the generators of the symmetry

$$p = \left.\frac{\partial f}{\partial \tau}\right|_{\alpha=0}\,, \quad \bar{p} = \left.\frac{\partial \bar{f}}{\partial \bar{\tau}}\right|_{\alpha=0}\,. \tag{B.4}$$

Then, in order for the transformation (B.2) to be a symmetry, it follows that H and V must satisfy

$$\begin{aligned} \frac{\partial H}{\partial \tau} p + \frac{\partial H}{\partial \bar{\tau}} \bar{p} + H \left(\frac{\partial p}{\partial \tau} + \frac{\partial \bar{p}}{\partial \bar{\tau}} \right) = 0 \,, \\ \frac{\partial V}{\partial \tau} p + \frac{\partial V}{\partial \bar{\tau}} \bar{p} = 0 \,. \end{aligned} \tag{B.5}$$

Under these conditions there is a canonical way of writing the Lagrangian. The idea is to introduce a new field Φ which transforms as

$$\Phi' = e^{i\alpha} \Phi \,. \tag{B.6}$$

To find the appropriate change of variables $\Phi(\tau)$, we note that under an infinitesimal transformation we have

$$\delta_\alpha \Phi = \frac{d\Phi}{d\tau} \delta_\alpha \tau = \frac{d\Phi}{d\tau} p \,, \tag{B.7}$$

and hence demanding $\delta_\alpha \Phi = i\Phi$ leads to

$$\frac{d\Phi}{d\tau} p = i\Phi \,. \tag{B.8}$$

This is a differential equation from where we can obtain $\Phi(\tau)$ or the inverse relation $\tau(\Phi)$. It remains to study the form of the Lagrangian when expressed in terms of Φ. We have

$$\mathcal{L} = -K \partial_\mu \Phi \partial^\mu \bar{\Phi} - V \,, \tag{B.9}$$

where

$$K = \frac{|p|^2}{|\Phi|^2} H \,, \tag{B.10}$$

and V is the same as in (B.1), but expressed as a function of Φ. Then, using (B.5), it follows that

$$\Phi \frac{\partial K}{\partial \Phi} - \bar{\Phi} \frac{\partial K}{\partial \bar{\Phi}} = 0 \,, \quad \Phi \frac{\partial V}{\partial \Phi} - \bar{\Phi} \frac{\partial V}{\partial \bar{\Phi}} = 0 \,, \tag{B.11}$$

hence implying that these quantities only depend on Φ through its modulus, $K = K\left(|\Phi|^2\right)$, $V = V\left(|\Phi|^2\right)$, as it should be since by construction the transformation (B.6) should be a symmetry.

Therefore, in terms of the variable Φ, the Lagrangian reads

$$\mathcal{L} = -K\left(|\Phi|^2\right) \partial_\mu \Phi \partial^\mu \bar{\Phi} - V\left(|\Phi|^2\right) \,. \tag{B.12}$$

While it is obvious that all the theories of this type are invariant under U(1), it is nontrivial that all nonlinear sigma models with a holomorphic isometry can be expressed in this way.

B.2 Numerical methods

The system of differential equations (3.26), (3.25), (3.27) can be solved by direct integration after the conditions of regularity at the origin and asymptotic flatness are imposed. As discussed in the main text, initial conditions are set at $r_{in} = 10^{-3}$ via the expansions (3.31) and the solution is obtained up to a radius $r_{\max}$, where it diverges for a generic value of ω. However, infinitely supported solutions may exist for specific values of ω, for which the domain of integration rapidly grows. The goal of the numerical analysis is therefore to identify the peak in $r_{\max}$ corresponding to the resonant frequency of the boson star ground state. With reference to Fig. 3.1, this would be leftmost peak.

First of all, the solutions depend on the choice of the scalar field value at the origin ϕ_0. For each value of the parameter γ, there exist a maximum value of ϕ_0 after which the solutions have bounded $r_{\max}$ for every ω and asymptotically flat solutions are thus not allowed. As a first step, one needs to find this value $\phi^{\gamma}_{0,\max}$. This is done applying a binary search algorithm on a table of ϕ_0 values until $\phi^{\gamma}_{0,\max}$ is estimated with sufficient precision. Let us stress that this requires an inefficient search of the first resonant frequency for each value of the central field. This is because in order to assess the existence of resonant solutions, one needs to scan a wide interval of frequencies with a grid fine enough to correctly identify peaks in $r_{\max}$. Nevertheless, $\phi^{\gamma}_{0,\max}$ can be obtained at a reasonable precision with a low number of binary search iterations.

Once the value of the maximum central field is known for a given value of γ, we build a table of resonant frequencies for $\phi_0 \in [\phi_{0,\min} \sim 10^{-2}, \phi^{\gamma}_{0,\max}]$. It turns out that for small ϕ_0, the resonant frequency of the ground state is close to 1. We can therefore fix $\phi_{0,\min}$ and start scanning over the frequency from $\omega = 1$ (in units of $\mu = 1$) with a certain step $\Delta\omega$. We then identify the first peak with a hill climbing method. Once the value $r_{\max}$ decreases — meaning that we have passed the peak — we change the sign of the frequency step and refine the grid. This allows to rapidly converge to the left-most peak without having to evaluate the solutions over a large interval of frequencies. Once the first peak is found, the value of the scalar field at the origin is taken to be $\phi_0 + \Delta\phi$ and the scan in frequency is performed starting from the previously found value $\omega_{\rm res}(\phi_0)$. As discussed in the main text, for large values of $|\gamma|$ and for $\phi_0 \sim \phi^{\gamma}_{0,\max}$, the distance between resonant peaks in the frequency space becomes very small. This makes finding the first resonant peak a difficult problem, as one needs to have a step fine enough to resolve it. This issue can be alleviated by dynamically adapting the frequency step, *i.e.* making it smaller with increasing $|\gamma|$ and ϕ_0.

Finally, some convergence checks can be performed on the solutions. In particular, both functions $f(r)$ and $g(r)$ should tend to the Schwarzschild

lapse function for $r > R$, *i.e.*

$$f_0\tilde{f}(r),\, g(r) \xrightarrow{r\to\infty} \left(1 - \frac{2M}{r}\right), \tag{B.13}$$

with M the ADM mass of the spacetime. Thus, we fit the numerical solutions to the Schwarzschild function and compare the best-fit values of M. If the values obtained from $f(r)$ and from $g(r)$ differ by less than 0.01% we consider the result of the integration to be trustworthy. Note that this agreement only happens if the scalar field has decayed enough so that we have effectively reached the asymptotically flat region. The value of f_0 is also obtained via this fitting procedure.

Appendix C

Additional material related to chapter 4

C.1 Evolution equations in the BBSN formalism

We give here the evolution equations for the BSSN variables $\{\phi, \tilde{\gamma}_{ij}, \tilde{A}_{ij}, K, \tilde{\Gamma}^i\}$ for completeness. They satisfy the system of partial differential equations

$$\partial_t \phi = -\frac{1}{6}\alpha K + \beta^i \partial_i \phi + \frac{1}{6}\partial_i \beta^i, \tag{C.1}$$

$$\partial_t \tilde{\gamma}_{ij} = -2\alpha \tilde{A}_{ij} + \beta^k \partial_k \tilde{\gamma}_{ij} + \tilde{\gamma}_{ik}\partial_j \beta^k + \tilde{\gamma}_{kj}\partial_i \beta^k - \frac{2}{3}\tilde{\gamma}_{ij}\partial_k \beta^k, \tag{C.2}$$

$$\partial_t K = -\gamma^{ij} D_i D_j \alpha + \alpha(\tilde{A}_{ij}\tilde{A}^{ij} + \frac{1}{3}K^2) + 4\pi\alpha(\rho + S) + \beta^i \partial_i K, \tag{C.3}$$

$$\begin{aligned}\partial_t \tilde{A}_{ij} = {} & e^{-4\phi}\left(-(D_i D_j \alpha)^{TF} + \alpha(R_{ij}^{TF} - 8\pi S_{ij}^{TF})\right) + \alpha(K\tilde{A}_{ij} - 2\tilde{A}_{il}\tilde{A}^l_j) \\ & + \beta^k \partial_k \tilde{A}_{ij} + \tilde{A}_{ik}\partial_j \beta^k + \tilde{A}_{kj}\partial_i \beta^k - \frac{2}{3}\tilde{A}_{ij}\partial_k \beta^k,\end{aligned} \tag{C.4}$$

$$\begin{aligned}\partial_t \tilde{\Gamma}^i = {} & -2\tilde{A}^{ij}\partial_j \alpha + 2\alpha\left(\tilde{\Gamma}^i_{jk}\tilde{A}^{kj} - \frac{2}{3}\tilde{\gamma}^{ij}\partial_j K - 8\pi\tilde{\gamma}^{ij}S_j + 6\tilde{A}^{ij}\partial_j \phi\right) \\ & + \beta^j \partial_j \tilde{\Gamma}^i - \tilde{\Gamma}^j \partial_j \beta^i + \frac{2}{3}\tilde{\Gamma}^i \partial_j \beta^j + \frac{1}{3}\tilde{\gamma}^{li}\partial_l \partial_j \beta^j + \tilde{\gamma}^{lj}\partial_l \partial_j \beta^i.\end{aligned} \tag{C.5}$$

The label TF indicates that the trace-free part of the tensors should be considered, i.e. $Q_{ij}^{TF} = Q_{ij} - \gamma_{ij} Q/3$.

C.2 Evolution equations in the CCZ4 formalism

We give here the evolution equations for the CCZ4 variables $\{\chi, \tilde{\gamma}_{ij}, K, \tilde{A}_{ij}, \Theta, \hat{\Gamma}^i\}$ for completeness. They satisfy the system of partial differential equations

$$\partial_t \chi = \beta^k \partial_k \chi + \frac{2}{3}\chi(\alpha K - \partial_k \beta^k), \tag{C.6}$$

$$\partial_t \tilde{\gamma}_{ij} = \beta^k \partial_k \tilde{\gamma}_{ij} + \tilde{\gamma}_{ki}\partial_j \beta^k + \tilde{\gamma}_{kj}\partial_i \beta^k - 2\alpha \tilde{A}_{ij} - \frac{2}{3}\tilde{\gamma}_{ij}\partial_k \beta^k, \tag{C.7}$$

$$\begin{aligned}\partial_t K = {} & \beta^k \partial_k K + \alpha\left(\hat{R} + K(K - 2\Theta)\right) - 3\alpha\kappa_1(1+\kappa_2)\Theta \\ & - \gamma^{kl} D_k D_l \alpha + 4\pi\alpha(S - 3\rho),\end{aligned} \tag{C.8}$$

$$\begin{aligned}\partial_t \tilde{A}_{ij} = {} & \beta^k \partial_k \tilde{A}_{ij} + \chi\left[-D_i D_j \alpha + \alpha(\hat{R}_{ij} - 8\pi S_{ij})\right]^{\mathrm{TF}} \\ & + \tilde{A}_{ij}\left[\alpha(K - 2\Theta) - \frac{2}{3}\partial_k \beta^k\right] + 2\tilde{A}_{k(i}\partial_{j)}\beta^k - 2\alpha\tilde{\gamma}^{kl}\tilde{A}_{ik}\tilde{A}_{lj},\end{aligned} \tag{C.9}$$

$$\begin{aligned}\partial_t \Theta = {} & \beta^k \partial_k \Theta + \frac{1}{2}\alpha\left(\hat{R} - \tilde{A}_{kl}\tilde{A}^{kl} + \frac{2}{3}K^2 - 2\Theta K\right) - \alpha\kappa_1\Theta(2+\kappa_2) \\ & - \Theta^k \partial_k \alpha - 8\pi\alpha\rho,\end{aligned} \tag{C.10}$$

$$\begin{aligned}\partial_t \hat{\Gamma}^i = {} & \beta^k \partial_k \hat{\Gamma}^i + \frac{2}{3}\left[\partial_k \beta^k\left(\tilde{\Gamma}^i + 2\kappa_3\frac{\Theta^i}{\chi}\right) - 2\alpha K\frac{\Theta^i}{\chi}\right] - 2\alpha\kappa_1\frac{\Theta^i}{\chi} \\ & + 2\tilde{\gamma}^{ik}(\alpha\partial_k\Theta - \Theta\partial_k\alpha) - 2\tilde{A}^{ik}\partial_k\alpha + 2\alpha\tilde{\Gamma}^i_{kl}\tilde{A}^{kl} \\ & - \alpha\left[\frac{4}{3}\tilde{\gamma}^{ik}\partial_k K + 3\tilde{A}^{ik}\frac{\partial_k\chi}{\chi}\right] - \left(\tilde{\Gamma}^k + 2\kappa_3\frac{\Theta^k}{\chi}\right)\partial_k\beta^i \\ & + \tilde{\gamma}^{kl}\partial_k\partial_l\beta^i + \frac{1}{3}\tilde{\gamma}^{ik}\partial_l\partial_k\beta^l - 16\pi\alpha\tilde{\gamma}^{ik}S_k,\end{aligned} \tag{C.11}$$

with $\hat{R}_{ij} = R_{ij} + 2D_{(i}\Theta_{j)}$ and κ_3 an extra damping parameter.

C.3 Matter equations in the ADM decomposition

In the $3+1$ decomposition, the Einstein-Klein-Gordon equation (4.36) reduces to two first-order equations

$$\Pi = \frac{1}{\alpha}(\partial_t \Phi - \beta^i \partial_i \Phi), \tag{C.12}$$

$$\partial_t \Pi = \beta^i \partial_i \Pi + \alpha \Bigg(K\,\Pi + D_i D^i \Phi - \frac{\gamma^2 \bar{\Phi}}{2\left(1 - \frac{\gamma^2}{4}|\Phi|^2\right)} (\Pi^2 - D_i \Phi\, D^i \Phi)$$

$$- 2\Phi \left(1 - \frac{\gamma^2}{4}|\Phi|^2\right)^2 U'(|\Phi|^2) \Bigg). \tag{C.13}$$

Two additional equations emerge for the complex conjugates $(\bar{\Phi}, \bar{\Pi})$, which are considered as independent variables, sending $\Phi \to \bar{\Phi}$, $\Pi \to \bar{\Pi}$ in equations (C.12) and (C.13).

The field's four-dimensional stress-energy tensor reads

$$T_{\mu\nu} = \frac{1}{2\left(1 - \frac{\gamma^2}{4}|\Phi|^2\right)^2} \left(\nabla_\mu \Phi \nabla_\nu \bar{\Phi} + \nabla_\nu \Phi \nabla_\mu \bar{\Phi} - g_{\mu\nu} \nabla_\sigma \Phi \nabla^\sigma \bar{\Phi}\right) - g_{\mu\nu}\, U(|\Phi|^2). \tag{C.14}$$

After decomposing the Einstein field equations in the $(3+1)$ formalism, the stress-energy tensor components associated to the scalar field Φ read

$$\rho = \frac{1}{2\left(1 - \frac{\gamma^2}{4}|\Phi|^2\right)^2} (D_i \bar{\Phi}\, D^i \Phi + \Pi\, \bar{\Pi}) + U(|\Phi|^2), \tag{C.15}$$

$$S_i = \frac{1}{2\left(1 - \frac{\gamma^2}{4}|\Phi|^2\right)^2} (\bar{\Pi}\, D_i \Phi + \Pi\, D_i \bar{\Phi}), \tag{C.16}$$

$$S_{ij} = \frac{1}{2\left(1 - \frac{\gamma^2}{4}|\Phi|^2\right)^2} \big(\gamma_{ij}\, (\Pi\, \bar{\Pi} - D_i \bar{\Phi}\, D^i \Phi)$$

$$+ D_i \bar{\Phi} D_j\, \Phi + D_i \Phi\, D_j \bar{\Phi}\big) - \gamma_{ij}\, U(|\Phi|^2). \tag{C.17}$$

C.4 Convergence

In this section, we describe the convergence test we performed on our code. To assess the accuracy of a numericall simulation and to get an estimate of the numerical error, one should perform the simulations at different resolutions, and compare the differences in the output. The discrepancies between the numerical results should scale appropriately given the order of the numerical scheme used in the evolution.

We start by checking the appropriate convergence of the initial conditions solver, which calculates the violations of the hamiltonian and momentum constraints for the initial metric and matter distributions. Convergence is achieved if the constraints violations scale as

$$\frac{H_{LR}}{H_{HR}} = \left(\frac{\Delta_{LR}}{\Delta_{HR}}\right)^n, \tag{C.18}$$

with Δ_{LR} the grid resolution at low resolution (LR), Δ_{HR} the grid resolution at high resolution (HR) and n the order of the code's finite-difference scheme. In Figure C.1 we plot the values of the residuals for the hamiltonian and momentum constraints in the case $\gamma^2 = 0$ and with an isolated BH at the centre of the domain. The plots show that the convergence is, as expected, of second order. The spikes in the constraint violations correspond to the boundaries of the mesh refinement levels.

We then tested the convergence of the orbital phase Ψ defined in this work for a BBH system with scalar field mass $\mu M = 0.3$ and $\gamma^2 = 10^5$, evolved with `GRChombo`. In Figure C.2 we plot the cumulated phase difference between three grid resolutions. We ran simulations with identical physical and initial parameters with a number of cells on the coarsest level of $N = 128$, $N = 160$ and $N = 192$, for low (LR), medium (MR) and high (HR) resolutions respectively. It demonstrates that the convergence order during the inspiral and merger of Ψ is around two, with a mild overconvergence during a brief part of the inspiral which was also observed in the detailed study carried out in [196]. This is consistent with the order of convergence of our initial data solver `GRTresna`. The results of the convergence analysis presented here indicate that our simulations are stable and in the convergent regime.

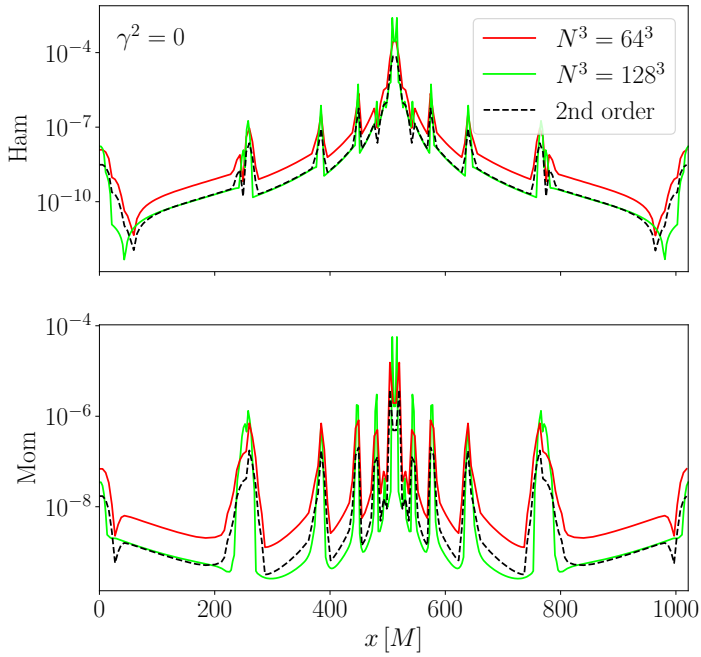

Figure C.1: Difference across resolutions for the Hamiltonian and momentum constraints in space domain for the initial data obtained with `GRTresna`.

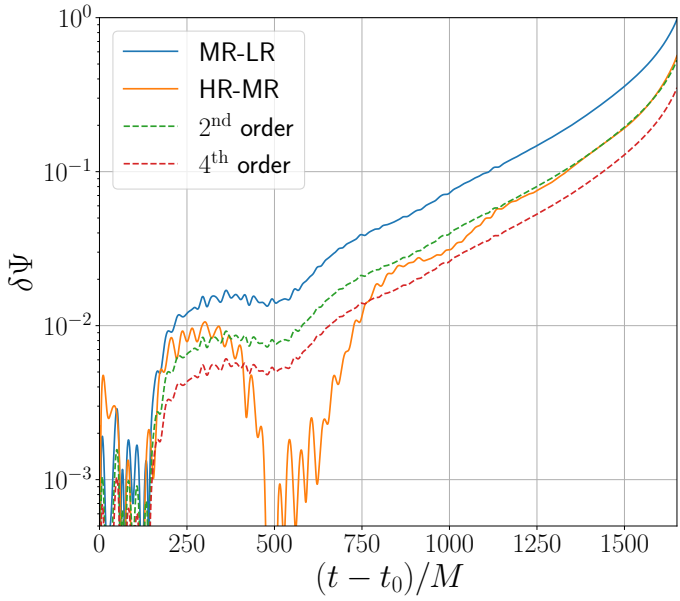

Figure C.2: Difference in accumulated phase in between high resolution (HR), mid resolution (MR) and low resolution (LR) simulations of a BBH with scalar field mass $\mu M = 0.3$ and $\gamma^2 = 10^5$.

Bibliography

[1] A. G. Abac et al. "GW231123: a Binary Black Hole Merger with Total Mass 190-265 $M_\odot$". In: (July 2025). arXiv: 2507.08219 [astro-ph.HE].

[2] A. G. Abac et al. "GWTC-4.0: An Introduction to Version 4.0 of the Gravitational-Wave Transient Catalog". In: (Aug. 2025). arXiv: 2508.18080 [gr-qc].

[3] A. G. Abac et al. "Observation of Gravitational Waves from the Coalescence of a 2.5–4.5 $M_\odot$ Compact Object and a Neutron Star". In: *Astrophys. J. Lett.* 970.2 (2024), p. L34. DOI: 10.3847/2041-8213/ad5beb. arXiv: 2404.04248 [astro-ph.HE].

[4] B. P. Abbott et al. "Multi-messenger Observations of a Binary Neutron Star Merger". In: *Astrophys. J. Lett.* 848.2 (2017), p. L12. DOI: 10.3847/2041-8213/aa91c9. arXiv: 1710.05833 [astro-ph.HE].

[5] B. P. Abbott et al. "Observation of Gravitational Waves from a Binary Black Hole Merger". In: *Phys. Rev. Lett.* 116.6 (2016), p. 061102. DOI: 10.1103/PhysRevLett.116.061102. arXiv: 1602.03837 [gr-qc].

[6] N. Afshordi et al. "Waveform Modelling for the Laser Interferometer Space Antenna". In: (Nov. 2023). arXiv: 2311.01300 [gr-qc].

[7] M. Alcubierre, J. Barranco, A. Bernal, J. C. Degollado, A. Diez-Tejedor, V. Jaramillo, M. Megevand, D. Núñez, and O. Sarbach. "Extreme ℓ-boson stars". In: *Class. Quant. Grav.* 39.9 (2022), p. 094001. DOI: 10.1088/1361-6382/ac5fc2. arXiv: 2112.04529 [gr-qc].

[8] M. Alcubierre, J. Barranco, A. Bernal, J. C. Degollado, A. Diez-Tejedor, M. Megevand, D. Nunez, and O. Sarbach. "ℓ-Boson stars". In: *Class. Quant. Grav.* 35.19 (2018), 19LT01. DOI: 10.1088/1361-6382/aadcb6. arXiv: 1805.11488 [gr-qc].

[9] M. Alcubierre, J. Barranco, A. Bernal, J. C. Degollado, A. Diez-Tejedor, M. Megevand, D. Núñez, and O. Sarbach. "Dynamical evolutions of ℓ-boson stars in spherical symmetry". In: *Class. Quant. Grav.* 36.21 (2019), p. 215013. DOI: 10.1088/1361-6382/ab4726. arXiv: 1906.08959 [gr-qc].

[10] D. Alic, C. Bona-Casas, C. Bona, L. Rezzolla, and C. Palenzuela. "Conformal and covariant formulation of the Z4 system with constraint-violation damping". In: *Phys. Rev. D* 85 (2012), p. 064040. DOI: 10.1103/PhysRevD.85.064040. arXiv: 1106.2254 [gr-qc].

[11] B. Allen, W. G. Anderson, P. R. Brady, D. A. Brown, and J. D. E. Creighton. "FINDCHIRP: An Algorithm for detection of gravitational waves from inspiraling compact binaries". In: *Phys. Rev. D* 85 (2012), p. 122006. DOI: 10.1103/PhysRevD.85.122006. arXiv: gr-qc/0509116.

[12] P. Amaro-Seoane, J. Barranco, A. Bernal, and L. Rezzolla. "Constraining scalar fields with stellar kinematics and collisional dark matter". In: *JCAP* 11 (2010), p. 002. DOI: 10.1088/1475-7516/2010/11/002. arXiv: 1009.0019 [astro-ph.CO].

[13] T. Andrade et al. "GRChombo: An adaptable numerical relativity code for fundamental physics". In: *J. Open Source Softw.* 6.68 (2021), p. 3703. DOI: 10.21105/joss.03703. arXiv: 2201.03458 [gr-qc].

[14] L. Aresté Saló, K. Clough, and P. Figueras. "Puncture gauge formulation for Einstein-Gauss-Bonnet gravity and four-derivative scalar-tensor theories in d+1 spacetime dimensions". In: *Phys. Rev. D* 108.8 (2023), p. 084018. DOI: 10.1103/PhysRevD.108.084018. arXiv: 2306.14966 [gr-qc].

[15] L. Aresté Saló, K. Clough, and P. Figueras. "Well-Posedness of the Four-Derivative Scalar-Tensor Theory of Gravity in Singularity Avoiding Coordinates". In: *Phys. Rev. Lett.* 129.26 (2022), p. 261104. DOI: 10.1103/PhysRevLett.129.261104. arXiv: 2208.14470 [gr-qc].

[16] L. Aresté Saló, D. D. Doneva, K. Clough, P. Figueras, and S. S. Yazadjiev. "Challenges in the nonlinear evolution of unequal mass binaries in sGB gravity". In: (July 2025). arXiv: 2507.13046 [gr-qc].

[17] R. L. Arnowitt, S. Deser, and C. W. Misner. "The Dynamics of general relativity". In: *Gen. Rel. Grav.* 40 (2008), pp. 1997–2027. DOI: 10.1007/s10714-008-0661-1. arXiv: gr-qc/0405109.

[18] A. Arvanitaki, S. Dimopoulos, S. Dubovsky, N. Kaloper, and J. March-Russell. "String Axiverse". In: *Phys. Rev. D* 81 (2010), p. 123530. DOI: 10.1103/PhysRevD.81.123530. arXiv: 0905.4720 [hep-th].

[19] A. Arvanitaki and S. Dubovsky. "Exploring the String Axiverse with Precision Black Hole Physics". In: *Phys. Rev. D* 83 (2011), p. 044026. DOI: 10.1103/PhysRevD.83.044026. arXiv: 1004.3558 [hep-th].

[20] J. C. Aurrekoetxea, K. Clough, and E. A. Lim. "CTTK: A New Method to Solve the Initial Data Constraints in Numerical Relativity". In: *Class. Quantum Grav.* 40.7 (Mar. 2023), p. 075003. ISSN: 0264-9381. DOI: 10.1088/1361-6382/acb883. (Visited on 04/02/2025).

[21] J. C. Aurrekoetxea et al. "GRTresna: An open-source code to solve the initial data constraints in numerical relativity". In: (Jan. 2025). arXiv: 2501.13046 [gr-qc].

[22] J. C. Aurrekoetxea, K. Clough, J. Bamber, and P. G. Ferreira. "Effect of Wave Dark Matter on Equal Mass Black Hole Mergers". In: *Phys. Rev. Lett.* 132.21 (2024), p. 211401. DOI: 10.1103/PhysRevLett.132.211401. arXiv: 2311.18156 [gr-qc].

[23] J. C. Aurrekoetxea, K. Clough, J. Bamber, and P. G. Ferreira. "Effect of Wave Dark Matter on Equal Mass Black Hole Mergers". In: *Phys. Rev. Lett.* 132 (21 May 2024), p. 211401. DOI: 10.1103/PhysRevLett.132.211401. URL: https://link.aps.org/doi/10.1103/PhysRevLett.132.211401.

[24] J. C. Aurrekoetxea, P. G. Ferreira, K. Clough, E. A. Lim, and O. J. Tattersall. "Where is the ringdown: Reconstructing quasinormal modes from dispersive waves". In: *Phys. Rev. D* 106.10 (2022), p. 104002. DOI: 10.1103/PhysRevD.106.104002. arXiv: 2205.15878 [gr-qc].

[25] J. C. Aurrekoetxea, J. Marsden, K. Clough, and P. G. Ferreira. "Self-interacting scalar dark matter around binary black holes". In: *Phys. Rev. D* 110.8 (2024), p. 083011. DOI: 10.1103/PhysRevD.110.083011. arXiv: 2409.01937 [gr-qc].

[26] J. Balakrishna, E. Seidel, and W.-M. Suen. "Dynamical evolution of boson stars. 2. Excited states and selfinteracting fields". In: *Phys. Rev. D* 58 (1998), p. 104004. DOI: 10.1103/PhysRevD.58.104004. arXiv: gr-qc/9712064.

[27] J. Bamber, J. C. Aurrekoetxea, K. Clough, and P. G. Ferreira. "Black hole merger simulations in wave dark matter environments". In: *Phys. Rev. D* 107.2 (2023), p. 024035. DOI: 10.1103/PhysRevD.107.024035. arXiv: 2210.09254 [gr-qc].

[28] J. Bamber, K. Clough, P. G. Ferreira, L. Hui, and M. Lagos. "Growth of accretion driven scalar hair around Kerr black holes". In: *Phys. Rev. D* 103.4 (2021), p. 044059. DOI: 10.1103/PhysRevD.103.044059. arXiv: 2011.07870 [gr-qc].

[29] E. Barausse, V. Cardoso, and P. Pani. "Can environmental effects spoil precision gravitational-wave astrophysics?" In: *Phys. Rev. D* 89.10 (2014), p. 104059. DOI: 10.1103/PhysRevD.89.104059. arXiv: 1404.7149 [gr-qc].

[30] C. Barcelo and M. Visser. "Twilight for the energy conditions?" In: *Int. J. Mod. Phys. D* 11 (2002), pp. 1553–1560. DOI: 10.1142/S0218271802002888. arXiv: gr-qc/0205066.

[31] D. Baumann, G. Bertone, J. Stout, and G. M. Tomaselli. "Ionization of gravitational atoms". In: *Phys. Rev. D* 105.11 (2022), p. 115036. DOI: 10.1103/PhysRevD.105.115036. arXiv: 2112.14777 [gr-qc].

[32] D. Baumann, G. Bertone, J. Stout, and G. M. Tomaselli. "Sharp Signals of Boson Clouds in Black Hole Binary Inspirals". In: *Phys. Rev. Lett.* 128.22 (2022), p. 221102. DOI: 10.1103/PhysRevLett.128.221102. arXiv: 2206.01212 [gr-qc].

[33] D. Baumann, H. S. Chia, and R. A. Porto. "Probing Ultralight Bosons with Binary Black Holes". In: *Phys. Rev. D* 99.4 (2019), p. 044001. DOI: 10.1103/PhysRevD.99.044001. arXiv: 1804.03208 [gr-qc].

[34] D. Baumann, H. S. Chia, J. Stout, and L. ter Haar. "The Spectra of Gravitational Atoms". In: *JCAP* 12 (2019), p. 006. DOI: 10.1088/1475-7516/2019/12/006. arXiv: 1908.10370 [gr-qc].

[35] T. W. Baumgarte and S. L. Shapiro. *Numerical Relativity: Solving Einstein's Equations on the Computer*. Cambridge University Press, 2010. DOI: 10.1017/CBO9781139193344.

[36] T. W. Baumgarte and S. L. Shapiro. "On the numerical integration of Einstein's field equations". In: *Phys. Rev. D* 59 (1998), p. 024007. DOI: 10.1103/PhysRevD.59.024007. arXiv: gr-qc/9810065.

[37] N. Becker, L. Sagunski, L. Prinz, and S. Rastgoo. "Circularization versus eccentrification in intermediate mass ratio inspirals inside dark matter spikes". In: *Phys. Rev. D* 105.6 (2022), p. 063029. DOI: 10.1103/PhysRevD.105.063029. arXiv: 2112.09586 [gr-qc].

[38] E. Berti, R. Brito, C. F. B. Macedo, G. Raposo, and J. L. Rosa. "Ultralight boson cloud depletion in binary systems". In: *Phys. Rev. D* 99.10 (2019), p. 104039. DOI: 10.1103/PhysRevD.99.104039. arXiv: 1904.03131 [gr-qc].

[39] E. Berti, V. Cardoso, and A. O. Starinets. "Quasinormal modes of black holes and black branes". In: *Class. Quant. Grav.* 26 (2009), p. 163001. DOI: 10.1088/0264-9381/26/16/163001. arXiv: 0905.2975 [gr-qc].

[40] E. Berti, A. Sesana, E. Barausse, V. Cardoso, and K. Belczynski. "Spectroscopy of Kerr black holes with Earth- and space-based interferometers". In: *Phys. Rev. Lett.* 117.10 (2016), p. 101102. DOI: 10.1103/PhysRevLett.117.101102. arXiv: 1605.09286 [gr-qc].

[41] E. Berti, K. Yagi, and N. Yunes. "Extreme Gravity Tests with Gravitational Waves from Compact Binary Coalescences: (I) Inspiral-Merger". In: *Gen. Rel. Grav.* 50.4 (2018), p. 46. DOI: 10.1007/s10714-018-2362-8. arXiv: 1801.03208 [gr-qc].

[42] G. Bertone et al. "Gravitational wave probes of dark matter: challenges and opportunities". In: *SciPost Phys. Core* 3 (2020), p. 007. DOI: 10.21468/SciPostPhysCore.3.2.007. arXiv: 1907.10610 [astro-ph.CO].

[43] G. Bertone and D. Hooper. "History of dark matter". In: *Rev. Mod. Phys.* 90.4 (2018), p. 045002. DOI: 10.1103/RevModPhys.90.045002. arXiv: 1605.04909 [astro-ph.CO].

[44] G. Bertone and D. Merritt. "Time-dependent models for dark matter at the Galactic Center". In: *Phys. Rev. D* 72 (2005), p. 103502. DOI: 10.1103/PhysRevD.72.103502. arXiv: astro-ph/0501555.

[45] G. Bertone, A. R. A. C. Wierda, D. Gaggero, B. J. Kavanagh, M. Volonteri, and N. Yoshida. "Dark Matter Mounds: towards a realistic description of dark matter overdensities around black holes". In: (Apr. 2024). arXiv: 2404.08731 [astro-ph.CO].

[46] S. Bhagwat, C. Pacilio, P. Pani, and M. Mapelli. "Landscape of stellar-mass black-hole spectroscopy with third-generation gravitational-wave detectors". In: *Phys. Rev. D* 108.4 (2023), p. 043019. DOI: 10.1103/PhysRevD.108.043019. arXiv: 2304.02283 [gr-qc].

[47] R. P. Bhatt, S. Chakraborty, and S. Bose. "Addressing issues in defining the Love numbers for black holes". In: *Phys. Rev. D* 108.8 (2023), p. 084013. DOI: 10.1103/PhysRevD.108.084013. arXiv: 2306.13627 [gr-qc].

[48] R. P. Bhatt, S. Chakraborty, and S. Bose. "Rotating black holes experience dynamical tides". In: (June 2024). arXiv: 2406.09543 [gr-qc].

[49] J. Binney and S. Tremaine. *Galactic Dynamics: Second Edition*. Princeton University Press, 2008.

[50] T. Binnington and E. Poisson. "Relativistic theory of tidal Love numbers". In: *Phys. Rev. D* 80 (2009), p. 084018. DOI: 10.1103/PhysRevD.80.084018. arXiv: 0906.1366 [gr-qc].

[51] C. Bona, T. Ledvinka, C. Palenzuela, and M. Zacek. "General covariant evolution formalism for numerical relativity". In: *Phys. Rev. D* 67 (2003), p. 104005. DOI: 10.1103/PhysRevD.67.104005. arXiv: gr-qc/0302083.

[52] C. Bona, J. Masso, E. Seidel, and J. Stela. "A New formalism for numerical relativity". In: *Phys. Rev. Lett.* 75 (1995), pp. 600–603. DOI: 10.1103/PhysRevLett.75.600. arXiv: gr-qc/9412071.

[53] J. M. Bowen and J. W. York Jr. "Time asymmetric initial data for black holes and black hole collisions". In: *Phys. Rev. D* 21 (1980), pp. 2047–2056. DOI: 10.1103/PhysRevD.21.2047.

[54] P. Brax, C. P. Burgess, and F. Quevedo. "Lifting Klein-Gordon/Einstein solutions to general nonlinear sigma-models: the wormhole example". In: *JHEP* 02 (2024), p. 130. DOI: 10.1007/JHEP02(2024)130. arXiv: 2308.12004 [hep-th].

[55] R. Brito, V. Cardoso, and P. Pani. "Black holes as particle detectors: evolution of superradiant instabilities". In: *Class. Quant. Grav.* 32.13 (2015), p. 134001. DOI: 10.1088/0264-9381/32/13/134001. arXiv: 1411.0686 [gr-qc].

[56] R. Brito, V. Cardoso, and P. Pani. "Superradiance: New Frontiers in Black Hole Physics". In: *Lect. Notes Phys.* 906 (2015), pp.1–237. DOI: 10.1007/978-3-319-19000-6.

[57] R. Brito, S. Ghosh, E. Barausse, E. Berti, V. Cardoso, I. Dvorkin, A. Klein, and P. Pani. "Gravitational wave searches for ultralight bosons with LIGO and LISA". In: *Phys. Rev. D* 96.6 (2017), p. 064050. DOI: 10.1103/PhysRevD.96.064050. arXiv: 1706.06311 [gr-qc].

[58] R. Brito and S. Shah. "Extreme mass-ratio inspirals into black holes surrounded by scalar clouds". In: *Phys. Rev. D* 108.8 (2023). [Erratum: Phys.Rev.D 110, 109902 (2024)], p. 084019. DOI: 10.1103/PhysRevD.108.084019. arXiv: 2307.16093 [gr-qc].

[59] A. Buchel. "AdS boson stars in string theory". In: (Oct. 2015). arXiv: 1510.08415 [hep-th].

[60] A. Buchel and M. Buchel. "On stability of nonthermal states in strongly coupled gauge theories". In: (Sept. 2015). arXiv: 1509.00774 [hep-th].

[61] A. Buchel, S. L. Liebling, and L. Lehner. "Boson stars in AdS spacetime". In: *Phys. Rev. D* 87.12 (2013), p. 123006. DOI: 10.1103/PhysRevD.87.123006. arXiv: 1304.4166 [gr-qc].

[62] P. Bueno, P. A. Cano, F. Goelen, T. Hertog, and B. Vercnocke. "Echoes of Kerr-like wormholes". In: *Phys. Rev. D* 97.2 (2018), p. 024040. DOI: 10.1103/PhysRevD.97.024040. arXiv: 1711.00391 [gr-qc].

[63] A. Buonanno and T. Damour. "Effective one-body approach to general relativistic two-body dynamics". In: *Phys. Rev. D* 59 (1999), p. 084006. DOI: 10.1103/PhysRevD.59.084006. arXiv: gr-qc/9811091.

[64] C. P. Burgess, R. C. Myers, and F. Quevedo. "On spherically symmetric string solutions in four-dimensions". In: *Nucl. Phys. B* 442 (1995), pp. 75–96. DOI: 10.1016/S0550-3213(95)00090-9. arXiv: hep-th/9410142.

[65] P. A. Cano, K. Fransen, T. Hertog, and S. Maenaut. "Quasinormal modes of rotating black holes in higher-derivative gravity". In: *Phys. Rev. D* 108.12 (2023), p. 124032. DOI: 10.1103/PhysRevD.108.124032. arXiv: 2307.07431 [gr-qc].

[66] P. A. Cano, L. Machet, and C. Myin. "Boson Stars with Nonlinear Sigma Models". In: *Phys. Rev. D* 109.4 (2024), p. 044043. DOI: 10.1103/PhysRevD.109.044043.

[67] V. Cardoso, K. Destounis, F. Duque, R. P. Macedo, and A. Maselli. "Black holes in galaxies: Environmental impact on gravitational-wave generation and propagation". In: *Phys. Rev. D* 105.6 (2022), p. L061501. DOI: 10.1103/PhysRevD.105.L061501. arXiv: 2109.00005 [gr-qc].

[68] V. Cardoso, K. Destounis, F. Duque, R. Panosso Macedo, and A. Maselli. "Gravitational Waves from Extreme-Mass-Ratio Systems in Astrophysical Environments". In: *Phys. Rev. Lett.* 129.24 (2022), p. 241103. DOI: 10.1103/PhysRevLett.129.241103. arXiv: 2210.01133 [gr-qc].

[69] V. Cardoso and F. Duque. "Environmental effects in gravitational-wave physics: Tidal deformability of black holes immersed in matter". In: *Phys. Rev. D* 101.6 (2020), p. 064028. DOI: 10.1103/PhysRevD.101.064028. arXiv: 1912.07616 [gr-qc].

[70] V. Cardoso, F. Duque, and T. Ikeda. "Tidal effects and disruption in superradiant clouds: a numerical investigation". In: *Phys. Rev. D* 101.6 (2020), p. 064054. DOI: 10.1103/PhysRevD.101.064054. arXiv: 2001.01729 [gr-qc].

[71] V. Cardoso, E. Franzin, A. Maselli, P. Pani, and G. Raposo. "Testing strong-field gravity with tidal Love numbers". In: *Phys. Rev. D* 95.8 (2017). [Addendum: Phys.Rev.D 95, 089901 (2017)], p. 084014. DOI: 10.1103/PhysRevD.95.084014. arXiv: 1701.01116 [gr-qc].

[72] V. Cardoso, C. F. B. Macedo, K.-i. Maeda, and H. Okawa. "ECO-spotting: looking for extremely compact objects with bosonic fields". In: *Class. Quant. Grav.* 39.3 (2022), p. 034001. DOI: 10.1088/1361-6382/ac41e7. arXiv: 2112.05750 [gr-qc].

[73] V. Cardoso, A. S. Miranda, E. Berti, H. Witek, and V. T. Zanchin. "Geodesic stability, Lyapunov exponents and quasinormal modes". In: *Phys. Rev. D* 79.6 (2009), p. 064016. DOI: 10.1103/PhysRevD.79.064016. arXiv: 0812.1806 [hep-th].

[74] V. Cardoso and P. Pani. "Testing the nature of dark compact objects: a status report". In: *Living Rev. Rel.* 22.1 (2019), p. 4. DOI: 10.1007/s41114-019-0020-4. arXiv: 1904.05363 [gr-qc].

[75] V. Cardoso and P. Pani. "Tests for the existence of black holes through gravitational wave echoes". In: *Nature Astron.* 1.9 (2017), pp. 586–591. DOI: 10.1038/s41550-017-0225-y. arXiv: 1709.01525 [gr-qc].

[76] G. Carullo, D. Laghi, N. K. Johnson-McDaniel, W. Del Pozzo, O. J. C. Dias, M. Godazgar, and J. E. Santos. "Constraints on Kerr-Newman black holes from merger-ringdown gravitational-wave observations". In: *Phys. Rev. D* 105.6 (2022), p. 062009. DOI: 10.1103/PhysRevD.105.062009. arXiv: 2109.13961 [gr-qc].

[77] S. K. Chakrabarti. "Gravitational wave emission from a binary black hole system in the presence of an accretion disk". In: *Phys. Rev. D* 53 (1996), pp. 2901–2907. DOI: 10.1103/PhysRevD.53.2901. arXiv: astro-ph/9603117.

[78] S. Chakraborty, G. Compère, and L. Machet. "Tidal Love numbers and quasinormal modes of the Schwarzschild-Hernquist black hole". In: *Phys. Rev. D* 112.2 (2025), p. 024015. DOI: 10.1103/4p2c-rwdh. arXiv: 2412.14831 [gr-qc].

[79] S. Chakraborty, E. Maggio, M. Silvestrini, and P. Pani. "Dynamical tidal Love numbers of Kerr-like compact objects". In: *Phys. Rev. D* 110.8 (2024), p. 084042. DOI: 10.1103/PhysRevD.110.084042. arXiv: 2310.06023 [gr-qc].

[80] P. Charalambous, S. Dubovsky, and M. M. Ivanov. "On the Vanishing of Love Numbers for Kerr Black Holes". In: *JHEP* 05 (2021), p. 038. DOI: 10.1007/JHEP05(2021)038. arXiv: 2102.08917 [hep-th].

[81] H. S. Chia. "Tidal deformation and dissipation of rotating black holes". In: *Phys. Rev. D* 104.2 (2021), p. 024013. DOI: 10.1103/PhysRevD.104.024013. arXiv: 2010.07300 [gr-qc].

[82] K. Clough. "Continuity equations for general matter: applications in numerical relativity". In: *Class. Quant. Grav.* 38.16 (2021), p. 167001. DOI: 10.1088/1361-6382/ac10ee. arXiv: 2104.13420 [gr-qc].

[83] K. Clough, P. G. Ferreira, and M. Lagos. "Growth of massive scalar hair around a Schwarzschild black hole". In: *Phys. Rev. D* 100.6 (2019), p. 063014. DOI: 10.1103/PhysRevD.100.063014. arXiv: 1904.12783 [gr-qc].

[84] P. S. Cole, G. Bertone, A. Coogan, D. Gaggero, T. Karydas, B. J. Kavanagh, T. F. M. Spieksma, and G. M. Tomaselli. "Distinguishing environmental effects on binary black hole gravitational waveforms". In: *Nature Astron.* 7.8 (2023), pp. 943–950. DOI: 10.1038/s41550-023-01990-2. arXiv: 2211.01362 [gr-qc].

[85] M. Colpi, S. L. Shapiro, and I. Wasserman. "Boson Stars: Gravitational Equilibria of Self-Interacting Scalar Fields". In: *Phys. Rev. Lett.* 57 (20 Nov. 1986), pp. 2485–2488. DOI: 10.1103/PhysRevLett.57.2485. URL: https://link.aps.org/doi/10.1103/PhysRevLett.57.2485.

[86] A. Coogan, G. Bertone, D. Gaggero, B. J. Kavanagh, and D. A. Nichols. "Measuring the dark matter environments of black hole binaries with gravitational waves". In: *Phys. Rev. D* 105.4 (2022), p. 043009. DOI: 10.1103/PhysRevD.105.043009. arXiv: 2108.04154 [gr-qc].

[87] P. V. P. Cunha, J. A. Font, C. Herdeiro, E. Radu, N. Sanchis-Gual, and M. Zilhão. "Lensing and dynamics of ultracompact bosonic stars". In: *Phys. Rev. D* 96.10 (2017), p. 104040. DOI: 10.1103/PhysRevD.96.104040. arXiv: 1709.06118 [gr-qc].

[88] P. V. P. Cunha, C. Herdeiro, E. Radu, and N. Sanchis-Gual. "Exotic Compact Objects and the Fate of the Light-Ring Instability". In: *Phys. Rev. Lett.* 130.6 (2023), p. 061401. DOI: 10.1103/PhysRevLett.130.061401. arXiv: 2207.13713 [gr-qc].

[89] E. Cuoco, M. Cavaglià, I. S. Heng, D. Keitel, and C. Messenger. "Applications of machine learning in gravitational-wave research with current interferometric detectors". In: *Living Rev. Rel.* 28.1 (2025), p. 2. DOI: 10.1007/s41114-024-00055-8. arXiv: 2412.15046 [gr-qc].

[90] C. Cutler and M. Vallisneri. "LISA detections of massive black hole inspirals: Parameter extraction errors due to inaccurate template waveforms". In: *Phys. Rev. D* 76 (2007), p. 104018. DOI: 10.1103/PhysRevD.76.104018. arXiv: 0707.2982 [gr-qc].

[91] M. Cvetic, G. W. Gibbons, and C. N. Pope. "Photon Spheres and Sonic Horizons in Black Holes from Supergravity and Other Theories". In: *Phys. Rev. D* 94.10 (2016), p. 106005. DOI: 10.1103/PhysRevD.94.106005. arXiv: 1608.02202 [gr-qc].

[92] T. Damour and S. N. Solodukhin. "Wormholes as black hole foils". In: *Phys. Rev. D* 76 (2007), p. 024016. DOI: 10.1103/PhysRevD.76.024016. arXiv: 0704.2667 [gr-qc].

[93] V. De Luca, L. Del Grosso, F. Iacovelli, A. Maselli, and E. Berti. "Systematic biases from ignoring environmental tidal effects in gravitational wave observations". In: *Phys. Rev. D* 111.12 (2025), p. 124046. DOI: 10.1103/h4nh-nl5s. arXiv: 2503.10746 [gr-qc].

[94] J. F. M. Delgado, C. A. R. Herdeiro, and E. Radu. "Rotating Axion Boson Stars". In: *JCAP* 06 (2020), p. 037. DOI: 10.1088/1475-7516/2020/06/037. arXiv: 2005.05982 [gr-qc].

[95] A. Diez-Tejedor, A. X. Gonzalez-Morales, and S. Profumo. "Dwarf spheroidal galaxies and Bose-Einstein condensate dark matter". In: *Phys. Rev. D* 90.4 (2014), p. 043517. DOI: 10.1103/PhysRevD.90.043517. arXiv: 1404.1054 [astro-ph.GA].

[96] S. R. Dolan. "Instability of the massive Klein-Gordon field on the Kerr spacetime". In: *Phys. Rev. D* 76 (2007), p. 084001. DOI: 10.1103/PhysRevD.76.084001. arXiv: 0705.2880 [gr-qc].

[97] D. D. Doneva, L. Aresté Saló, K. Clough, P. Figueras, and S. S. Yazadjiev. "Testing the limits of scalar-Gauss-Bonnet gravity through nonlinear evolutions of spin-induced scalarization". In: *Phys. Rev. D* 108.8 (2023), p. 084017. DOI: 10.1103/PhysRevD.108.084017. arXiv: 2307.06474 [gr-qc].

[98] D. D. Doneva, L. Aresté Saló, and S. S. Yazadjiev. "3+1 nonlinear evolution of Ricci-coupled scalar-Gauss-Bonnet gravity". In: *Phys. Rev. D* 110.2 (2024), p. 024040. DOI: 10.1103/PhysRevD.110.024040. arXiv: 2404.15526 [gr-qc].

[99] O. Dreyer, B. J. Kelly, B. Krishnan, L. S. Finn, D. Garrison, and R. Lopez-Aleman. "Black hole spectroscopy: Testing general relativity through gravitational wave observations". In: *Class. Quant. Grav.* 21 (2004), pp. 787–804. DOI: 10.1088/0264-9381/21/4/003. arXiv: gr-qc/0309007.

[100] F. Duque. "Gravitational Waves and the Galactic Potential". PhD thesis. U. Lisbon (main), 2023. arXiv: 2308.03850 [gr-qc].

[101] W. E. East and F. Pretorius. "Superradiant Instability and Backreaction of Massive Vector Fields around Kerr Black Holes". In: *Phys. Rev. Lett.* 119.4 (2017), p. 041101. DOI: 10.1103/PhysRevLett.119.041101. arXiv: 1704.04791 [gr-qc].

[102] J. Eby, C. Kouvaris, N. G. Nielsen, and L. C. R. Wijewardhana. "Boson Stars from Self-Interacting Dark Matter". In: *JHEP* 02 (2016), p. 028. DOI: 10.1007/JHEP02(2016)028. arXiv: 1511.04474 [hep-ph].

[103] K. Eda, Y. Itoh, S. Kuroyanagi, and J. Silk. "Gravitational waves as a probe of dark matter minispikes". In: *Phys. Rev. D* 91.4 (2015), p. 044045. DOI: 10.1103/PhysRevD.91.044045. arXiv: 1408.3534 [gr-qc].

[104] A. Einstein. "On a Stationary System With Spherical Symmetry Consisting of Many Gravitating Masses". In: *Annals of Mathematics* 40.4 (1939), pp. 922–936. ISSN: 0003486X. URL: http://www.jstor.org/stable/1968902 (visited on 11/24/2022).

[105] T. Evstafyeva, U. Sperhake, T. Helfer, R. Croft, M. Radia, B.-X. Ge, and E. A. Lim. "Unequal-mass boson-star binaries: initial data and merger dynamics". In: *Class. Quant. Grav.* 40.8 (2023), p. 085009. DOI: 10.1088/1361-6382/acc2a8. arXiv: 2212.08023 [gr-qc].

[106] V. Ferrari and L. Gualtieri. "Quasi-Normal Modes and Gravitational Wave Astronomy". In: *Gen. Rel. Grav.* 40 (2008), pp. 945–970. DOI: 10.1007/s10714-007-0585-1. arXiv: 0709.0657 [gr-qc].

[107] E. G. M. Ferreira. "Ultra-light dark matter". In: *Astron. Astrophys. Rev.* 29.1 (2021), p. 7. DOI: 10.1007/s00159-021-00135-6. arXiv: 2005.03254 [astro-ph.CO].

[108] F. Ferrer, A. M. da Rosa, and C. M. Will. "Dark matter spikes in the vicinity of Kerr black holes". In: *Phys. Rev. D* 96.8 (2017), p. 083014. DOI: 10.1103/PhysRevD.96.083014. arXiv: 1707.06302 [astro-ph.CO].

[109] E. Figueiredo, A. Maselli, and V. Cardoso. "Black holes surrounded by generic dark matter profiles: Appearance and gravitational-wave emission". In: *Phys. Rev. D* 107.10 (2023), p. 104033. DOI: 10.1103/PhysRevD.107.104033. arXiv: 2303.08183 [gr-qc].

[110] P. Figueras and T. França. "Black hole binaries in cubic Horndeski theories". In: *Phys. Rev. D* 105.12 (2022), p. 124004. DOI: 10.1103/PhysRevD.105.124004. arXiv: 2112.15529 [gr-qc].

[111] P. Figueras and T. França. "Gravitational Collapse in Cubic Horndeski Theories". In: *Class. Quant. Grav.* 37.22 (2020), p. 225009. DOI: 10.1088/1361-6382/abb693. arXiv: 2006.09414 [gr-qc].

[112] P. Figueras, T. França, C. Gu, and T. Andrade. "Endpoint of the Gregory-Laflamme instability of black strings revisited". In: *Phys. Rev. D* 107.4 (2023), p. 044028. DOI: 10.1103/PhysRevD.107.044028. arXiv: 2210.13501 [hep-th].

[113] P. Figueras, M. Kunesch, and S. Tunyasuvunakool. "End Point of Black Ring Instabilities and the Weak Cosmic Censorship Conjecture". In: *Phys. Rev. Lett.* 116.7 (2016), p. 071102. DOI: 10.1103/PhysRevLett.116.071102. arXiv: 1512.04532 [hep-th].

[114] L. S. Finn and K. S. Thorne. "Gravitational waves from a compact star in a circular, inspiral orbit, in the equatorial plane of a massive, spinning black hole, as observed by LISA". In: *Phys. Rev. D* 62 (2000), p. 124021. DOI: 10.1103/PhysRevD.62.124021. arXiv: gr-qc/0007074.

[115] R. Friedberg, T. D. Lee, and Y. Pang. "Scalar soliton stars and black holes". In: *Phys. Rev. D* 35 (12 June 1987), pp. 3658–3677. DOI: 10.1103/PhysRevD.35.3658. URL: https://link.aps.org/doi/10.1103/PhysRevD.35.3658.

[116] B.-X. Ge, E. A. Lim, U. Sperhake, T. Evstafyeva, D. Cors, E. de Jong, R. Croft, and T. Helfer. "Hair is complicated: Gravitational waves from stable and unstable boson-star mergers". In: (Oct. 2024). arXiv: 2410.23839 [gr-qc].

[117] A. Geralico, F. Pompi, and R. Ruffini. "On Einstein clusters". In: *Int. J. Mod. Phys. Conf. Ser.* 12 (2012). Ed. by R. Ruffini, pp. 146–173. DOI: 10.1142/S2010194512006356.

[118] M. Gleiser. "Stability of Boson Stars". In: *Phys. Rev. D* 38 (1988). [Erratum: Phys.Rev.D 39, 1257 (1989)], p. 2376. DOI: 10.1103/PhysRevD.38.2376.

[119] O. Y. Gnedin and J. R. Primack. "Dark Matter Profile in the Galactic Center". In: *Phys. Rev. Lett.* 93 (2004), p. 061302. DOI: 10.1103/PhysRevLett.93.061302. arXiv: astro-ph/0308385.

[120] P. Gondolo and J. Silk. "Dark matter annihilation at the galactic center". In: *Phys. Rev. Lett.* 83 (1999), pp. 1719–1722. DOI: 10.1103/PhysRevLett.83.1719. arXiv: astro-ph/9906391.

[121] D. Guerra, C. F. B. Macedo, and P. Pani. "Axion boson stars". In: *JCAP* 09.09 (2019). [Erratum: JCAP 06, E01 (2020)], p. 061. DOI: 10.1088/1475-7516/2019/09/061. arXiv: 1909.05515 [gr-qc].

[122] C. Gundlach, J. M. Martin-Garcia, G. Calabrese, and I. Hinder. "Constraint damping in the Z4 formulation and harmonic gauge". In: *Class. Quant. Grav.* 22 (2005), pp. 3767–3774. DOI: 10.1088/0264-9381/22/17/025. arXiv: gr-qc/0504114.

[123] G. Guo, Y. Lu, P. Wang, H. Wu, and H. Yang. "Black Holes with Multiple Photon Spheres". In: (Dec. 2022). arXiv: 2212.12901 [gr-qc].

[124] J. Halverson, C. Long, and P. Nath. "Ultralight axion in supersymmetry and strings and cosmology at small scales". In: *Phys. Rev. D* 96.5 (2017), p. 056025. DOI: 10.1103/PhysRevD.96.056025. arXiv: 1703.07779 [hep-ph].

[125] M. Hannam, P. Schmidt, A. Bohé, L. Haegel, S. Husa, F. Ohme, G. Pratten, and M. Pürrer. "Simple Model of Complete Precessing Black-Hole-Binary Gravitational Waveforms". In: *Phys. Rev. Lett.* 113.15 (2014), p. 151101. DOI: 10.1103/PhysRevLett.113.151101. arXiv: 1308.3271 [gr-qc].

[126] S. W. Hawking and G. F. R. Ellis. *The Large Scale Structure of Space-Time*. Cambridge Monographs on Mathematical Physics. Cambridge University Press, 1973. DOI: 10.1017/CBO9780511524646.

[127] T. Helfer, E. A. Lim, M. A. G. Garcia, and M. A. Amin. "Gravitational Wave Emission from Collisions of Compact Scalar Solitons". In: *Phys. Rev. D* 99.4 (2019), p. 044046. DOI: 10.1103/PhysRevD.99.044046. arXiv: 1802.06733 [gr-qc].

[128] C. Herdeiro, I. Perapechka, E. Radu, and Y. Shnir. "Gravitating solitons and black holes with synchronised hair in the four dimensional O(3) sigma-model". In: *JHEP* 02 (2019), p. 111. DOI: 10.1007/JHEP02(2019)111. arXiv: 1811.11799 [gr-qc].

[129] C. A. R. Herdeiro, A. M. Pombo, E. Radu, P. V. P. Cunha, and N. Sanchis-Gual. "The imitation game: Proca stars that can mimic the Schwarzschild shadow". In: *JCAP* 04 (2021), p. 051. DOI: 10.1088/1475-7516/2021/04/051. arXiv: 2102.01703 [gr-qc].

[130] C. A. R. Herdeiro and E. Radu. "Asymptotically flat black holes with scalar hair: a review". In: *Int. J. Mod. Phys. D* 24.09 (2015). Ed. by C. A. R. Herdeiro, V. Cardoso, J. P. S. Lemos, and F. C. Mena, p. 1542014. DOI: 10.1142/S0218271815420146. arXiv: 1504.08209 [gr-qc].

[131] T. Hinderer. "Tidal Love numbers of neutron stars". In: *Astrophys. J.* 677 (2008). [Erratum: Astrophys.J. 697, 964 (2009)], pp. 1216–1220. DOI: 10.1086/533487. arXiv: 0711.2420 [astro-ph].

[132] T. Hinderer and É. É. Flanagan. "Two-timescale analysis of extreme mass ratio inspirals in Kerr spacetime: Orbital motion". In: *Phys. Rev. D* 78 (6 Sept. 2008), p. 064028.

[133] J. Ho, S.-j. Kim, and B.-H. Lee. "Maximum mass of boson star formed by selfinteracting scalar fields". In: (Feb. 1999). arXiv: gr-qc/9902040.

[134] B. Holdom and J. Ren. "Not quite a black hole". In: *Phys. Rev. D* 95.8 (2017), p. 084034. DOI: 10.1103/PhysRevD.95.084034. arXiv: 1612.04889 [gr-qc].

[135] L. Hui. "Wave Dark Matter". In: *Ann. Rev. Astron. Astrophys.* 59 (2021), pp. 247–289. DOI: 10.1146/annurev-astro-120920-010024. arXiv: 2101.11735 [astro-ph.CO].

[136] T. Jacobson. "Primordial black hole evolution in tensor scalar cosmology". In: *Phys. Rev. Lett.* 83 (1999), pp. 2699–2702. DOI: 10.1103/PhysRevLett.83.2699. arXiv: astro-ph/9905303.

[137] V. Jaramillo, N. Sanchis-Gual, J. Barranco, A. Bernal, J. C. Degollado, C. Herdeiro, and D. Núñez. "Dynamical ℓ -boson stars: Generic stability and evidence for nonspherical solutions". In: *Phys. Rev. D* 101.12 (2020), p. 124020. DOI: 10.1103/PhysRevD.101.124020. arXiv: 2004.08459 [gr-qc].

[138] P. Jetzer and J. Van Der Bij. "Charged boson stars". In: *Physics Letters B* 227.3 (1989), pp. 341–346. ISSN: 0370-2693. DOI: https://doi.org/10.1016/0370-2693(89)90941-6. URL: https://www.sciencedirect.com/science/article/pii/0370269389909416.

[139] P. Jetzer. "Boson stars". In: *Physics Reports* 220.4 (1992), pp. 163–227. ISSN: 0370-1573. DOI: https://doi.org/10.1016/0370-1573(92)90123-H. URL: https://www.sciencedirect.com/science/article/pii/037015739290123H.

[140] T. K. Karydas, B. J. Kavanagh, and G. Bertone. "Sharpening the dark matter signature in gravitational waveforms I: Accretion and eccentricity evolution". In: (Feb. 2024). arXiv: 2402.13053 [gr-qc].

[141] D. Kasen, B. Metzger, J. Barnes, E. Quataert, and E. Ramirez-Ruiz. "Origin of the heavy elements in binary neutron-star mergers from a gravitational wave event". In: *Nature* 551 (2017), p. 80. DOI: 10.1038/nature24453. arXiv: 1710.05463 [astro-ph.HE].

[142] M. L. Katz, A. J. K. Chua, L. Speri, N. Warburton, and S. A. Hughes. "Fast extreme-mass-ratio-inspiral waveforms: New tools for millihertz gravitational-wave data analysis". In: *Phys. Rev. D* 104.6 (2021), p. 064047. DOI: 10.1103/PhysRevD.104.064047. arXiv: 2104.04582 [gr-qc].

[143] D. J. Kaup. "Klein-Gordon Geon". In: *Phys. Rev.* 172 (5 Aug. 1968), pp. 1331–1342. DOI: 10.1103/PhysRev.172.1331. URL: https://link.aps.org/doi/10.1103/PhysRev.172.1331.

[144] B. J. Kavanagh, D. A. Nichols, G. Bertone, and D. Gaggero. "Detecting dark matter around black holes with gravitational waves: Effects of dark-matter dynamics on the gravitational waveform". In: *Phys. Rev. D* 102.8 (2020), p. 083006. DOI: 10.1103/PhysRevD.102.083006. arXiv: 2002.12811 [gr-qc].

[145] M. Khlopov, B. A. Malomed, and I. B. Zeldovich. "Gravitational instability of scalar fields and formation of primordial black holes". In: *Mon. Not. Roy. Astron. Soc.* 215 (1985), pp. 575–589.

[146] L. E. Kidder, M. A. Scheel, and S. A. Teukolsky. "Extending the lifetime of 3-D black hole computations with a new hyperbolic system of evolution equations". In: *Phys. Rev. D* 64 (2001), p. 064017. DOI: 10.1103/PhysRevD.64.064017. arXiv: gr-qc/0105031.

[147] R. A. Konoplya. "Black holes in galactic centers: Quasinormal ringing, grey-body factors and Unruh temperature". In: *Phys. Lett. B* 823 (2021), p. 136734. DOI: 10.1016/j.physletb.2021.136734. arXiv: 2109.01640 [gr-qc].

[148] R. A. Konoplya. "Quasinormal behavior of the d-dimensional Schwarzschild black hole and higher order WKB approach". In: *Phys. Rev. D* 68 (2003), p. 024018. DOI: 10.1103/PhysRevD.68.024018. arXiv: gr-qc/0303052.

[149] F. V. Kusmartsev, E. W. Mielke, and F. E. Schunck. "Gravitational stability of boson stars". In: *Phys. Rev. D* 43 (12 June 1991), pp. 3895–3901. DOI: 10.1103/PhysRevD.43.3895. URL: https://link.aps.org/doi/10.1103/PhysRevD.43.3895.

[150] A. Le Tiec, M. Casals, and E. Franzin. "Tidal Love Numbers of Kerr Black Holes". In: *Phys. Rev. D* 103.8 (2021), p. 084021. DOI: 10.1103/PhysRevD.103.084021. arXiv: 2010.15795 [gr-qc].

[151] T. D. Lee. "Soliton stars and the critical masses of black holes". In: *Phys. Rev. D* 35 (12 June 1987), pp. 3637–3639. DOI: 10.1103/PhysRevD.35.3637. URL: https://link.aps.org/doi/10.1103/PhysRevD.35.3637.

[152] T. D. Lee and Y. Pang. "Stability of Mini - Boson Stars". In: *Nucl. Phys. B* 315 (1989). Ed. by H.-C. Ren and Y. Pang, p. 477. DOI: 10.1016/0550-3213(89)90365-9.

[153] T. Lee and Y. Pang. "Nontopological solitons". In: *Physics Reports* 221.5 (1992), pp. 251–350. ISSN: 0370-1573. DOI: https://doi.org/10.1016/0370-1573(92)90064-7. URL: https://www.sciencedirect.com/science/article/pii/0370157392900647.

[154] S. H. W. Leong, J. Calderón Bustillo, M. Gracia-Linares, and P. Laguna. "Detectability of dense-environment effects on black-hole mergers: The scalar field case, higher-order ringdown modes, and parameter biases". In: *Phys. Rev. D* 108.12 (2023), p. 124079. DOI: 10.1103/PhysRevD.108.124079. arXiv: 2308.03250 [gr-qc].

[155] B. Li, T. Rindler-Daller, and P. R. Shapiro. "Cosmological Constraints on Bose-Einstein-Condensed Scalar Field Dark Matter". In: *Phys. Rev. D* 89.8 (2014), p. 083536. DOI: 10.1103/PhysRevD.89.083536. arXiv: 1310.6061 [astro-ph.CO].

[156] S. L. Liebling. "The Nonlinear sigma model with distributed adaptive mesh refinement". In: *Class. Quant. Grav.* 21 (2004), p. 3995. DOI: 10.1088/0264-9381/21/16/012. arXiv: gr-qc/0403076.

[157] S. L. Liebling, E. W. Hirschmann, and J. Isenberg. "Critical phenomena in nonlinear sigma models". In: *J. Math. Phys.* 41 (2000), pp. 5691–5700. DOI: 10.1063/1.533432. arXiv: math-ph/9911020.

[158] S. L. Liebling and C. Palenzuela. "Dynamical boson stars". In: *Living Rev. Rel.* 26.1 (2023), p. 1. DOI: 10.1007/s41114-023-00043-4. arXiv: 1202.5809 [gr-qc].

[159] W. Liu, X. Fang, J. Jing, and A. Wang. "Gauge invariant perturbations of general spherically symmetric spacetimes". In: *Sci. China Phys. Mech. Astron.* 66.1 (2023), p. 210411. DOI: 10.1007/s11433-022-1956-4. arXiv: 2201.01259 [gr-qc].

[160] Y. T. Liu, Z. B. Etienne, and S. L. Shapiro. "Evolution of near-extremal-spin black holes using the moving puncture technique". In: *Phys. Rev. D* 80 (2009), p. 121503. DOI: 10.1103/PhysRevD.80.121503. arXiv: 1001.4077 [gr-qc].

[161] C. F. B. Macedo, P. Pani, V. Cardoso, and L. C. B. Crispino. "Astrophysical signatures of boson stars: quasinormal modes and inspiral resonances". In: *Phys. Rev. D* 88.6 (2013), p. 064046. DOI: 10.1103/PhysRevD.88.064046. arXiv: 1307.4812 [gr-qc].

[162] C. F. B. Macedo, P. Pani, V. Cardoso, and L. C. B. Crispino. "Into the lair: gravitational-wave signatures of dark matter". In: *Astrophys. J.* 774 (2013), p. 48. DOI: 10.1088/0004-637X/774/1/48. arXiv: 1302.2646 [gr-qc].

[163] P. Mach and A. Odrzywołek. "Accretion of the relativistic Vlasov gas onto a moving Schwarzschild black hole: Exact solutions". In: *Phys. Rev. D* 103 (2 Jan. 2021), p. 024044. URL: https://link.aps.org/doi/10.1103/PhysRevD.103.024044.

[164] L. Machet and L. Aresté Saló. "Scalar fields from nonlinear sigma models on black hole spacetimes". In: *Phys. Rev. D* 112.8 (2025), p. 084047. DOI: 10.1103/klxz-fgmt. arXiv: 2508.18362 [gr-qc].

[165] M. Maggiore et al. "Science Case for the Einstein Telescope". In: *JCAP* 03 (2020), p. 050. DOI: 10.1088/1475-7516/2020/03/050. arXiv: 1912.02622 [astro-ph.CO].

[166] G. A. Marks, S. J. Staelens, T. Evstafyeva, and U. Sperhake. "Long-term stable nonlinear evolutions of ultracompact black-hole mimickers". In: (Apr. 2025). arXiv: 2504.17775 [gr-qc].

[167] T. Marrodán Undagoitia and L. Rauch. "Dark matter direct-detection experiments". In: *J. Phys. G* 43.1 (2016), p. 013001. DOI: 10.1088/0954-3899/43/1/013001. arXiv: 1509.08767 [physics.ins-det].

[168] P. Martín–Moruno and M. Visser. "Classical and Semi-classical Energy Conditions". In: *Wormholes, Warp Drives and Energy Conditions*. Ed. by F. S. N. Lobo. Cham: Springer International Publishing, 2017, pp. 193–213. ISBN: 978-3-319-55182-1. DOI: 10.1007/978-3-319-55182-1_9. URL: https://doi.org/10.1007/978-3-319-55182-1_9.

[169] S. D. Mathur. "The Fuzzball proposal for black holes: An Elementary review". In: *Fortsch. Phys.* 53 (2005). Ed. by E. Kiritsis, pp. 793–827. DOI: 10.1002/prop.200410203. arXiv: hep-th/0502050.

[170] D. R. Mayerson and B. Vercnocke. "Observational Opportunities for the Fuzzball Program". In: (June 2023). arXiv: 2306.01565 [hep-th].

[171] P. O. Mazur and E. Mottola. "Gravitational Condensate Stars: An Alternative to Black Holes". In: *Universe* 9.2 (2023), p. 88. DOI: 10.3390/universe9020088. arXiv: gr-qc/0109035.

[172] M. van de Meent and H. P. Pfeiffer. "Intermediate mass-ratio black hole binaries: Applicability of small mass-ratio perturbation theory". In: *Phys. Rev. Lett.* 125.18 (2020), p. 181101. DOI: 10.1103/PhysRevLett.125.181101. arXiv: 2006.12036 [gr-qc].

[173] R. F. P. Mendes and H. Yang. "Tidal deformability of boson stars and dark matter clumps". In: *Class. Quant. Grav.* 34.18 (2017), p. 185001. DOI: 10.1088/1361-6382/aa842d. arXiv: 1606.03035 [astro-ph.CO].

[174] D. Merritt. "Evolution of the dark matter distribution at the galactic center". In: *Phys. Rev. Lett.* 92 (2004), p. 201304. DOI: 10.1103/PhysRevLett.92.201304. arXiv: astro-ph/0311594.

[175] E. W. Mielke and F. E. Schunck. "Are axidilaton stars massive compact halo objects?" In: *Gen. Rel. Grav.* 33 (2001), pp. 805–813. DOI: 10.1023/A:1010251707026.

[176] E. W. Mielke. "Rotating Boson Stars". In: *Fundam. Theor. Phys.* 183 (2016). Ed. by T. Asselmeyer-Maluga, pp. 115–131. DOI: 10.1007/978-3-319-31299-6_6.

[177] A. Milekhin and N. Sukhov. "All holographic systems have scar states". In: (July 2023). arXiv: 2307.11348 [hep-th].

[178] A. K. Mishra, G. Carullo, and S. Chakraborty. "Bounds on tidal charges from gravitational wave ringdown observations". In: *Phys. Rev. D* 109.2 (2024), p. 024025. DOI: 10.1103/PhysRevD.109.024025. arXiv: 2311.03556 [gr-qc].

[179] S. Mitra, S. Chakraborty, R. Vicente, and J. C. Feng. "Probing the quantum nature of black holes with ultralight boson environments". In: *Phys. Rev. D* 110.8 (2024), p. 084012. DOI: 10.1103/PhysRevD.110.084012. arXiv: 2312.06783 [gr-qc].

[180] S. Mitra, N. Speeney, S. Chakraborty, and E. Berti. "Extreme mass ratio inspirals in rotating dark matter spikes". In: *Phys. Rev. D* 112.4 (2025), p. 044030. DOI: 10.1103/ycl1-kx7d. arXiv: 2505.04697 [gr-qc].

[181] S. Mondal and M. Bagchi. "f-mode oscillations of anisotropic neutron stars in full general relativity". In: *Phys. Rev. D* 110.12 (2024), p. 123011. DOI: 10.1103/PhysRevD.110.123011. arXiv: 2309.00439 [gr-qc].

[182] M. S. Morris, K. S. Thorne, and U. Yurtsever. "Wormholes, Time Machines, and the Weak Energy Condition". In: *Phys. Rev. Lett.* 61 (1988), pp. 1446–1449. DOI: 10.1103/PhysRevLett.61.1446.

[183] D. Mukherjee, A. M. Holgado, G. Ogiya, and H. Trac. "Examining the effects of dark matter spikes on eccentric intermediate-mass ratio inspirals using N-body simulations". In: *Mon. Not. Roy. Astron. Soc.* 533.2 (2024), pp. 2335–2355. DOI: 10.1093/mnras/stae1989. arXiv: 2312.02275 [astro-ph.CO].

[184] S. Nair, S. Chakraborty, and S. Sarkar. "Asymptotically de Sitter black holes have nonzero tidal Love numbers". In: *Phys. Rev. D* 109.6 (2024), p. 064025. DOI: 10.1103/PhysRevD.109.064025. arXiv: 2401.06467 [gr-qc].

[185] D. A. Nichols, B. A. Wade, and A. M. Grant. "Secondary accretion of dark matter in intermediate mass-ratio inspirals: Dark-matter dynamics and gravitational-wave phase". In: *Phys. Rev. D* 108.12 (2023), p. 124062. DOI: 10.1103/PhysRevD.108.124062. arXiv: 2309.06498 [gr-qc].

[186] T. Ortin. *Gravity and Strings*. 2nd ed. Cambridge Monographs on Mathematical Physics. Cambridge University Press, July 2015. ISBN: 978-0-521-76813-9, 978-0-521-76813-9, 978-1-316-23579-9. DOI: 10.1017/CBO9781139019750.

[187] P. Pani. "Binary pulsars as dark-matter probes". In: *Phys. Rev. D* 92.12 (2015), p. 123530. DOI: 10.1103/PhysRevD.92.123530. arXiv: 1512.01236 [astro-ph.HE].

[188] P. Pani and A. Maselli. "Love in Extrema Ratio". In: *Int. J. Mod. Phys. D* 28.14 (2019), p. 1944001. DOI: 10.1142/S0218271819440012. arXiv: 1905.03947 [gr-qc].

[189] L. Perivolaropoulos and F. Skara. "Challenges for ΛCDM: An update". In: *New Astron. Rev.* 95 (2022), p. 101659. DOI: 10.1016/j.newar.2022.101659. arXiv: 2105.05208 [astro-ph.CO].

[190] L. Pezzella, K. Destounis, A. Maselli, and V. Cardoso. "Quasinormal modes of black holes embedded in halos of matter". In: *Phys. Rev. D* 111.6 (2025), p. 064026. DOI: 10.1103/PhysRevD.111.064026. arXiv: 2412.18651 [gr-qc].

[191] L. Pierini and L. Gualtieri. "Quasi-normal modes of rotating black holes in Einstein-dilaton Gauss-Bonnet gravity: the first order in rotation". In: *Phys. Rev. D* 103 (2021), p. 124017. DOI: 10.1103/PhysRevD.103.124017. arXiv: 2103.09870 [gr-qc].

[192] R. A. Porto. "The Tune of Love and the Nature(ness) of Spacetime". In: *Fortsch. Phys.* 64.10 (2016), pp. 723–729. DOI: 10.1002/prop.201600064. arXiv: 1606.08895 [gr-qc].

[193] E. A. Power and J. A. Wheeler. “Thermal Geons”. In: *Rev. Mod. Phys.* 29 (3 July 1957), pp. 480–495. DOI: 10.1103/RevModPhys.29.480. URL: https://link.aps.org/doi/10.1103/RevModPhys.29.480.

[194] F. Pretorius. “Evolution of binary black hole spacetimes”. In: *Phys. Rev. Lett.* 95 (2005), p. 121101. DOI: 10.1103/PhysRevLett.95.121101. arXiv: gr-qc/0507014.

[195] M. Pürrer and C.-J. Haster. “Gravitational waveform accuracy requirements for future ground-based detectors”. In: *Phys. Rev. Res.* 2.2 (2020), p. 023151. DOI: 10.1103/PhysRevResearch.2.023151. arXiv: 1912.10055 [gr-qc].

[196] M. Radia, U. Sperhake, A. Drew, K. Clough, P. Figueras, E. A. Lim, J. L. Ripley, J. C. Aurrekoetxea, T. França, and T. Helfer. “Lessons for Adaptive Mesh Refinement in Numerical Relativity”. In: *Class. Quantum Grav.* 39.13 (July 2022). Comment: 46 pages, 10 figures, to match version published in CQG, p. 135006. ISSN: 0264-9381, 1361-6382. DOI: 10.1088/1361-6382/ac6fa9. arXiv: 2112.10567 [gr-qc]. (Visited on 04/02/2025).

[197] D. Reitze et al. “Cosmic Explorer: The U.S. Contribution to Gravitational-Wave Astronomy beyond LIGO”. In: *Bull. Am. Astron. Soc.* 51.7 (2019), p. 035. arXiv: 1907.04833 [astro-ph.IM].

[198] P. Rioseco and O. Sarbach. “Accretion of a relativistic, collisionless kinetic gas into a Schwarzschild black hole”. In: *Classical and Quantum Gravity* 34.9 (Apr. 2017), p. 095007. URL: https://doi.org/10.1088/1361-6382/aa65fa.

[199] J. L. Rosa, P. Garcia, F. H. Vincent, and V. Cardoso. “Observational signatures of hot spots orbiting horizonless objects”. In: *Phys. Rev. D* 106.4 (2022), p. 044031. DOI: 10.1103/PhysRevD.106.044031. arXiv: 2205.11541 [gr-qc].

[200] J. L. Rosa, C. F. B. Macedo, and D. Rubiera-Garcia. “Imaging compact boson stars with hot spots and thin accretion disks”. In: *Phys. Rev. D* 108.4 (2023), p. 044021. DOI: 10.1103/PhysRevD.108.044021. arXiv: 2303.17296 [gr-qc].

[201] J. L. Rosa and D. Rubiera-Garcia. “Shadows of boson and Proca stars with thin accretion disks”. In: *Phys. Rev. D* 106.8 (2022), p. 084004. DOI: 10.1103/PhysRevD.106.084004. arXiv: 2204.12949 [gr-qc].

[202] S. Roy and R. Vicente. “Compact Binary Coalescences in Dense Environments Can Pose as in Vacuum”. In: (Oct. 2024). arXiv: 2410.16388 [gr-qc].

[203] V. C. Rubin and W. K. Ford Jr. “Rotation of the Andromeda Nebula from a Spectroscopic Survey of Emission Regions”. In: *Astrophys. J.* 159 (1970), pp. 379–403. DOI: 10.1086/150317.

[204] R. RUFFINI and S. BONAZZOLA. “Systems of Self-Gravitating Particles in General Relativity and the Concept of an Equation of State”. In: *Phys. Rev.* 187 (5 Nov. 1969), pp. 1767–1783. DOI: 10.1103/PhysRev.187.1767. URL: https://link.aps.org/doi/10.1103/PhysRev.187.1767.

[205] L. Sadeghian, F. Ferrer, and C. M. Will. “Dark matter distributions around massive black holes: A general relativistic analysis”. In: *Phys. Rev. D* 88.6 (2013), p. 063522. DOI: 10.1103/PhysRevD.88.063522. arXiv: 1305.2619 [astro-ph.GA].

[206] S. Sarkar, M. Rahman, and S. Chakraborty. “Perturbing the perturbed: Stability of quasinormal modes in presence of a positive cosmological constant”. In: *Phys. Rev. D* 108.10 (2023), p. 104002. DOI: 10.1103/PhysRevD.108.104002. arXiv: 2304.06829 [gr-qc].

[207] F. E. Schunck and E. W. Mielke. “General relativistic boson stars”. In: *Class. Quant. Grav.* 20 (2003), R301–R356. DOI: 10.1088/0264-9381/20/20/201. arXiv: 0801.0307 [astro-ph].

[208] S. L. Shapiro and J. Shelton. “Weak annihilation cusp inside the dark matter spike about a black hole”. In: *Phys. Rev. D* 93.12 (2016), p. 123510. DOI: 10.1103/PhysRevD.93.123510. arXiv: 1606.01248 [astro-ph.HE].

[209] M. Shibata and T. Nakamura. “Evolution of three-dimensional gravitational waves: Harmonic slicing case”. In: *Phys. Rev. D* 52 (1995), pp. 5428–5444. DOI: 10.1103/PhysRevD.52.5428.

[210] N. Speeney, A. Antonelli, V. Baibhav, and E. Berti. “The impact of relativistic corrections on the detectability of dark-matter spikes with gravitational waves”. In: (Apr. 2022). arXiv: 2204.12508 [gr-qc].

[211] N. Speeney, E. Berti, V. Cardoso, and A. Maselli. “Black holes surrounded by generic matter distributions: Polar perturbations and energy flux”. In: *Phys. Rev. D* 109.8 (2024), p. 084068. DOI: 10.1103/PhysRevD.109.084068. arXiv: 2401.00932 [gr-qc].

[212] T. F. M. Spieksma, V. Cardoso, G. Carullo, M. Della Rocca, and F. Duque. “Black hole spectroscopy in environments: detectability prospects”. In: (Sept. 2024). arXiv: 2409.05950 [gr-qc].

[213] H. Takeda, A. Nishizawa, Y. Michimura, K. Nagano, K. Komori, M. Ando, and K. Hayama. “Polarization test of gravitational waves from compact binary coalescences”. In: *Phys. Rev. D* 98.2 (2018), p. 022008. DOI: 10.1103/PhysRevD.98.022008. arXiv: 1806.02182 [gr-qc].

[214] G. M. Tomaselli, T. F. M. Spieksma, and G. Bertone. "Dynamical friction in gravitational atoms". In: *JCAP* 07 (2023), p. 070. DOI: 10.1088/1475-7516/2023/07/070. arXiv: 2305.15460 [gr-qc].

[215] D. Traykova, R. Vicente, K. Clough, T. Helfer, E. Berti, P. G. Ferreira, and L. Hui. "Relativistic drag forces on black holes from scalar dark matter clouds of all sizes". In: *Phys. Rev. D* 108.12 (2023), p. L121502. DOI: 10.1103/PhysRevD.108.L121502. arXiv: 2305.10492 [gr-qc].

[216] P. Ullio, H. Zhao, and M. Kamionkowski. "A Dark matter spike at the galactic center?" In: *Phys. Rev. D* 64 (2001), p. 043504. DOI: 10.1103/PhysRevD.64.043504. arXiv: astro-ph/0101481.

[217] E. Vasiliev. "Dark matter annihilation near a black hole: Plateau vs. weak cusp". In: *Phys. Rev. D* 76 (2007), p. 103532. DOI: 10.1103/PhysRevD.76.103532. arXiv: 0707.3334 [astro-ph].

[218] Y. Verbin. "Sigma model Q-balls and Q-stars". In: *Phys. Rev. D* 76 (2007), p. 085018. DOI: 10.1103/PhysRevD.76.085018. arXiv: 0708.3283 [gr-qc].

[219] R. Vicente, T. K. Karydas, and G. Bertone. "A fully relativistic treatment of EMRIs in collisionless environments". In: (May 2025). arXiv: 2505.09715 [gr-qc].

[220] L. Visinelli. "Boson stars and oscillatons: A review". In: *Int. J. Mod. Phys. D* 30.15 (2021), p. 2130006. DOI: 10.1142/S0218271821300068. arXiv: 2109.05481 [gr-qc].

[221] R. M. Wald. *General Relativity*. Chicago, USA: Chicago Univ. Pr., 1984. DOI: 10.7208/chicago/9780226870373.001.0001.

[222] D. H. Weinberg, J. S. Bullock, F. Governato, R. Kuzio de Naray, and A. H. G. Peter. "Cold dark matter: controversies on small scales". In: *Proc. Nat. Acad. Sci.* 112 (2015), pp. 12249–12255. DOI: 10.1073/pnas.1308716112. arXiv: 1306.0913 [astro-ph.CO].

[223] J. A. Wheeler. "Geons". In: *Phys. Rev.* 97 (2 Jan. 1955), pp. 511–536. DOI: 10.1103/PhysRev.97.511. URL: https://link.aps.org/doi/10.1103/PhysRev.97.511.

[224] M. I. Wilkinson and N. W. Evans. "The present and future mass of the Milky Way halo". In: *Mon. Not. Roy. Astron. Soc.* 310 (1999), p. 645. DOI: 10.1046/j.1365-8711.1999.02964.x. arXiv: astro-ph/9906197.

[225] X.-J. Yue and Z. Cao. "Gravitational waves with dark matter minispikes: Fourier-domain waveforms of eccentric intermediate-mass-ratio-inspirals". In: *Class. Quant. Grav.* 41.9 (2024), p. 095011. DOI: 10.1088/1361-6382/ad38fb.

[226] H.-S. Zhao and J. Silk. "Mini-dark halos with intermediate mass black holes". In: *Phys. Rev. Lett.* 95 (2005), p. 011301. DOI: 10.1103/PhysRevLett.95.011301. arXiv: astro-ph/0501625.

[227] L. Zwick, P. R. Capelo, and L. Mayer. "Priorities in gravitational waveforms for future space-borne detectors: vacuum accuracy or environment?" In: *Mon. Not. Roy. Astron. Soc.* 521.3 (2023), pp. 4645–4651. DOI: 10.1093/mnras/stad707. arXiv: 2209.04060 [gr-qc].

[228] F. Zwicky. "Die Rotverschiebung von extragalaktischen Nebeln". In: *Helv. Phys. Acta* 6 (1933), pp. 110–127. DOI: 10.1007/s10714-008-0707-4.

Statement on the use of Generative AI

I did use the generative AI assistance tools Le Chat and ChatGPT. Generative AI was used for short-form input assistance as summarizing tool to extract key concepts from specific published papers. These bullet points summaries were used to structure parts of the introduction and the conclusion of this work.
The text, code, and images in this thesis are my own (unless otherwise specified). Generative AI has only been used in accordance with the KU Leuven guidelines and appropriate references have been added. I have reviewed and edited the content as needed and I take full responsibility for the content of the thesis.

Publication List

The work presented in this thesis is based on the following publications and preprint articles.

Journal article

[66] P. A. Cano, L. Machet, and C. Myin. "Boson Stars with Nonlinear Sigma Models". In: *Phys. Rev. D* 109.4 (2024), p. 044043. DOI: 10.1103/PhysRevD.109.044043.

[78] S. Chakraborty, G. Compère, and L. Machet. "Tidal Love numbers and quasinormal modes of the Schwarzschild-Hernquist black hole". In: *Phys. Rev. D* 112.2 (2025), p. 024015. DOI: 10.1103/4p2c-rwdh. arXiv: 2412.14831 [gr-qc].

[164] L. Machet and L. Aresté Saló. "Scalar fields from nonlinear sigma models on black hole spacetimes". In: *Phys. Rev. D* 112.8 (2025), p. 084047. DOI: 10.1103/klxz-fgmt. arXiv: 2508.18362 [gr-qc].

FACULTÉ DE SCIENCES
PHYSIQUE THÉORIQUE ET MATHÉMATIQUE
Campus Plaine – Building NO – CP 231
Boulevard du Triomphe
B-1050 Bruxelles
https://ptm.ulb.be

FACULTY OF SCIENCE
DEPARTMENT OF PHYSICS AND ASTRONOMY
Celestijnenlaan 200D box 2415
B-3001 Leuven
ludovico.machet@kuleuven.be
https://fys.kuleuven.be/itf